IMPURITIES IN ANTIFERROMAGNETIC TRANSITION-METAL OXIDES – SYMMETRY AND OPTICAL TRANSITIONS

by

John Emil Petersen III, M.S.

A dissertation submitted to the Graduate Council of
Texas State University in partial fulfillment
of the requirements for the degree of
Doctor of Philosophy
with a major in
Materials Science, Engineering, and Commercialization
December 2017

Committee members:

Thomas Myers, Chair

Luisa Scolfaro, Co-Chair

Wilhelmus Geerts

Ravi Droopad

Benjamin Martin

Cecilia Temponi

FAIR USE AND AUTHOR'S PERMISSION STATEMENT

Fair Use

Duplication Permission

ACKNOWLEDGMENTS

First and foremost, I would like to thank Dr. Luisa Scolfaro who was my chief advisor throughout my time in graduate school. Her patience and guidance was and is greatly appreciated. Much of what I have achieved has been a direct result of her professional support and knowledge. I would like to thank her for allowing me to approach problems in my own way, which has shaped me into the scientist I have become.

She introduced me to multiple extraordinary individuals whose expertise proved invaluable in my research. I was lucky enough to be able to visit the Solid State Theory Department at Friedrich-Schiller-Universität Jena, Germany, where I had the pleasure of meeting and starting a collaboration with Dr. Friedhelm Bechstedt and Dr. Jürgen Furthmüller. Friedhelm's vast knowledge of electronic excitations in solids was extremely helpful and inspired me to learn more about symmetry, which became a large focus in this work. Jürgen's extensive technical expertise was at times critical to solving problems I have encountered, throughout the time I have spent working with Luisa. Dr. Silvana Botti and the rest of wonderful people in their department made me feel at home during the short few weeks of my visit.

During my time in graduate school at Texas State University, I worked with a number of excellent experimentalists. I would like to give a special thanks to the chair of my committee, Dr. Thomas Myers, who taught me quite a lot about experimental material

characterization. He was very helpful with a particular potential business endeavor, as well. He has been quick to offer assistance and wisdom, whenever I needed anything, and I hope to repay that kindness in time. Dr. Craig Swartz was extremely helpful during my short time as an experimentalist, showing me “the ropes,” so to speak. Also, he inspired me to improve my knowledge of the C language, and I was glad to help convert his PLI modeling program to run on our high-performance computing cluster.

From the engineering and chemistry departments, I would like to thank Dr. Ravi Droopad and Dr. Benjamin Martin, respectively. I spent a semester with each of them in independent study, and their knowledge helped to shape this dissertation into what it is today. Ravi piqued my interest in complex oxides, and Benjamin taught me essential chemistry, of which I was not aware, since my background is in physics.

Finally, I would like to cordially thank Dr. Wilhelmus Geerts. With his funding and professional support, I was able to return to my passion – theoretical work. While much of the work presented here (NiO, with and without impurities and defects) is specifically related to the DOD grant (HBCU/MI grant W911NF-15-1-0394), I was extremely pleased that he allowed me to explore similar transition-metal oxides, as well. As it turned out, the broader the study became, the understanding of all materials involved became greater. Without his leadership, this would not have been possible.

Certainly, acknowledgments would not be complete without thanking my family. Their encouragement and patience during trying times has been invaluable.

TABLE OF CONTENTS

Page

LIST OF TABLES

Table **Page**

LIST OF FIGURES

Figure **Page**

ABSTRACT

The study of antiferromagnetic transition-metal oxides is an extremely active area in the physical sciences, where condensed matter physics, inorganic chemistry, and materials science blend together. The sheer number of potential commercial applications is staggering, but much of the fundamental science remains unexplained. This is not due to a lack of effort, however, as theorists have been struggling to understand these materials for decades – particularly the character of the band edges and first optical transitions. The difficulty lies in the strong correlation or Coloumb attraction between the electrons in the anisotropic d orbitals, which conventional band theory cannot describe adequately. The correlation problem is approached here by the well-accepted method of adding a Hubbard potential energy term to the ground state Hamiltonian, calculated within Density Functional Theory. The frequency-dependent complex dielectric function is calculated within the Independent Particle Approximation, and optical transitions are evaluated in multiple different ways.

Peaks in the imaginary part of the dielectric function are compared energetically to orbitally decomposed density of states calculations. Optical transitions are typically analyzed in terms of atomic orbitals, which, strictly speaking, gives misleading results. Here, however, from the calculated data, two alternative interpretations are analyzed for each material studied. The first employs rigorous group theoretical analysis to determine allowed electric-dipole transitions, taking into account both orbital hybridization and

crystal symmetry. The second interpretation is that of metal cation site hopping. In this interpretation, carriers hop from the $x^2 - y^2$ d orbital of one metal cation lattice site to the next metal cation site which is antiferromagnetically aligned. At times, thoughout this work, one interpretation is favorable to the other.

Which interpretation is most valid depends on the material considered. For example, simple rock-salt transition-metal oxides are quite different from the high temperature superconducting cuprates. A range of materials is studied here, in order to gain a greater understanding of optical transitions in highly-correlated systems. In this work, O vacancies are introduced in NiO, along with Fe impurities, to understand better the band filling in the insulating behavior observed experimentally. These results are compared with those of La_2NiO_4, La_2CuO_4, $La_{2-x}Sr_xNiO_4$, and $La_{2-x}Sr_xCuO_4$. to elucidate the mechanisms behind the symmetry breaking phenomena in the Sr doped systems.

As it turns out, indeed, the $x^2 - y^2$ orbital in these materials plays a critical role in spatial charge distribution, magnetic, and spin densities which are coupled to the dopant position in the lattice. The in-depth study of electronic and optical properties of transition-metal oxides presented here provides theoretical characterization of the infamous pseudogap in the cuprates – one of the greatest mysteries of modern solid state physics. In addition, via Density Functional Perturbation Theory, the phonon coupling with charge-density wave is explored in $La_{2-x}Sr_xNiO_4$ and found to be the dominant contributing factor to the colossal dielectric constant.

1. INTRODUCTION

The present work is a theoretical dissertation on structural, electronic, magnetic, and optical properties in transition metal oxides, within Density Functional Theory (DFT). Deficiencies in DFT in the study of these materials are alleviated by employing a Hubbard potential energy U (DFT + U), which accounts for electron-electron interaction of d orbitals in these highly-correlated systems. The effects of dopants and other symmetry-breaking phenomena are investigated and analyzed by group theoretical methods, bringing new insight and understanding to this distinct class of materials. Before detailing the theoretical background, a short review on electronic applications of the materials studied is warranted, in order to convey the motivation behind this work.

The electronics revolution of modern times began with a single commercially viable transistor in 1959 and has since evolved to the point where microprocessors can contain over a billion transistors, while flash memory chips have tens of billions, in accordance with the famous Moore's Law.[1,2] As demand to store more data at less cost increases, conventional flash memory devices approach fundamental physical limits.[3–5] The traditional method of increasing memory density in random-access memory (RAM) devices, based on complimentary metal-oxide-semiconductor (CMOS) technology, is by scaling down in size, thus increasing the number of transistors per unit area. As oxide thickness approaches tens of nanometers (nm), quantum mechanical tunneling occurs, causing leakage current through the gate of CMOS transistors.[6] Therefore, new nonvolatile memory technology, with non-charge based memory storage, for use in

RAM, is necessary for the future of integrated electronics.[7]

Emerging RAM technologies include magnetic RAM (MRAM), ferroelectric RAM (FeRAM), spin-transfer torque RAM (STT-RAM), phase-change RAM (PRAM), and resistive RAM (RRAM or ReRAM), among others. RRAM is especially promising due to the ease of integration in CMOS technology, durability, low energy consumption, nonvolatility, and fast switching speed in the tens of nanoseconds (ns).[4,5] While materials of interest for the insulating active layer in RRAM vary from metal oxides, organic materials, and chalcogenides,[8] NiO is particularly attractive, due to its simplicity, high endurance, and excellent retention.[9–11] This dissertation will focus heavily on theoretically characterizing optical and electronic properties of NiO and the physical effects of O vacancies and Fe dopants on such properties.

The methods used to study NiO can be extended to more complex transition metal oxides, such as La_2NiO_4 and La_2CuO_4. The intrinsic materials are not of much interest for electronic applications; however, upon hole doping, interesting physical properties emerge, such as a colossal dielectric constant (CDC) in the nickelate and high-temperature superconductivity (HTSC) in the cuprate. A unitless value, the dielectric constant describes the extent to which an electric field can propagate through a material when multiplied by the permittivity of free space. CDC materials are sought for supercapacitors which can store a much larger amount of energy in the form of charge than conventional capacitors. As integrated circuits (ICs) become smaller, the passive components, such as capacitors, must become smaller and require enhanced performance. Furthermore, supercapacitors, based on CDC materials, could replace rechargeable

batteries in the near future, due to their potentially superior lifetimes and energy densities. Sr-doped La_2NiO_4, $La_{2-x}Sr_xNiO_4$ (LSNO), where Sr substitutionally replaces La in the lattice, is particularly promising, since it maintains a CDC at high frequency, which is desirable for modern electronic devices.

Not only is LSNO promising for engineering applications, but the complex mechanisms responsible for its CDC, including charge and spin-ordered phenomena, make LSNO an important material for studying emerging solid state physics. The scientific community has uncovered a host of ordered phenomena in related materials since the discovery of HTSC in a doped antiferromagnetic (AF) cuprate in 1986,[12] for which the authors Bednorz and Müller won the Nobel Prize in Physics in 1987. $La_{2-x}Sr_xCuO_4$ (LSCO) is a material exhibiting HTSC which is isostructural to LSNO. HTSC is an active area of research, both experimentally and theoretically, since the relationships between order, disorder, and coupling of complex mechanisms, as well as the influence of competing orders due to charge, spin, orbital, and lattice fluctuations are heavily debated.[13] The relationship between the notorious pseudogap (PG) and HTSC is uncertain, as well. The origin of the PG is one of the most prominent unsolved problems in condensed matter physics. In addition to the PG, the superconducting gap (SC gap) is present in HTSC materials, as well as in type I and type II superconductors. The relationship between the SC gap and superconductivity in type I and type II superconductors is well described by Bardeen–Cooper–Schrieffer (BCS) theory, for which they received the Nobel Prize in Physics in 1972. However, the mechanism(s) behind HTSC in the cuprates is thought to be different from that of the traditional (type I

and type II) superconductors. Here, physical properties of insulating LSNO are compared to those of superconducting LSCO to explore these mechanisms and help illuminate the mysteries surrounding them.

Before addressing the new physics, some background on physical mechanisms in the materials studied is included for a full comprehension of the impact of the work presented here. The following sections review the relevant literature surrounding the current understanding of RRAM as it relates to NiO (1.1) and of stripe physics as it relates to applications of LSNO and LSCO (1.2). Chapter 2 reviews theoretical background extensively, and results are presented in Chapter 3, along with discussion and comparison with previous work, when possible. In many cases, the subject matter of Chapter 3 consists of theoretical predictions, which are presented here, for the first time. The most notable findings here include a description of the mechanism behind the CDC in LSNO and the origin of the pseudogap (PG) (discussed below) in LSCO.

1.1 Resistive Random Access Memory

Metal-insulator-metal (MIM) interfaces which exhibit resistive switching from a high resistance state (HRS) to a low resistance state (LRS), under an applied bias, form the basis for RRAM technology. Applying a threshold voltage – at which the insulator, typically a transition metal oxide, exhibits dielectric breakdown – results in a switching from HRS to LRS called the “set” process. The “reset” process, which is the switching from a LRS to a HRS, can be unipolar or bipolar. A MIM system that can be reset by applying the same voltage polarity as the set process is unipolar, and if opposite voltage

polarities result in equivalent behavior, the unipolar system is said to be nonpolar. If bipolar, the set process is achieved through applying an opposite voltage polarity as that of the reset process.[4,5] Although oxides exhibiting both a HRS and LRS have been observed since the 1960s,[4,5,14–16] the physical mechanism behind the switching process has been understood only recently and will be covered in the following sub-section (Section 1.1.1).

1.1.1. Physical Mechanism

The dielectric breakdown process, where a MIM interface switches from a HRS to a LRS under an applied bias, is the result of conductive filaments (CFs) forming through the oxide (Figure 1),[17] from one electrode to the other, and can be observed in both unipolar and bipolar switching cases.[4,5,18] Upon removing an electrode, CF formation has been experimentally confirmed on the surface of the oxides NiO, TiO_2, HfO_2, and $SrTiO_3$, among others, by atomic force microscopy (AFM).[5,9–13] CFs are initially formed in what is aptly called the “forming” process, where dielectric soft breakdown results from an applied voltage across the MIM interface, sufficient to produce an electric field > 10 MV/cm, which stresses the oxide, creating grain boundaries.[4,22] Further, the electric field causes the O ions to diffuse through the grain boundaries toward the anode, leaving behind O vacancies and/or metal precipitates, which make up the stoichiometry of the CFs.[5,23–27] Two less common models describing a conducting path through the oxide include that of electron or hole trap states[28,29] or that of a Mott transition from carriers doped at the interface.[30] The set process (HRS to LRS) is essentially the same as the

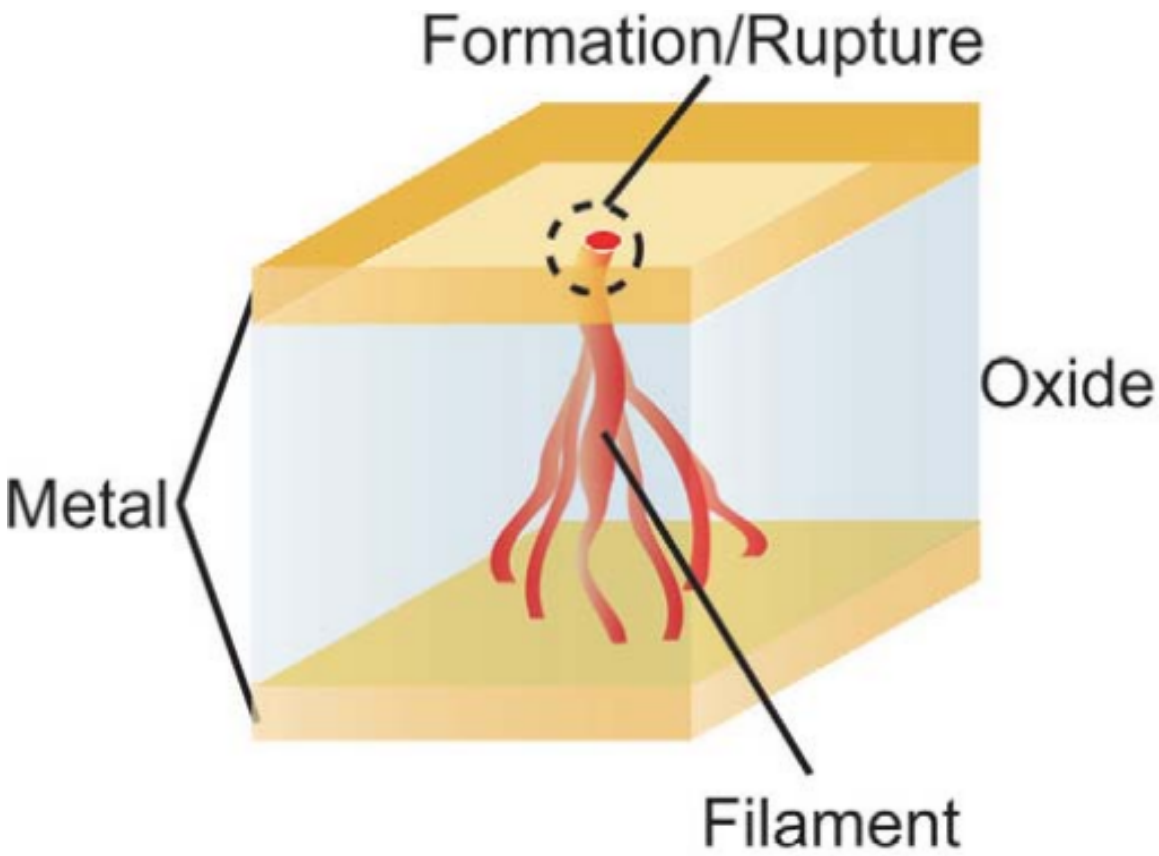

Figure 1. Schematic Model of RRAM Mechanism. *Filaments indicate paths of least electronic resistance, where O vacancies are most prevalent. The schematic is taken from Reference [17].*

forming process; however, less voltage is required, and the MIM device must be set and reset numerous times in order to stabilize the CFs, before reliable operation can be achieved.[4,5,10]

While the bulk of recent literature agrees that the physics of the forming and set processes (HRS to LRS) can be universally attributed to diffusion of O vacancies, resulting in CFs, the reset process (LRS to HRS) is generally thought to be different for unipolar and bipolar cases. Bipolar switching in RRAM is perhaps the simplest, since the reset process is just the opposite of the set process: the applied bias in the opposite direction diffuses the O ions back into the grain boundaries, thus bonding again with the

cations, disrupting the CFs. In the unipolar case, however, a reset voltage less than that of the set voltage, but with the same polarity, thermally oxidizes the excess metal ions in the CFs, i.e., Ni in NiO.[4,5,18] In essence, the voltage is high enough to generate heat, diffusion, and oxidation of the metal cations, yet low enough not to exert a substantial force to push O anions away from the attractive positively charged vacancies. The physical differences in unipolar and bipolar switching are such that bipolar switching MIM RRAM devices have greater stability.[31] NiO can exhibit both unipolar and bipolar switching.[9,32]

1.1.2 NiO

In recent years, NiO_y has been studied for numerous applications ranging from use as the pseudocapacitor electrode in electrochemical supercapacitors,[33,34] the spin filter in spintronics applications,[35] the electrochromic (EC) material in EC devices,[36] the sensing material in gas sensor devices,[37] and perhaps most noteworthy, the resistive switching material in RRAM.[8–10,32,38–42] The y in NiO_y represents a non-stoichiometric concentration of O, with a value less than unity indicating O vacancies or Ni precipitates, and with a value greater than unity indicating Ni vacancies or excess O interstitials. Being the functional material in all of the mentioned applications, clearly, the physical properties of NiO_y are of great interest for the next generation of electronic devices.

To assist in characterization of such devices, this work will investigate the frequency-dependent dielectric function in relation to the partial density of states (PDOS) and band structure, for both intrinsic NiO and the case with O vacancies (Sections 3.1.1 and 3.1.2, respectively). The stoichiometry of the CFs, consisting of O vacancies, results

in different electronic properties from the bulk, which can be characterized via optical measurements. Recently, by the Independent Particle Approximation (IPA)[43] (Section 2.3.2), the author of this work has shown for the first time that an additional optical transition occurs at lower energy when O vacancies are introduced to the system, resulting from a reduced direct band gap caused by an impurity energy level.[44] With transparent electrodes, this transition could be detected during the switching process. The static dielectric constant is calculated as well, within Density Functional Perturbation Theory (DFPT), and compared to the IPA results, as well as experiment.[45]

In addition to electronic and optical characterization, regardless of the type of switching, understanding the diffusion of oxygen is paramount to developing improved RRAM devices. Improvements are necessary, before commercial viability of NiO RRAM is possible. Device operation can be improved by reducing the reset current and reducing fluctuation in resistance during the switching process.[18,39,46] Therefore, in addition to studying the electronic structure and optical properties, energy barrier and tangential force of diffusion of the O anions is calculated here by the Nudged Elastic Band method.[47] The calculations of the present work will serve to assist in understanding fundamental physics of NiO and developing future RRAM devices.

1.1.3 $Ni_{1-x}Fe_xO$

While NiO has been studied extensively, little work has been done with antiferromagnetic $Ni_{1-x}Fe_xO$ (Fe:NiO), also known as permalloy oxide (PyO). A ferromagnetic alloy of Ni and Fe (permalloy) is used in magnetic recording heads. Ni_{1-}

$_xFe_xO$ has been considered undesirable in industry, since oxidation changes the magnetic order, due to spinel precipitates.[48] However, some recent experimental works have focused on ferromagnetic (FM) $Ni_{1-x}Fe_xO$ for applications in spintronics devices. These studies use solution-based preparation of nanoparticles, in oxygen-rich conditions, resulting in formation of Fe_2O_3 and $NiFe_2O_4$ crystallites for Fe concentrations in FM $Ni_{1-x}Fe_xO$, for x ranging from 0.02 to 0.05.[49–53] The high surface to volume ratio of the nanoparticles results in the interesting FM properties.[54] With sputter deposition – a type of physical vapor deposition – oxygen levels can be finely tuned to achieve near-stoichiometric or oxygen-poor AF $Ni_{1-x}Fe_xO_y$ thin films. The phase diagram of the Ni-Fe-O system reports a stable rock salt structure for iron concentrations up to x = 0.4 in a low oxygen atmosphere.[55] Reports of dual ion beam sputtered $Ni_{1-x}Fe_xO$ (x = 0.19) and radio frequency magnetron sputtered $Ni_{1-x}Fe_xO$ confirm the rock salt crystal structure for films sputtered at low oxygen pressure.[48,56,57] At lower concentrations, Yan, et al. have found a NaCl rock-salt phase for pulsed laser deposition grown $Ni_{1-x}Fe_xO$ (x = 0.02), as well.[58]

In this work, the antiferromagnetic rock-salt phase of $Ni_{1-x}Fe_xO$ is investigated theoretically for the first time by ab initio methods. The previously mentioned NiO calculations are compared to those of the Fe-doped system, with x = 0.125 and 0.25 in Section 3.3, and varying O vacancy concentrations are included in the analysis in Section 3.4. Fe-doping effects on electronic structure, optical properties, dielectric properties, and diffusion of O anions will be evaluated, with a particular emphasis on how addition of Fe affects RRAM switching capability.

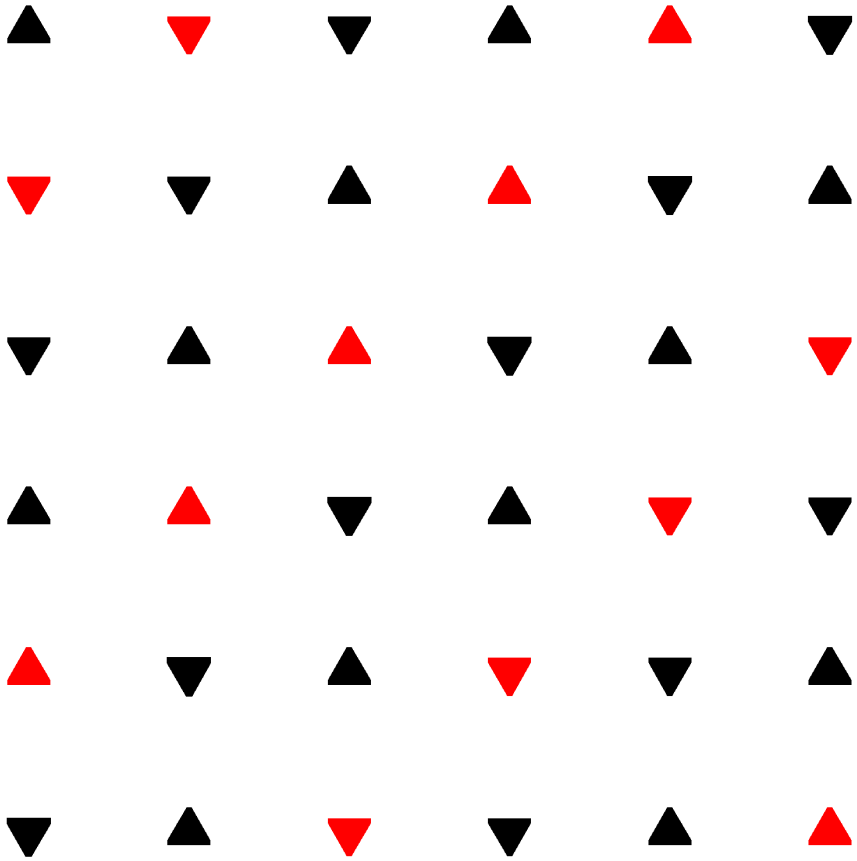

Figure 2. Schematic of stripes in the Ni-O plane of $La_{2-x}Sr_xNiO_4$ (LSNO). *Shown is the commensurate x = 1/3 case. Triangles indicate spin direction on Ni atoms, while red triangles indicate magnetically frustrated Ni sites where charge-density waves are densest.*

1.2 Stripe Physics in Transition-Metal Oxides

The ordering mentioned previously in LSNO and LSCO includes, but certainly is not limited to, charge-density waves (CDWs) and spin-density waves (SDWs). A CDW is self-organized charge density, generally from hole-doping or oxygen interstitials, arranged in periodic patterns at the atomic scale, below a charge-ordering temperature T_{CO}. Magnetization is frustrated at sites where the excess charge density is greatest. These frustrated sites act as domain walls to AF order, and a SDW manifests as the resulting periodic magnetic order, of lattice period twice that of the CDW, occurring below a spin-

ordering temperature T_{SO}, where generally $T_{SO} < T_{CO}$. A combination of CDW and SDW aligns in "stripes" in the two-dimensional Cu-O or Ni-O bonding planes, which are separated by Mott insulating layers (Mott insulators are discussed in detail in Section 3.1). A schematic of commensurate stripes in the plane of x = 1/3 $La_{2-x}Sr_xNiO_4$ (LSNO) is shown in Figure 2. Stripe physics is an active area of research, both experimentally and theoretically, since the relation between stripes and the formation, coupling, and filling to HTSC, as well as the influence of competing orders due to charge, spin, orbital, and lattice fluctuations are heavily debated.[13]

Hücker et al. found convincing experimental evidence that the enhanced commensurability of stripes at x = 1/8, in $La_{2-x}Ba_xCuO_4$, resulted in suppression of HTSC.[59] They showed that the same composition can exhibit slight SC behavior in the Cu-O planes.[60,61] For Sr concentration slightly less than 1/8, replacing Ba by Sr, in electrochemically oxygen-doped $La_{2-x}Sr_xCuO_{4+\delta}$, excess oxygen congregates as interstitials, such that hole concentration in the bulk equals 1/8.[62] Due to the yet-unexplained physics associated with this highly commensurate concentration, it has come to be known as the 1/8 anomaly.[63] Nearly isostructural yet insulating $La_{2-x}Sr_xNiO_4$ (LSNO) is well known to exhibit stripes and have a colossal dielectric constant (CDC) into the GHz range, with its highest values reported being ~10^6–10^7 for a Sr concentration of x = 1/8, where the colossal value is interpreted as resulting from spatial modulation of hole charge.[64,65] However, x-ray diffraction and inelastic neutron scattering measurements on LSNO have shown that neither the charge ordering transition nor the magnetic ordering transition is well defined.[66,67]

In addition to being of interest for oxide electronics, comparing stripe physics of LSNO with $La_{2-x}Sr_xCuO_4$ (LSCO) can help illuminate the mechanism(s) behind HTSC in the cuprates, by analyzing the different carrier filling. Recently, Coslovich, et al. detected a mid-infrared optical gap in LSNO, with x = ¼.[68] They interpreted it as having PG characteristics, which they attributed to electronic localization (disorder), rather than stripes (order). In the cuprates, two d orbital gaps of Cu $x^2 - y^2$ (i.e., d orbital) character are present – the PG and the SC gap. The SC gap is the lower energy gap where Cooper pair formation is thought to occur in the Cu-O plane below a critical temperature T_C, while the PG is at higher energy and is present below a temperature T*, where $T^* > T_C$. Both gaps exhibit a Fermi surface along the nodal bonding direction in the Cu-O plane and have Cu $x^2–y^2$ and O p character. The origin of the PG in the cuprates is heavily debated[63,69] and is one of the most prominent unsolved problems in condensed matter physics, along with the mechanism(s) behind HTSC, and whether a connection between the two is significant.

In this work, charge and spin ordering, electronic structure, and dielectric response are theoretically characterized for highly commensurate x=1/3 LSNO and x=1/4 LSCO from first principles. Experimentally, below x = 1/2, the nickelate remains insulating,[70,71] while the cuprate is past the SC limit at x = 0.3 and is semi-metallic[72]. The concentration of x = 1/3 has been found to show the most commensurate stripe ordering for x < 1/2 in LSNO.[71,73] At these critical Sr doping concentrations, well-defined fillings of the stripe atoms in the Ni-O and Cu-O planes may occur. The two nearly isostructural layered materials crystallize in the tetragonal crystal system with I4/mmm space group

without doping. They are model materials to study the interplay of charge, spin, and lattice degrees of freedom. In particular, the d-electron shells of the transition metal atoms Ni and Cu, which differ by only one electron, allow investigations of the influence of band filling. Electronic structure of the resulting stripe phases are analyzed by band structure and projected density of states (PDOS). The frequency-dependent dielectric tensor allows conclusions about interband transitions and the static dielectric constants of LSNO. The phonon contribution to the static dielectric constants is calculated via Density Functional Perturbation Theory, where it is found that significant phonon-CDW coupling accounts for the huge values of the CDC. The dielectric functions of LSCO are not calculated, because of its semi-metallic band structure, which would require the inclusion of Drude-like terms to account for intraband transitions; however, the electronic structure is compared to the results of LSNO. The dopant concentrations studied in the nickelate and the cuprate are chosen to be highly commensurate with the lattice, resulting in a net magnetic moment of zero for the unit cell, simulating bulk samples.

1.2.1 Colossal Dielectric Constant in $La_{2-x}Sr_xNiO_4$ (LSNO)

New materials which exhibit extremely high dielectric constants are sought for use in reducing the size of passive components in emerging electronic devices. As transistors, microprocessors, and memory chips get smaller, the passive components in integrated circuits (ICs), which are resistors, inductors, and capacitors, encompass a growing fraction of real estate in electronic devices. Current technology allows capacitors to be fabricated as thin films, reducing the footprint;[74] however, often, the capacitors must

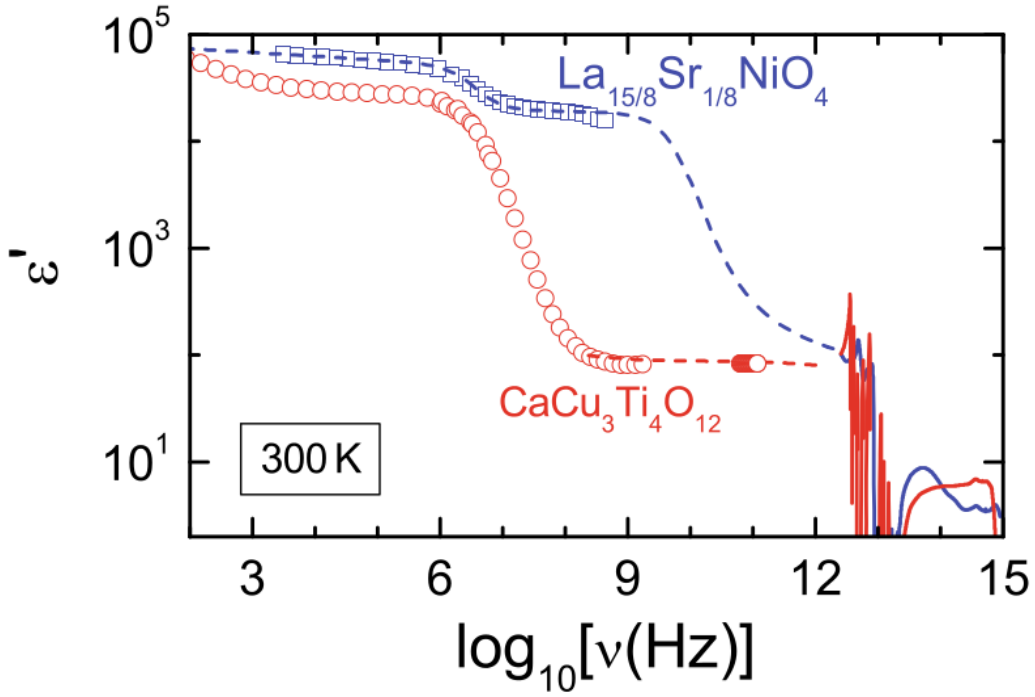

Figure 3. Frequency-Dependent Dielectric Function of LSNO vs CCTO. The real component of the dielectric function is shown over a broad frequency range for LSNO and CCTO. Figure taken from Reference [64].

be external to the IC, because the capacitance required for device operation is higher than can be achieved in the silicon chip.[75] Electrolytic capacitors typically have a higher capacitance per unit volume ratio than thin film capacitors, but they are prone to failure.[76] Therefore, new materials, with a CDC, are sought for use in thin film capacitors with much greater capability. A CDC material is one with a unitless dielectric constant k greater than 10^3.[77] LSNO is one of the best performing CDC materials. A key consideration in choosing a material for such an application is its dielectric loss, which corresponds to how much energy is lost in operation, through heat. Dielectric loss can be found from the following relation

$$L_{\alpha\alpha}(\omega) = -Imag\left(\frac{1}{\epsilon_{\alpha\alpha}(\omega)}\right),$$

where α corresponds to the direction of applied field and response, ω is the angular frequency, and ε is the complex permittivity

$$\epsilon = \epsilon_1 + i\,\epsilon_2 .$$

$\varepsilon_{\alpha\alpha}$ corresponds to the dielectric response in the α direction from a field applied in the α direction.

$CaCu_3Ti_4O_{12}$ (CCTO) is the current material of choice for non-electrolytic capacitor thin films for CDC applications. The problem with CCTO is that it loses its CDC at higher frequency, beginning around 1 megahertz (MHz or 10^6 Hz). At 1 gigahertz (GHz or 10^9 Hz), the dielectric constant is reduced to only about 100, at room temperature.[77] LSNO, on the other hand, maintains its CDC at about 400 MHz and is predicted to go into the GHz range, at room temperature (Figure 3). This is an important observation, since modern applications require operation into the GHz range.[78]

1.2.2 High-Temperature Superconductivity (HTSC) in $La_{2-x}Sr_xCuO_4$ (LSCO)

The complex orders observed in LSNO are also present in isostructural LSCO; however, in the case of the cuprate, the relation between ordered phases and HTSC is unclear. Superconductivity can be described as a state of zero electronic resistance which expels magnetic fields up to an inherent critical field. While type I and some type II superconductors can be explained by BCS theory, the origins of HTSC in cuprates remain an unsolved problem in physics. In BCS theory, type I superconductors at extremely low temperature are described as having Cooper pairs that are coupled electrons which attract rather than repel due to fluctuations in the lattice from phonons. Each electron attracts

local atomic nuclei in the lattice causing an attractive force on the other electron. This pairing causes the electrons to behave as bosons rather than fermions, allowing them to condense into the same energy level, since bosons are not restricted by the Pauli exclusion principle of fermions. Metals which have strong vibronic interactions exhibit superconductivity below a critical temperature slightly above absolute zero.

While type I superconductors are pure metals, type II superconductors are alloys which exhibit superconductivity at slightly higher temperatures than type I cases and have higher critical fields, allowing for higher current densities. The critical field is the minimum magnetic field strength which can penetrate the material, which extinguishes superconductivity, yielding nonzero resistance, where current density is dependent upon the curl of the magnetic field, by Maxwell's equations. Still, even type II superconducting materials have to be cooled by liquid helium, limiting practical applications. In 1986, Bednorz and Müller discovered the first case of HTSC behavior in the doped ceramic $La_{2-x}Ba_xCuO_4$, with a critical temperature of 30 K.[12] They won the Nobel prize in physics in 1987 for their discovery. Soon after, several similar cuprates were found to have a critical temperature above 77 K, which can be cooled by liquid Nitrogen, a much less expensive coolant than helium, making superconducting applications a practical reality. Such potential applications include maglev trains, low loss electrical grids, magnetic resonance imaging (MRI), supercomputers with new architecture and logic, and particle accelerators, some of which are closer to commercial viability than others.

While applications are being developed, theorists struggle to explain fundamental aspects of HTSC materials. However, much progress has been achieved in the past 30

years, and is mentioned above (Section 1.2). The cuprates exhibiting HTSC are doped Mott insulators (Mottness is discussed in Section 3.1). A wide variety of AF cuprate insulators exhibit HTSC upon hole doping, whether that doping be with Sr, Ba, or excess O interstitials. While all the HTSC cuprates are inherently complex and exhibit multiple symmetry breaking phases, including CDWs and SDWs, LSCO is perhaps the simplest. Being isostructural to LSNO and of similar composition, direct comparisons between the CDC insulating nickelate and the HTSC cuprate are calculated here within an almost parameter-free ab initio approach for the first time. By this comparison, the origin of the pseudogap in the cuprates is predicted to be directly related to the CDW.

1.3 Overview

Before discussing calculation results, some theoretical background is necessary, and Chapter 2 will provide a comprehensive overview. The bulk of the present work is in Chapter 3, where calculation results are presented, discussed, analyzed, and compared to the relevant literature when available. Each intrinsic material and each doped or vacancy-containing material has its own section in Chapter 3, where optical transitions are analyzed in relation to electronic structure and symmetry arguments. A large part of Chapter 3 is dedicated to the study of intrinsic NiO (Section 3.1), which is a particularly appropriate and deceptively simple introduction to physical properties of AF transition-metal oxides, and the chapter will become progressively more complex. Effects of varying concentrations of Fe dopants on physical properties of NiO, without O vacancies (Section 3.2.1) and with O vacancies (Section 3.2.2), are presented for the first time.

Energy barriers of O diffusion in NiO will be compared with cases of heavily Co- or Fe-doped NiO in Section 3.2.2. A short section on intrinsic La_2NiO_4 (Section 3.3.1) will be followed by analysis of calculations on LSNO, where the physical mechanism behind the colossal dielectric constant will be revealed for the first time in Section 3.3.2. In preparation for the final section, Section 3.4.1 will discuss physical properties of intrinsic La_2CuO_4. Finally, the answer to one of the greatest mysteries in modern solid state physics will be addressed in Section 3.4.2 – the origin of the pseudogap in the HTSC cuprates. Conclusions and future work will be discussed in Chapter 4.

2. THEORETICAL BACKGROUND

It is the intent of the author to follow a pedagogical approach such that all of the information contained herein will be accessible to persons of the appropriate mathematical background. For this reason, the key points of the theories employed in the present work will be covered in this chapter. Density Functional Theory (DFT) is treated here with brevity (Section 2.1), since the author has written an extensive account in his master's thesis,[79] beginning with the many-body problem, and including topics such as exchange-correlation approximations and the projector-augmented wave methodology. Extensions to DFT, including the effective Hubbard potential U – J (Section 2.2), a short discussion on density of states (2.3), the Independent Particle Approximation (IPA) (Section 2.4), and Density Functional Perturbation Theory (DFPT) (Section 2.5) are covered here. Group theory as it pertains to optical transitions and crystal field splitting are fundamental to understanding analysis throughout Chapter 3, and the relevant background is in Section 2.6. Section 2.7 is a short account of the theory of the Nudged Elastic Band (NEB) method.

2.1 Density Functional Theory (DFT)

Energy is perhaps the most useful physical property in science, and theorists working in materials science, solid state physics, and chemistry use DFT as the tool of choice for calculating it. Due to the impact DFT has made on the scientific community, Walter Kohn and John Pople shared the Nobel Prize in Chemistry in 1998 – Kohn for the

underlying theory, and Pople for computational advances in the theory. The Hohenberg-Kohn theorems state that the fundamental electron density function n(**r**) – with which ground-state energy E is solely determined, via a functional form of the many-body Schrödinger equation – has just one density, which is dependent upon position **r**. The ground-state energy dependent upon this exact n(**r**) is lower than the total ground-state energy calculated from any other n_R(**r**). The potential energy between nuclei and electrons is described by just one value for $\hat{\boldsymbol{V}}_{ne}$, as well.

The total potential energy V in the time-independent Schrödinger equation,

$$\hat{H}\psi=(-\frac{\hbar^2}{2m}\nabla^2+V)\psi=E\psi, \qquad (2.1.1)$$

can be broken down into constituent parts, making it more tractable in the many-body quantum mechanical case. The caret over the Hamiltonian H indicates that it is an operator which acts on the wavefunction ψ. The kinetic energy term encompasses the ħ, which is Planck's constant, the nabla operator, which is the three-dimensional vector derivative with respect to position, and the mass m. The reason to decompose V is because electron-electron Coulombic interaction is particularly difficult to determine, except in the simplest cases, due to the wavelike nature of the electron. Thus, the new equation becomes (in Dirac notation)

$$\langle\boldsymbol{\psi}|\hat{\boldsymbol{H}}|\boldsymbol{\psi}\rangle=\langle\boldsymbol{\psi}|(\hat{\boldsymbol{T}}+\hat{\boldsymbol{V}}_{ne}+\hat{\boldsymbol{U}}_{ee})|\boldsymbol{\psi}\rangle+U_{nn}=\mathrm{E}, \qquad (2.1.2)$$

where $\hat{\boldsymbol{T}}$ is the kinetic energy operator, $\hat{\boldsymbol{V}}_{ne}$ is the potential energy between nuclei and electrons, $\hat{\boldsymbol{U}}_{ee}$ is the potential energy between electrons, and U_{nn} is the potential energy between nuclei, which is not an operator in the Born-Oppenheimer approximation,

where nuclei are approximated to have no kinetic energy. U_{nn} is frequently omitted when discussing total energy.

Now that the potential energy is decomposed into multiple components, the electron-electron potential energy can be split further to account for correlation and exchange. Correlation corresponds to a potential energy term that takes into account the probability that an electron at position **r** has a low chance of being close to another electron at **r'** – with n(**r**) and n(**r'**) being in a dual space within the same volume – and a high chance of being farther away, due to the Coulomb repulsion. Here, this probability will be represented as g(**r**, **r'**). Due to the wavelike nature of electrons, g(**r**, **r'**) for correlation is not simple to calculate and is only known for homogeneous systems. Exchange, on the other hand, can be calculated very precisely. Exchange arises from the Pauli Exclusion Principle, which states that electrons of the same spin cannot occupy the same position (orbital); however, an electron of opposite spin can. Therefore, U_{ee} can be described as

$$U_{ee}=\frac{1}{2}\int\int\frac{n(\boldsymbol{r})n(\boldsymbol{r}')}{|\boldsymbol{r}-\boldsymbol{r}'|}d^3\boldsymbol{r}\,d^3\boldsymbol{r}'+\frac{1}{2}\int\int\frac{n(\boldsymbol{r})n(\boldsymbol{r}')}{|\boldsymbol{r}-\boldsymbol{r}'|}[g(\boldsymbol{r},\boldsymbol{r}')-1]d^3\boldsymbol{r}\,d^3\boldsymbol{r}'. \quad (2.1.3)$$

The first term on the right-hand side is known as the Hartree potential, which is classical and electrostatic, and the second term on the right-hand side is the combined exchange and correlation correction energy, ε_{XC}, from quantum mechanics, which includes the probability g(**r**, **r'**). The Hartree potential is the largest contribution to U_{ee} and known exactly, followed by the exchange, which can be calculated precisely also, and the smallest contribution is the correlation, which must be approximated.

Ignoring spin density, the full Kohn-Sham ground-state energy equation becomes

$$E=-\sum_{i=1}^{N_\varphi}\langle\varphi_i|\nabla^2|\varphi_i\rangle-\sum_{j=1}^{P}\int\frac{Z_j n_R(\boldsymbol{r})}{|\boldsymbol{R}_j-\boldsymbol{r}|}d^3\boldsymbol{r}+\frac{1}{2}\sum_{j\neq k}\frac{Z_j Z_k}{|\boldsymbol{R}_j-\boldsymbol{R}_k|}$$
$$+\frac{1}{2}\int\int\frac{n_R(\boldsymbol{r})n_R(\boldsymbol{r}')}{|\boldsymbol{r}-\boldsymbol{r}'|}d^3\boldsymbol{r}\,d^3\boldsymbol{r}'+\int n_R(\boldsymbol{r})\epsilon_{XC}[n_R(\boldsymbol{r})]d^3\boldsymbol{r}. \quad (2.1.4)$$

Hartree notation is used here for convenience. Z corresponds to the number of protons in each nucleus, **φ** is the wavefunction of each individual electron, **R** refers to position of nuclei, and the density $n_R(\mathbf{r})$ is a reference electron density,

$$n_R(\boldsymbol{r})=2\sum_{i=1}^{N_\varphi}|\varphi_i(\boldsymbol{r})|^2, \quad (2.1.5)$$

which is iteratively improved, along with the total energy and ε_{XC}, until the ground state reaches the desired accuracy. The iterative equations are as follows – first

$$\hat{\boldsymbol{V}}_{ne}+\int\hat{\boldsymbol{U}}_{ee}\,n_R(\boldsymbol{r}')\,d^3\boldsymbol{r}' \quad (2.1.6)$$

is calculated by the initial approximation of $n_R(\mathbf{r})$. Next, the exchange and correlation contribution to the chemical potential is calculated by

$$\mu_{XC}[n(\boldsymbol{r})]=\frac{\delta E_{XC}}{\delta n_R(\boldsymbol{r})}. \quad (2.1.7)$$

Kohn and Sham's idea was to find a system of non-interacting electrons which had the same electronic density as that of the interacting system and treat it as homogeneous. Once the non-interacting density is exactly the same as the interacting one, the chemical potential μ will be the same in both cases; otherwise, charge would flow from one to the other, if they were adjacent. This is called the Local Density or Local Spin-Density Approximation (LDA or LSDA). LSDA will be used in this work, along with a more sophisticated technique called the Generalized Gradient Approximation (GGA), which treats valence electron distribution closer to the core as more dense than that further

away. Hybrid functionals combine DFT with Hartree Fock theory to determine ε_{XC}. The exchange-correlation functionals used in this work include the LSDA of Ceperly and Alder,[80] the so-called PBE functional in the GGA, named for Perdew, Burke, and Ernzerhof,[81] and the hybrid functional HSE06 of Heyd, Scuseria, and Ernzerhof, where the term hybrid corresponds to a mixing of Hartree-Fock Theory with DFT.[82] For more information on treatment of ε_{XC}, along with a summary of the projector-augmented wave (PAW) method,[83] see the author's master's thesis.[79]

Finally, eigenvalues ε_i and eigenvector wave functions $\boldsymbol{\varphi}_i$ can be found from the set of one-orbital Schrödinger equations:

$$\{-\frac{1}{2}\nabla^2+\hat{\boldsymbol{V}}_{ne}+\int \hat{\boldsymbol{U}}_{ee}\, n_R(\boldsymbol{r}')\, d^3\boldsymbol{r}'+\mu_{XC}[n_R(\boldsymbol{r})]\}\boldsymbol{\varphi}_i[n_R(\boldsymbol{r})]=\epsilon_i\,\boldsymbol{\varphi}_i[n_R(\boldsymbol{r})]. \quad (2.1.8)$$

A new charge density, $n_{Rout}(\mathbf{r})$, that is no longer homogeneous and changes with $\mathbf{r}$, can be calculated by:

$$n_{R_{out}}(\boldsymbol{r})=2\sum_{i=1}^{N_\varphi}|\boldsymbol{\varphi}_i|^2. \quad (2.1.9)$$

The process can be repeated iteratively, achieving a more and more accurate electron density (accurate up to ∇^4), until the desired accuracy for E and the eigenvalues ε_i is obtained. The computational software Vienna Ab Initio Simulation Package (VASP),[84,85] which is used for all ground-state energy and eigenvalue calculations in this work, is based on these fundamental self-consistent equations of Kohn-Sham theory.

For completeness, it should be noted that an infinite crystal has potential energy which is periodic with the lattice and can be represented by a unit cell. The solutions to the Schrödinger equation in a periodic potential have the form

$$\psi_{\boldsymbol{k}}(\boldsymbol{r}) = u_{\boldsymbol{k}}(\boldsymbol{r}) \exp(i\,\boldsymbol{k}\cdot\boldsymbol{r}),$$

which is called the Bloch theorem, where $u_{\mathbf{k}}(\mathbf{r})$ has the period of the lattice, and **k** is a reciprocal lattice vector. Unit cells for each material will be described in each respective section in Chapter 3. The symmetries associated with each cell have an effect on various physical properties. How these properties relate to symmetry and group theory will be discussed in Section 2.6.

2.2 Effective Hubbard U – J Potential Energy in the Dudarev Approximation

For many materials which contain ions with partially-filled d or f shells, conventional DFT (LSDA) either incorrectly predicts metallic behavior or greatly underestimates the energy band gap. In other cases, HTSC materials are found to not have magnetic properties described correctly. Materials with partially filled d or f orbitals are said to be highly-correlated, meaning correlation, as described in the previous section, is particularly strong between electrons in d or f orbitals which are partially filled. The Coulomb energy required to place two d electrons at the same site can be described by the Hubbard parameter

$$U = E(d^{n+1}) + E(d^{n-1}) - E(d^{n}), \qquad (2.2.1)$$

where n is the number of d electrons in the neutral ground-state of energy E. In LSDA, interactions such as the Hubbard potential energy are assumed to be small compared to the valence bandwidth, but this is not the case for Mott-like insulators. Here, a Mott-like insulator is one which has substantial d states near the band gap. In LSDA, spin in $n_R(\mathbf{r})$ is dependent upon Hund's-rule exchange energy (J), but in Mott-like insulators, spin is

predominantly dependent upon the Hubbard potential energy. The problem is that the Hubbard potential energy (U) is roughly an order of magnitude greater than the exchange energy.[86]

Since all materials studied in this work have Mott-like valence bandwidths and band gaps involving 3d states, an effective Hubbard U – J Hamiltonian, following the Dudarev approach,[87] is added to the Hamiltonian in Equation 2.1.4 in all calculations in this work. The addition is as follows:

$$\hat{H}=\frac{U}{2}\sum_{m,m',\sigma}\hat{n}_{m,\sigma}\hat{n}_{m',-\sigma}+\frac{(U-J)}{2}\sum_{m\neq m',\sigma}\hat{n}_{m,\sigma}\hat{n}_{m',\sigma} \quad , \tag{2.2.2}$$

where orbital degeneracy of the 3d shell is taken into account. The $\hat{n}_{\sigma}=\hat{a}_{\sigma}^{\dagger}\hat{a}_{\sigma}$, is an operator for the number of electrons located at a site, and m and σ are the magnetic and spin quantum numbers, respectively. At the end of the iterative process, the total ground-state energy becomes

$$E_{LSDA+U}=E_{LSDA}+\frac{(U-J)}{2}\sum_{l,j,\sigma}\rho_{lj}^{\sigma}\rho_{jl}^{\sigma}, \tag{2.2.3}$$

where ρ_{jl}^{σ} is the density matrix of d electrons. The ½ in Equations 2.2.2 and 2.2.3 are to prevent double-counting. For more details on the Dudarev approach to the Hubbard potential energy as implemented in DFT, see Reference [87].

In VASP, both U and J are introduced to the program as user-supplied constants. Commonly, these values are determined empirically by varying over a range and choosing appropriate values based on agreement of physical properties with experimental quantities. It has been shown recently that certain values of U – J can result in greater agreement with some experimental physical properties, while other values result in

greater agreement with other physical properties.[88] Thus, care must be taken when choosing appropriate values. Chapter 3 discusses in detail the values used for the U – J values in the different systems studied here.

2.3 Density of States

Frequently in Chapter 3, density of states will be used to characterize the band structure and optical transitions, so a short definition is in order. Converting the eigenvalues in Equation 2.1.8 to be functions of **k**, the density of states can be found independently for each spin by

$$g_n(\epsilon)=\int \frac{d\boldsymbol{k}}{4\pi^3}\delta(\epsilon-\epsilon_n(\boldsymbol{k})), \tag{2.3.1}$$

where the integral is over the primitive cell.[89]

2.4 The Independent Particle Approximation (IPA)

The IPA is a powerful theoretical tool for the calculation of the frequency-dependent complex dielectric function in the long-wavelength limit. The Brillouin zone (BZ) is reduced to an irreducible wedge of the crystal symmetry group (symmetry discussed in Section 2.6), where the following limit is evaluated:

$$\varepsilon^{(2)}_{\alpha\beta}(\omega)=\frac{4\pi^2e^2}{\Omega}\lim_{q\to 0}\frac{1}{q^2}\sum_{c,v,\boldsymbol{k}} 2w_{\boldsymbol{k}}\delta(\epsilon_{c\boldsymbol{k}}-\epsilon_{v\boldsymbol{k}}-\omega)\times\langle u_{c\boldsymbol{k}+e_\alpha q}|u_{v\boldsymbol{k}}\rangle\langle u_{c\boldsymbol{k}+e_\beta q}|u_{v\boldsymbol{k}}\rangle^*. \tag{2.4.1}$$

The imaginary part (indicated by the 2) of the dielectric tensor is indicated by ε, where α and β indicate the tensor components, as functions of ω. The electron charge and primitive cell volume are represented by e and Ω, respectively. The limit is evaluated as

the wave vector **q** approaches zero (wavelength approaches infinity). The indices c, v, and **k** stand for conduction bands, valence bands, and reciprocal lattice vectors, respectively. The weights of **k**, $w_{\mathbf{k}}$, sum to unity. The ϵ indicates eigenvalues of valence or conduction bands, depending on index. The e_α and e_β are representative of Cartesian unit vectors. The u characters indicate Bloch quantum mechanical wave vectors, where orthogonality will yield zero, which indicates an optical transition at that energy/frequency is forbidden. The * represents a complex conjugate, and the δ is the Dirac delta function.

Transitions are allowed at non-zero values, in accordance with quantum mechanics. Since the limit is evaluated numerically, with wavefunctions calculated from density functional theory, information about the character of the transition is not given from the equation directly. Therefore, some analysis of density of states (Section 2.3), along with group theory analysis and quantum mechanical selection rules (Section 2.6) can help to interpret results. From the imaginary part, the real part of the frequency-dependent dielectric tensor can be calculated by the Kramers-Kronig transformation:

$$\varepsilon_{\alpha\beta}^{(1)}(\omega)=1+\frac{2}{\pi}P\int_0^\infty \frac{\varepsilon_{\alpha\beta}^{(2)}(\omega')\omega'}{\omega'^2-\omega^2}d\omega', \tag{2.4.2}$$

where the 1 indicates the real portion, and P indicates the Cauchy principle value, which accounts for the singularity at ω' = ω.[89]

It should be noted that the excitonic contribution to the dielectric function is not included in this approximation, which is based on PAWs. A similar approach which is much more expensive, yet approaches more accurate conduction band eigenvalues and includes quasiparticle effects, is the IPQA, where the Q designates quasiparticle. However, for a full excitonic study which also includes local field effects (LFE), the

extremely expensive method of solving the Bethe-Salpeter equation is recommended. The IPA calculations in this work do not include excitonic effects but do include LFEs in DFT. LFEs are microscopic electric fields present from local dipoles in the periodic cell which, in this case, are included by exchange and correlation contributions to the wavefunctions. For more information on the IPA and how it relates to PAWs, see Reference [43].

2.5 Density Functional Perturbation Theory (DFPT)

In DFPT, the electronic and vibrational degrees of freedom are separated within the Born-Oppenheimer adiabatic approximation. The electronic Hamiltonian can be solved as in Section 2.1, and the linear response of a lattice distortion perturbation can be described by differentiating the Hellmann-Feynman forces with respect to atomic core coordinates by

$$\frac{\partial^2 E(\boldsymbol{R})}{\partial \boldsymbol{R}_i \partial \boldsymbol{R}_j} = \frac{\partial \boldsymbol{F}_i}{\partial \boldsymbol{R}_j} = \int \frac{\partial n(\boldsymbol{r})}{\partial \boldsymbol{R}_j} \frac{\partial V_{ne}(\boldsymbol{r})}{\partial \boldsymbol{R}_i} d\boldsymbol{r} + \int n(\boldsymbol{r}) \frac{\partial^2 V_{ne}(\boldsymbol{r})}{\partial \boldsymbol{R}_i \partial \boldsymbol{R}_j} d\boldsymbol{r} + \frac{\partial^2 E_N(\boldsymbol{R})}{\partial \boldsymbol{R}_i \partial \boldsymbol{R}_j}, \tag{2.5.1}$$

where notation is consistent with Section 2.1.

Currently, within the PAW methodology implemented in VASP, only static values of the dielectric tensor can be calculated via the polarization induced by perturbations in Equation 2.5.1. The DFPT method is based entirely upon the ground-state which does not depend on conduction bands. The equation for the vibronic component of the static dielectric tensor in DFPT is

$$\varepsilon_\infty(\hat{\boldsymbol{q}}) = 1 - \frac{8\pi e^2}{\Omega} \sum_{v,\boldsymbol{k}} 2 w_{\boldsymbol{k}} \langle \hat{\boldsymbol{q}} \boldsymbol{\beta}_{v\boldsymbol{k}} | \varphi_{v\boldsymbol{k}} \rangle, \tag{2.5.2}$$

where $\hat{\boldsymbol{q}}$ represents the three Cartesian unit vectors, and $\boldsymbol{\beta}$ and φ are the polarization vector and perturbed wave function, respectively, for valence band v, where φ is determined from Equation 2.1.8. Again, w_k represents the weights of each k point, which sum to unity. Finally, the total static dielectric constant $\varepsilon_{ij}^{\infty}(0)$ can be given by the sum of Equations 2.4.2 and 2.5.2. Here, the zero indicates zero frequency. For more information on the dielectric constant within DFPT, see References [90] and [43].

2.6 Symmetry, Crystal Field, and Selection Rules

Much of the analysis in Chapter 3 is derived from group theory arguments, which is discussed briefly in this section. Several different symmetries are explored in this work, which are dependent upon the crystal symmetry of the respective material studied. Vacancies, dopants, magnetic order, CDW, and SDW are explored in Chapter 3, and all of them break crystal symmetry to a certain extent. When symmetry is broken, degeneracy of partially filled d orbitals is lifted, leading to crystal field splitting. Since NiO, La_2NiO_4, La_2CuO_4, and all the variants studied here have d states present near the Fermi energy, this splitting is particularly important when evaluating optical transitions, and each optical transition in this work is scrutinized by the quantum mechanical selection rules of crystals within group theory.

First, it should be noted that the crystal field in 3d transition-metal oxides is much stronger than the spin-orbit interaction (SOI),[91] so SOI is neglected throughout this study, and spin is treated as collinear. By collinear, it is meant that the charge density of Section 2.1 for each spin channel is treated as non-interacting. In the binary cubic rock-salt

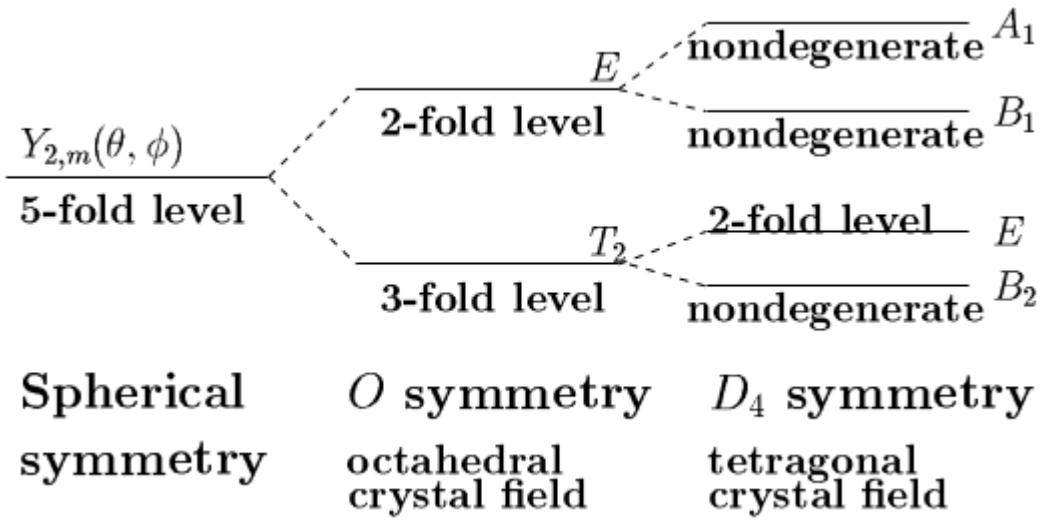

Figure 4. Crystal Field Splitting of d Orbitals in Octahedral and Dihedral Coordination. *Figure adapted from Reference* [91].

structure, the crystal field is octahedrally coordinated, with O_h symmetry, leading to the d level splitting into doublet e_g and triplet t_{2g} states. The g indicates even parity, which originates from the German word for even – gerade (the subscript u denotes ungerade or odd). The e_g states have basis functions $(\sqrt{3})(x^2 - y^2)$ and $3z^2 - r^2$, and the t_{2g} states have basis functions xy, yz, and zx, where basis functions and their orthogonality are explained in Appendix B. If symmetry is reduced from a cubic crystal to a tetragonal one of symmetry D_{4h}, the e_g level splits further into A_{1g} and B_{1g} nondegenerate states with basis functions z^2 and $x^2 - y^2$,, and the t_{2g} level splits into a doublet E_g level (xz, yz) and a nondegenerate B_{2g} level (xy), as indicated in the schematic in Figure 4 for the symmetry D_4. Note that the first letter of the orbital symmetry can be upper or lower-case, and both notations are used here, interchangeably. The h in O_h and D_{4h} represents a horizontal reflection symmetry, so a g is added to the states of O and D_4 in Figure 4.

While group theory only determines whether the splitting occurs and cannot

determine the energies, the density of states from Section 2.3 gives quantitative energetic information about these levels called the projected or partial density of states (PDOS). The selection rules of quantum mechanics and group theory combined with PDOS and the frequency-dependent complex dielectric function from the IPA (Section 2.4) can predict which optical transitions are possible.

The traditional quantum mechanical selection rules for an atomic electric-dipole transition include angular momentum quantum number $\Delta l = \pm 1$; magnetic quantum number $\Delta m_l = -1, 0,$ or 1; spin quantum number $\Delta m_s = 0$; and, initial (φ) and final (ψ) states must be of opposite parity.[91] Going a step further, the relation governing the selection rule of an electric-dipole transition in group theory is as follows:

$$\psi^{i'}_{\alpha'} \otimes \hat{\boldsymbol{H}}^{j}_{\beta} \otimes \varphi^{i}_{\alpha}, \tag{2.6.1}$$

where $\otimes$ represents a direct matrix product, i and i' are irreducible representations of symmetry operations, α and α' are partners of irreducible representations Γ_i and $\Gamma_{i'}$, and the electric-dipole Hamiltonian is

$$\hat{\boldsymbol{H}}^{j}_{\beta} = -\frac{e}{2mc}\,\hat{\boldsymbol{p}}\cdot\boldsymbol{A}. \tag{2.6.2}$$

The $\hat{\boldsymbol{p}}$ term is the electron momentum operator, and **A** is the vector potential of an external electromagnetic field. Magnetic-dipole and electric-quadrupole transitions are known to be weak and will not be addressed in the present work. Equation 2.6.1 can determine whether an electric-dipole transition is allowed or forbidden. An allowed transition has nonzero matrix element(s) upon evaluating Equation 2.6.1, and a forbidden optical transition will not.

However, it has been pointed out by Rödl and Bechstedt that a purely atomic

electric-dipole interpretation of optical transitions in transition-metal oxides can be highly deceptive.[92] Here, optical transitions of hybrid orbitals are considered, as well. In any case, for any transition, precisely to which symmetries a given symmetry is allowed to transition can be determined by

$$a_{\lambda\mu\nu}=\frac{1}{h}\sum_{C_\alpha} N_{C_\alpha}[\mathrm{X}^{(\lambda)}(C_\alpha)\mathrm{X}^{(\mu)}(C_\alpha)][\mathrm{X}^{(\nu)}(C_\alpha)]^*, \tag{2.6.3}$$

where h is the order of the group (number of group elements), $N_{C\alpha}$ is the number of elements in the class C_α, and $X^{(i)}(C_\alpha)$ are irreducible representations of a group, where the product is a linear combination of the irreducible representations:

$$\mathrm{X}^{(\lambda)}(R)\mathrm{X}^{(\mu)}(R)=\sum_{\nu} a_{\lambda\mu\nu}\mathrm{X}^{(\nu)}(R). \tag{2.6.4}$$

Equation 2.6.3 will be used frequently in the analysis in Chapter 3. Incidentally, symmetry of hybrid orbitals can be predicted in this way, as well, in what is known as ligand field theory. Further, since high-symmetry points in the Brillouin zone have their own symmetry operations, the equation can be applied to optical transitions in specific regions of **k** space, where the Bloch states mentioned in Section 2.1 are described accordingly. For more information on group theory, see References [91], [93], and [94].

2.7 The Nudged Elastic Band (NEB) Method

As an ion diffuses through a bulk crystal, it will encounter an energy barrier between stable sites, corresponding to a local maximum. The minimum energy along this path is aptly referred to as the minimum energy path (MEP). Since a continuous calculation within DFT would be prohibitively expensive, in the NEB method within VASP, the user chooses a set number of steps, or data points to calculate, named images.

Each image corresponds to an ion's position along the path, and the total ground-state energy is calculated for the entire system, as outlined in Section 2.1, for each image of the ion along the path, resulting in an MEP curve.

The force at each image i along the MEP is given by

$$\boldsymbol{F}_i = \boldsymbol{F}_i^s - \boldsymbol{F}_i^t, \tag{2.7.1}$$

where the spring force $\mathbf{F}^s = k\mathbf{x}$ is given for each image by

$$\boldsymbol{F}_i^s = k\left(\left|\boldsymbol{R}_{i+1} - \boldsymbol{R}_i\right| - \left|\boldsymbol{R}_i - \boldsymbol{R}_{i-1}\right|\right)\cdot\hat{\boldsymbol{\tau}}_i, \tag{2.7.2}$$

and the true force is given for each image by

$$\boldsymbol{F}_i^t = \nabla E\left(\boldsymbol{R}_i\right) - \nabla E\left(\boldsymbol{R}_i\right)\cdot\hat{\boldsymbol{\tau}}_i. \tag{2.7.3}$$

The constant k is the spring constant, and $\hat{\boldsymbol{\tau}}_i$ is the normalized local tangent at image i. More information can be found in references [95] and [47].

3. CALCULATION RESULTS AND DISCUSSION

Structural, magnetic, spin, electronic, optical, and dielectric properties are calculated within DFT for NiO (Section 3.1), Fe:NiO (Section 3.2), La_2NiO_4 (Section 3.3), $La_{2-x}Sr_xNiO_4$ (Section 3.4), La_2CuO_4 (Section 3.5), and $La_{2-x}Sr_xCuO_4$ (Section 3.6). Results are presented, and analysis is carried out in each respective section, comparing with previous works, both experimental and theoretical, when possible. All calculations were performed on the STAR cluster, at Texas State University. For a discussion of new key findings, see Chapter 4.

3.1 NiO

Nickel (II) Oxide (NiO) is an antiferromagnetic (AF) insulator with structural space group Fm3m (isostructural to rock salt or NaCl). The NiO (NaCl) unit cell can be described as two interlaced face-centered cubic cells which are separated by half of the lattice constant. The result of this description is a cubic cell (octahedral or O_h symmetry) with alternating anions and cations and can be seen in Figure 5(a). The structural primitive cell has two atoms; however, due to antiferromagnetism at room temperature, with a Néel temperature T_N of ~525 K, the magnetic primitive cell must contain at least four atoms, in order to contain both spin up and spin down Ni. The four atoms are highlighted in green in Figure 5(a), and the magnetic primitive cell is shown in Figure 5(b). The lattice vectors for the magnetic primitive cell in Figure 5(b) are

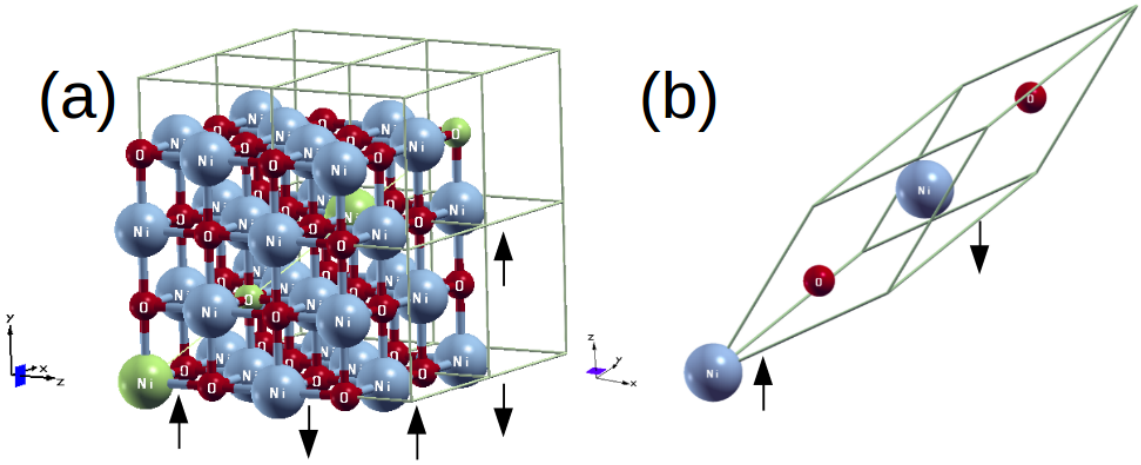

Figure 5. Primitive Cell of NiO. *Ni are gray, and O are red. Arrows indicate local magnetization of Ni (111) planes. The (a) cubic representation, with lattice vectors 2**a** can be reduced to a (b) trigonal magnetic primitive cell by sampling only the four green atoms.*

$$\boldsymbol{a}_1 = a\,\hat{\boldsymbol{x}} + \frac{a}{2}\,\hat{\boldsymbol{y}} + \frac{a}{2}\,\hat{\boldsymbol{z}},$$
$$\boldsymbol{a}_2 = \frac{a}{2}\,\hat{\boldsymbol{x}} + a\,\hat{\boldsymbol{y}} + \frac{a}{2}\,\hat{\boldsymbol{z}}, \qquad (3.1.1)$$
$$\boldsymbol{a}_3 = \frac{a}{2}\,\hat{\boldsymbol{x}} + \frac{a}{2}\,\hat{\boldsymbol{y}} + a\,\hat{\boldsymbol{z}},$$

where $\hat{\boldsymbol{x}}$, $\hat{\boldsymbol{y}}$, and $\hat{\boldsymbol{z}}$ are the Cartesian unit vectors. The cubic representation can be reduced by 1/8 of Figure 5(a), by sampling one of the eight cubes outlined in gray. The trigonal (a type of rhombohedral cell) primitive cell in Figure 5(b) has half the volume and half the number of atoms of one eighth of Figure 5(a), making the calculation with the unit cell in Figure 5(b) more computationally efficient. Magnetization vectors (indicated by arrows in Figure 5) are parallel in the (111) plane (type II AF ordering), with Ni in each adjacent plane in the [111] direction having antiparallel magnetization. Bonding is mostly ionic, with charge of Ni 2^+ and O 2^-.

Ni $4s^2 3d^8$ and O $3s^2 3p^4$ electrons were treated as valence in the PBE-generated PAWs, whereas inner orbitals were taken to be frozen in the core. Cutoff energy was chosen to be 320 eV, where plane waves with kinetic energy larger than the cutoff energy

are excluded from the calculation. A 4 × 4 × 4 gamma-centered k-point mesh was used to calculate the ground state in 32 atom 2 × 2 × 2 cells. The 32 atom cell was used in even the intrinsic case in order to compare directly with cases with vacancies and/or Fe dopants.

3.1.1 Intrinsic NiO

The lattice parameter, a, was optimized by varying the value sufficiently, fitting to the Birch-Murnaghan Equation of State[96]

$$P(V)=\frac{3B_0}{2}[(\frac{V_0}{V})^{\frac{7}{3}}-(\frac{V_0}{V})^{\frac{5}{3}}][1+\frac{3}{4}(B_0^{'}-4)[(\frac{V_0}{V})^{\frac{2}{3}}-1]], \quad (3.1.2)$$

where P is pressure, V is volume, and V_0 and B_0 are the volume and bulk modulus at zero pressure, respectively, where

$$B_0=-V\frac{\partial P}{\partial V}, \quad (3.1.3)$$

evaluated at P equal to zero. The interpolated minimum energy corresponds to the optimized volume, with the structural lattice parameter for this particular unit cell being

$$a_0=\frac{1}{2}(16V_0)^{1/3}, \quad (3.1.4)$$

which is 7.915 Bohr radii or 4.189 Å. The 16 originates from the fact that Figure 5(a) has 16 times the volume and number of atoms as Figure 5(b), whereas the 2 indicates that each lattice vector in Figure 5(a) is twice the length of the lattice constant. Two cubic unit cells in each direction illustrate this. The excellent Birch-Murnaghan fit can be seen in Figure 6.

Electronic structure and other physical properties of intrinsic NiO were calculated

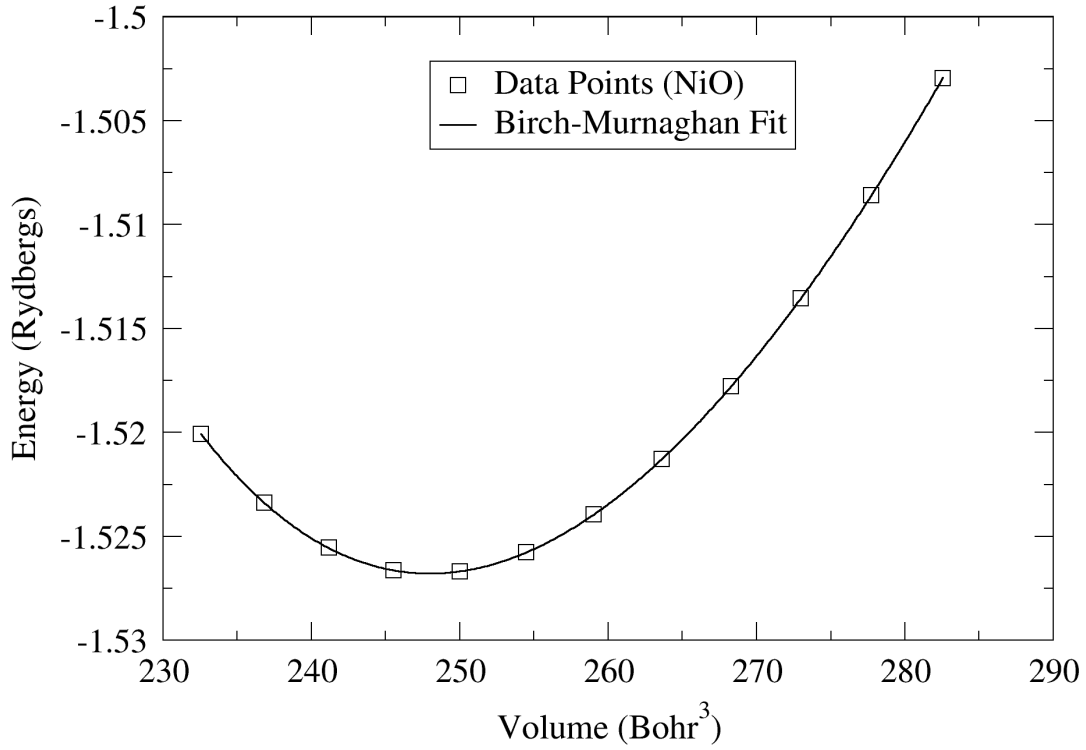

Figure 6. Birch-Murnaghan Fit of Intrinsic NiO. *Calculated energies for each volume considered are indicated by squares. The Murnaghan fit was performed using equation 3.1.2, where V_0 is at the minimum of the curve, and 1 Rydberg = 13.6 eV.*

here and compared to previous works to illustrate the accuracy of the methods used. Table 1 shows a comparison of the physical properties of NiO calculated here with those of experiment and theory, and a high level of agreement can be seen. As expected, an increase in the band gap was observed when using the HSE06 functional. The magnitude of the magnetic dipole moment of each Ni is indicated by μ (Bohr magnetons), where Ni in adjacent (111) planes have opposite sign. The value listed for the band gap of NiO is that of the indirect gap. The static optical dielectric constant, ε(∞), of Table 1 was calculated within the long wavelength limit of the Independent Particle approximation[43] (IPA) (Section 2.4), and the total static dielectric constant, ε(0), was

Table 1. Physical properties of intrinsic NiO. *Comparisons with previous works are shown, both theoretical and experimental, where a is lattice constant, B is bulk modulus, μ is magnetic dipole moment of Ni, E_g is the indirect band gap energy, and ε is the dielectric constant. Theoretical results from this work and others were calculated with VASP-PAW, within GGA+U, with an effective U = 5.3 eV. These values are compared to our HSE06 calculations, as well.*

	a (Å)	B (GPa)	μ (Bohr)	E_g (eV)	ε(∞)	ε(0)
Theory						
PRB 77, 134103 (2008) (GGA + U)	4.19	189	1.67	3.53		
PRB 69, 075413 (2004) (GGA + U)	4.2	202.5	1.72	3.2		
Hyung Dong Lee Dissertation(2011) (GGA + U)	4.21	188.55	1.67	3.26		
This Work (GGA+U)	**4.19**	**183**	**1.71**	**3.29**	**5.81**	**13.4**
PRB 79, 235114 (2009) (HSE03)	4.17		1.6	4.1	4.5	
This Work (HSE06)	**4.19**		**1.68**	**4.65**		
Experiment						
PRB 27, 6964 (1983)	4.17		1.9			
JAP 104, 113521 (2008)		188, 189, 195				
JAP 36, 2446 (1965)					5.7	
J. Phys. C 8, 3955 (1975)					5.7	13.0
PNAS 105, 2783 (2008)				3.4 – 4.3		
Optica Applicata, XLI, 2, 431 (2011)				3.4 – 3.58		

calculated by summing the optical contribution (IPA) with the vibronic contribution from Density Functional Perturbation Theory[90] (DFPT) (Section 2.5). HSE06 values of the band gap are listed for comparison and can be seen to overestimate conduction band eigenvalues substantially. For this reason, and since the GGA + U calculations show excellent agreement with previous work, both experimental and theoretical, DFT + U (Sections 2.1 – 2.2) is used throughout the rest of this study. An effective U – J value of 5.3 eV was used in all NiO calculations, because previous theoretical works have found this value to give excellent quantitative agreement with experimental physical properties.[41,97]

To analyze physical properties related to electronic structure and optical transitions, first, the band structure is calculated along high-symmetry lines in the BZ. The reciprocal lattice vectors, high-symmetry points, and path through the BZ can be seen in Figure 7. The high-symmetry points, in reciprocal lattice units of 2π/a, are

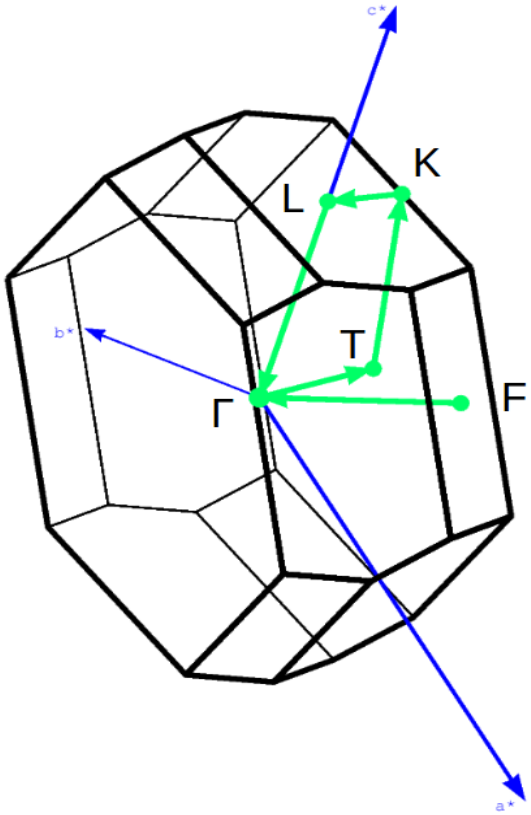

Figure 7. Primitive Brillouin Zone of Antiferromagnetic NiO. *Primitive vectors are shown in blue, and the path of the band structures in Figures 7 and 8 is shown in green.*

F = (0.5, 0.0, 0.5);

Γ = (0.0, 0.0, 0.0);

T = (0.5, 0.5, 0.5);

K = (0.375, 0.375, 0.75);

L = (0.0, 0.0, 0.5).

This path gives a representative sampling of the relevant BZ by symmetry, and the resulting band structure calculation, within GGA + U, can be seen in Figure 8. For comparison, the band structure calculated within HSE06 is shown in Figure 9. In both cases, an indirect band gap can be seen, with the valence band maximum (VBM) at T and

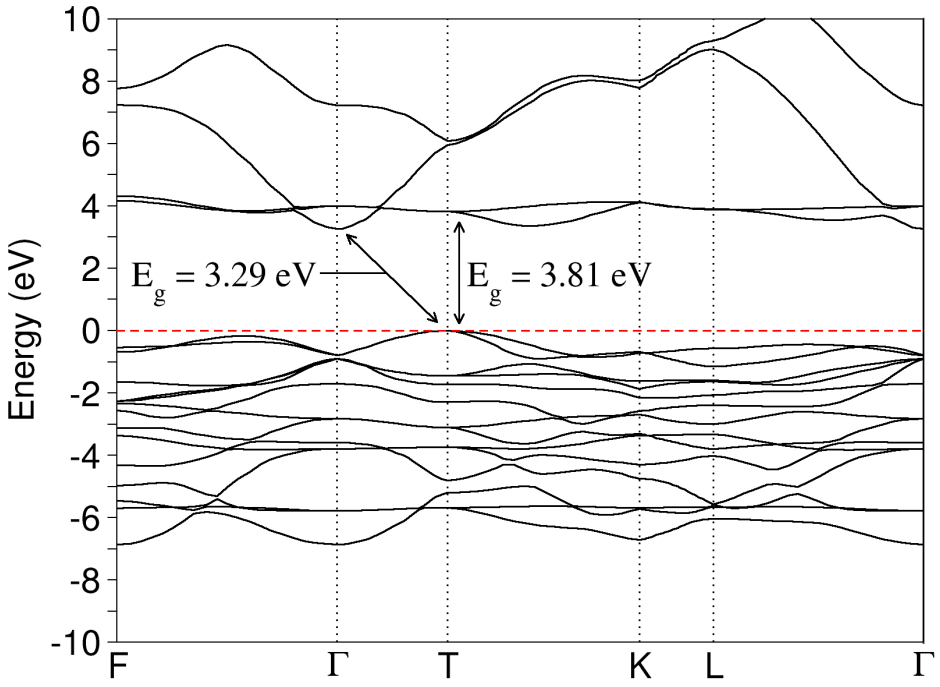

Figure 8. Calculated GGA + U Band Structure of Intrinsic NiO. *An indirect band gap of 3.29 eV can be seen between the Γ and T points. The smallest direct band gap is 3.81 eV, at the T point. The red dashed line indicates the Fermi Energy, taken to be zero.*

the conduction band minimum (CBM) at Γ, whereas the minimum direct band gap is at the T point. All of the eigenvalues in both figures are adjusted to the Fermi energy, which is taken to be zero, and is shown as a red dashed line.

The optical band gap of approximately 4.0 eV has undergone considerable scrutiny over the years, and while originally thought to be a Mott insulator, the current consensus is that NiO is either a charge-transfer insulator or possibly having characteristics of both types.[40,98–104] The gap of a Mott insulator consists of a d-d transition, as a result of exchange and crystal field splitting, whereas the gap of a charge-transfer insulator consists of a transition typically from the anion valence band to the cation conduction band.[99] Most works report a valence band comprised of a mix between

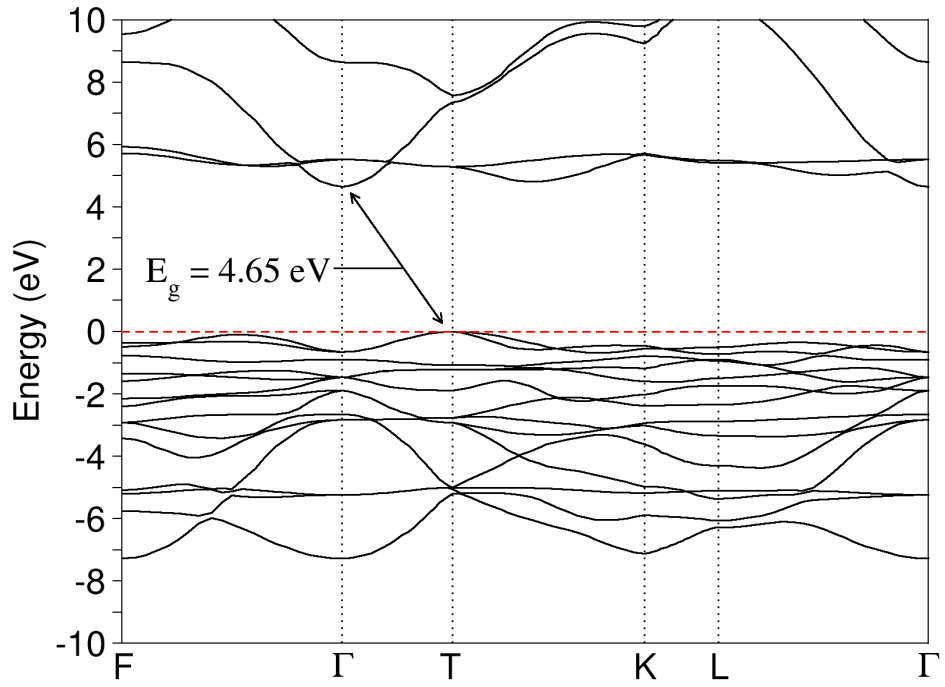

Figure 9. Calculated HSE06 Band Structure of Intrinsic NiO. *Clear similarity is seen between the HSE06 and GGA + U band structures, yet the HSE06 functional, which is thought to be more rigorous, overestimates the experimental band gap in Table 1 considerably. This illustrates the effectiveness of the GGA + U method used in this work. Again, the Fermi Energy is taken to be zero and is indicated by the red dashed line.*

O p and Ni t_{2g} states and a Ni e_g conduction band.[40,98–104] However, some recent works indicate that the lowest energy conduction band is Ni s.[105,106] Here, only a very small contribution of Ni s is shown to be near the CBM, which is predominantly Ni e_g. However, Rödl et al. suggest the dispersive CBM at the Γ point is of s character.[98] In subsequent work, Rödl and Bechstedt concluded from expensive GW calculations, in conjunction with the Bethe-Salpeter Equation, that the first optical transition is intra-atomic from t_{2g} of one Ni site to e_g of the same Ni.[92] The d orbitals of Ni are split into t_{2g} and e_g states by the crystal field induced by the octahedral (O_h) coordination of Ni-O bonds (Section 2.6).

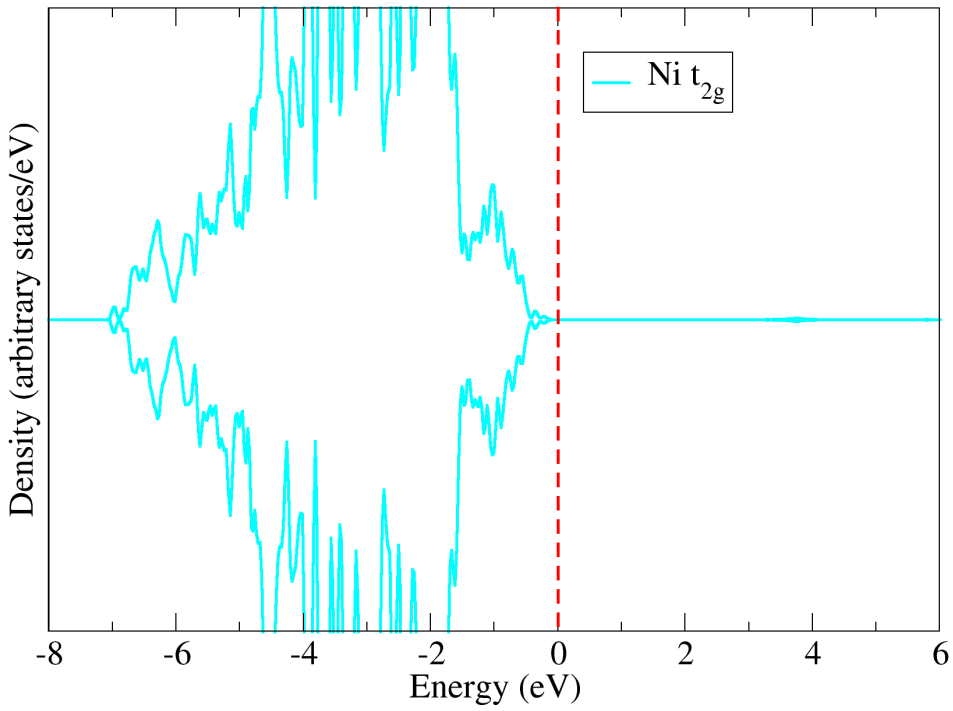

Figure 10. PDOS of Non-Interacting Ni d^3 π Orbital of t_{2g} Symmetry in Intrinsic NiO. *Density is normalized per unit cell. Fermi energy is taken to be zero and is indicated by the red dashed line.*

From a pure crystal-field theory interpretation, the calculations presented here indicate that the VBM is predominantly O p, and the CBM is predominantly e_g, aligning with the charge-transfer insulator point-of-view. However, taking the more rigorous interpretation of ligand field theory, where overlap of metal d orbitals with ligand orbitals is taken into account, in O_h symmetry, it is clear that the t_{2g} orbitals conform to a π bonding set which does not interact with the oxygen. This is evident from decomposing the reducible representation of all possible π orbitals, as shown by Cotton.[107] The result of the decomposition via Equation 2.6.3 becomes

$\Gamma_\pi = 3t_{1g} + 3t_{2g} + 3t_{1u} + 3t_{2u}$.

Of these representations, t_{2g} matches the triplet 3d orbitals of Ni with basis functions xy,

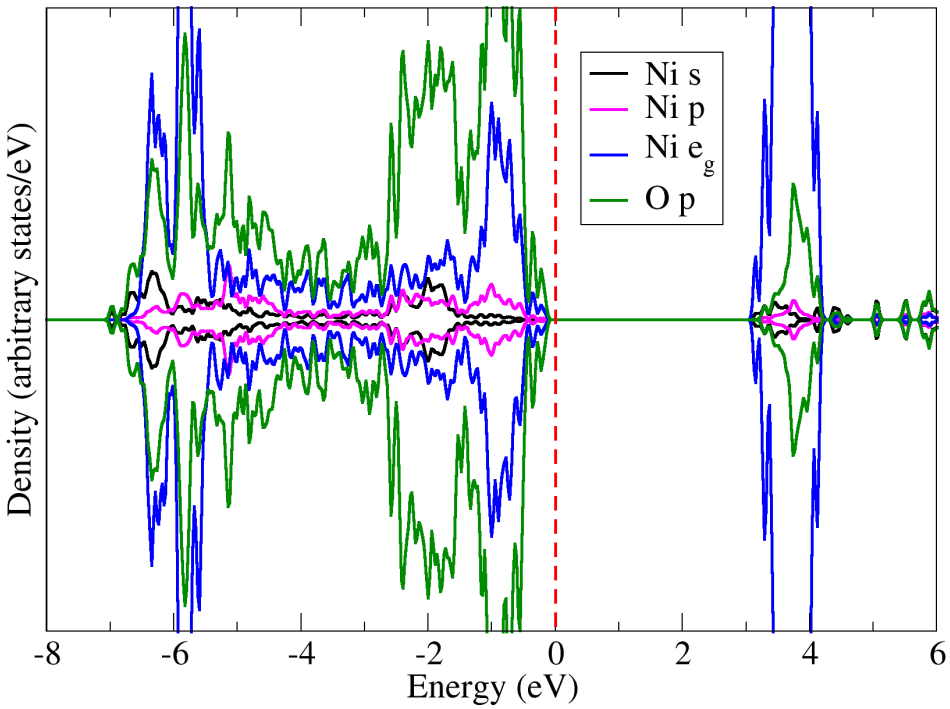

Figure 11. PDOS of the Orbitals involved in σ bonds in Intrinsic NiO. *Density is normalized per unit cell. Fermi energy is taken to be zero and is indicated by the red dashed line.*

xz, and yz, while t_{1u} matches the symmetry of the p orbitals of Ni. The other two representations, while possible mathematically, have no physical meaning. The t_{1u} p orbitals of Ni can be excluded from π bonding, as will be made clear below, so the result is a d^3 Ni π bond of t_{2g} symmetry, which is noninteracting with oxygen. The calculated t_{2g} PDOS is shown in Figure 10, for completeness.

However, it is the s, p, and e_g (d) orbitals of Ni, which overlap with O p in octahedrally-coordinated NiO, creating σ bonds. The σ bonds take precedence over π bonding, so the Ni p orbitals are reserved for this configuration. The PDOS of these orbitals is shown in Figure 11. Again, applying Equation 2.6.3,

$\Gamma_\sigma = a_{1g} + 2e_g + 3t_{1u}$,

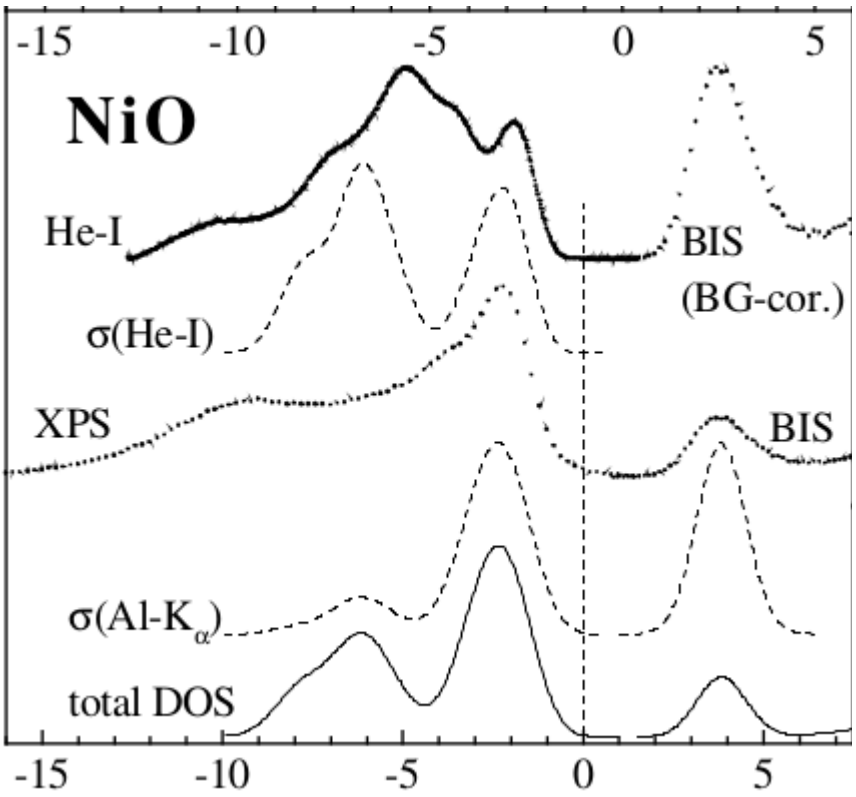

Figure 12. Comparison of measured photoemission with inverse photoemission (BIS) spectra. *Figure adapted from Reference [108].*

where each representation corresponds to a σ bond between O p and Ni s (a_{1g}), Ni d (e_g), and Ni p (t_{1u}). With this interpretation, the valence band maximum (VBM) at the T point is a σ orbital of e_g symmetry. Incidentally, the conduction band minimum (CBM) at Γ is missing any contribution from O p, being solely comprised of Ni s and Ni e_g, making the intra-atomic optical transition of Rödl and Bechstedt appear likely. For the other high-symmetry points, the CBM is clearly composed of a σ* anti-bonding orbital of symmetry e_g. The first optical transition will be investigated further below. For now, comparing DOS with experiment, the bremsstrahlung isochromat spectroscopy (BIS) measurements in Figure 12 of Zimmerman, et al.[108] show two peaks at ~2 eV and ~6 eV below the

VBM, in excellent agreement with PDOS results presented here in Figure 11.

While the e_g orbitals of Ni are only partially filled, giving rise to the AF nature of the material, the t_{2g} orbitals are completely occupied. Locally, the DOS of each Ni lies within a strong ligand field, resulting in a large splitting between the e_g and t_{2g} states, as shown in previous work of Petersen, et al.,[44] and as will be analyzed further in the next section. In addition, results obtained for the real and imaginary parts of the complex dielectric function and related optical properties will be shown, analyzed, and compared with the results of the cases with O vacancies (NiO_y).

3.1.2 O Vacancies in NiO_y

While the conducting filaments (CFs) consist of O vacancies and/or metal precipitates, the most stable defect in NiO is Ni vacancies which give NiO its intrinsic p-type character. However, in RRAM, as the metal electrode scavenges O anions upon an applied threshold voltage, creating the CFs, this results in a Ni-rich condition where 2^+ O vacancies become increasingly more stable at higher Fermi Energies (E_F).[38,109–111] In other words, the O vacancy behaves as a 2^+ charge which bonds with the Ni valence. For this reason, up to a threshold concentration of O vacancies, the system remains insulating. While not labeled explicitly, all O vacancies in this work should be considered 2^+. Therefore, the electrodes should be chosen carefully and may determine whether O ions are scavenged effectively and whether the switching is unipolar or bipolar.[9] Since bipolar switching is desirable, as mentioned above in Section 1.1.1, understanding electronic and dielectric properties in the Ni-rich condition is a large focus of this work.

Since the composition of interest with respect to RRAM is such that O vacancies are present in the bulk, further characterization of NiO with O vacancies by PDOS is presented in Figure 13 and compared to the stoichiometric case. Each supercell with vacancies underwent full ionic relaxation, reducing forces on each ion to < 10 meV/Å. Upon relaxation, the Ni ions move 2.9% closer to the vacancy site than if no vacancy were present, which agrees fully with the findings of Park, et al.[41] Vacancy concentrations considered are 6.25%, 12.5%, and 25% and will be referred to by y = 0.9375, y = 0.875, and y = 0.75, respectively. 2 × 2 × 2 supercells grown in the direction of each lattice vector, consisting of 32 atom supercells were used in the calculation of the PDOS in Figure 13. Figure 13(a) is the case of y = 1 and is displayed for comparison, while Figure 13(b) corresponds to y = 0.9375, 13(c) is y = 0.875, and 13(d) is y = 0.75. In the cases of multiple O vacancies, each O lattice site was tested as a vacancy, until the lowest energy (most thermodynamically stable) configuration was found. Each Ni has prominent crystal field splitting, indicating a strong ligand field, that is reduced at sites which are nearest-neighbor to an O vacancy.

The oxygen vacancy induced levels nearest in energy on either side of the Fermi energy in Figures 13(b) and 13(c) show σ bonded Ni d and O p of symmetry e_g, with a low-lying level occupied by the two orphaned electrons being shared among the six octahedrally-coordinated Ni atoms, making up the new VBM. The other set of introduced energy levels are of Ni e_g character, as well, and lie just below the intrinsic CBM and are unoccupied. Yet, the system remains insulating until a threshold O vacancy limit is reached somewhere between y = 0.875 – 0.75, where the system becomes n-type. In

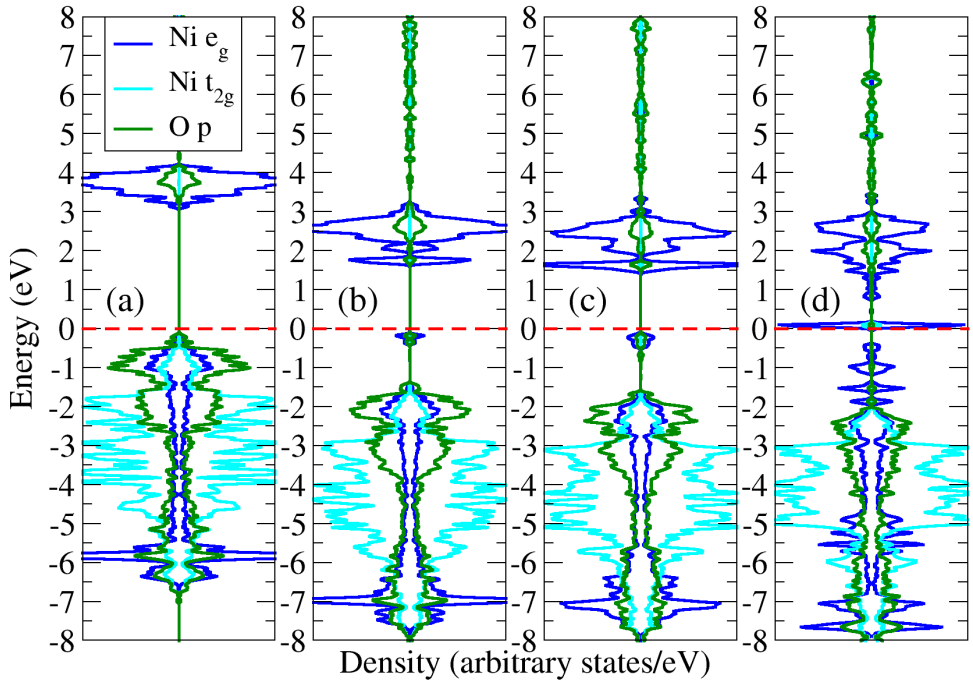

Figure 13. PDOS Showing Crystal Field Splitting in NiO_y. *Ni e_g, Ni t_{2g}, and O p states are shown for (a) y = 1, (b) y = 0.9375, (c) y = 0.875, and (d) y = 0.75. The Fermi energy is taken to be zero and is indicated by the red dashed lines.*

Figure 13(d), for y = 0.75, the O vacancy concentration has crossed the limit, and a Fermi surface of Ni e_g character is introduced. Even though scattering plays a role in resistance, clearly, from the reduced band gap in the electronic structure alone, it can be concluded that the resistance decreases as filamentary stoichiometry is approached, providing further evidence for the filament model of NiO RRAM.

Figure 14 displays the calculated local site-projected density of states (LDOS). In Figure 14(a), the y = 1 case is displayed for comparison. As discussed above, the e_g state is only partially filled. Figure 14(b) is for an arbitrary Ni in the y = 0.9375 concentration, where all states can be seen to be shifted to lower energy. Figure 14(c) shows the LDOS for a Ni which is nearest-neighbor to a vacancy in the y = 0.9375 concentration. In this

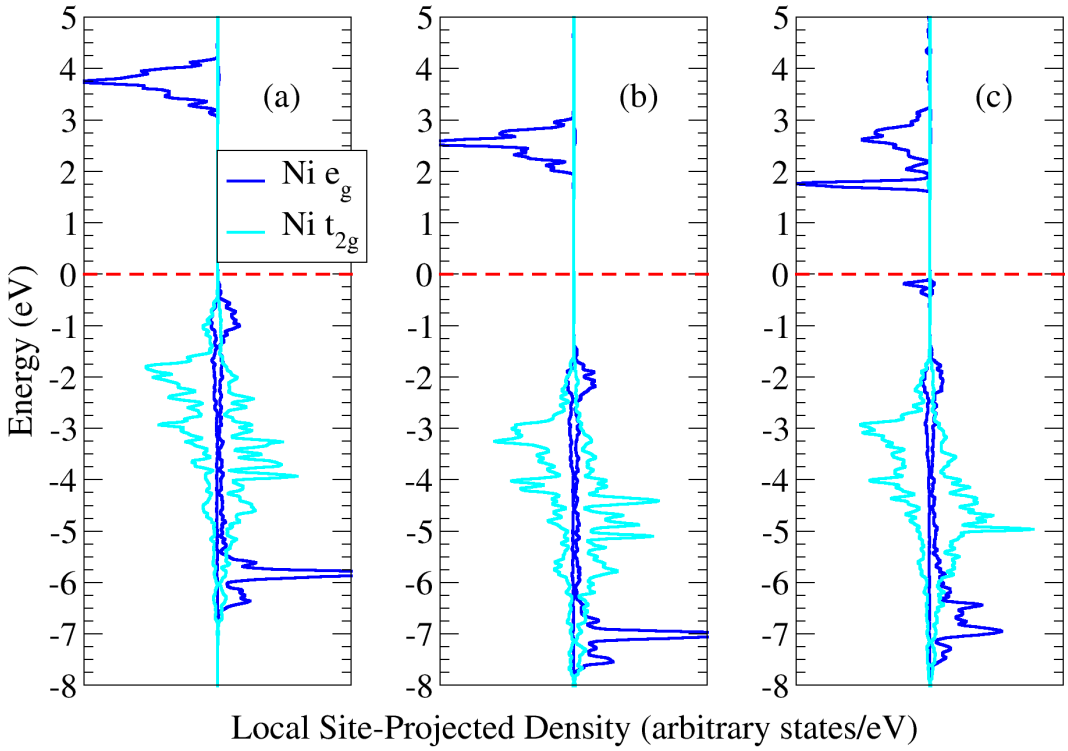

Figure 14. LDOS of NiO_y. *Ni eg and t2g states are shown for (a) arbitrary Ni with y = 1, (b) arbitrary Ni with x = 0.9375, and (c) Ni nearest to an O vacancy with x = 0.9375. The Fermi energy is taken to be zero and is indicated by the red dashed lines.*

case, an alternate spin configuration is found where total spin is reduced by an introduced Ni e_g state originating from the O vacancy. It is this vacancy effect that decreases the band gap. In the band structure for the y = 0.9375 case (one vacancy in the 2 × 2 × 2 unit cell), Figure 15 clearly shows a reduced band gap at the L point which is direct. In this case, the bands comprising the CBM are highly localized, while the VBM shows some dispersion.

While confirming a reduced band gap experimentally would prove challenging in situ during the switching process, using transparent electrodes would make measurements of optical transitions during operation possible. For this reason, calculations of optical

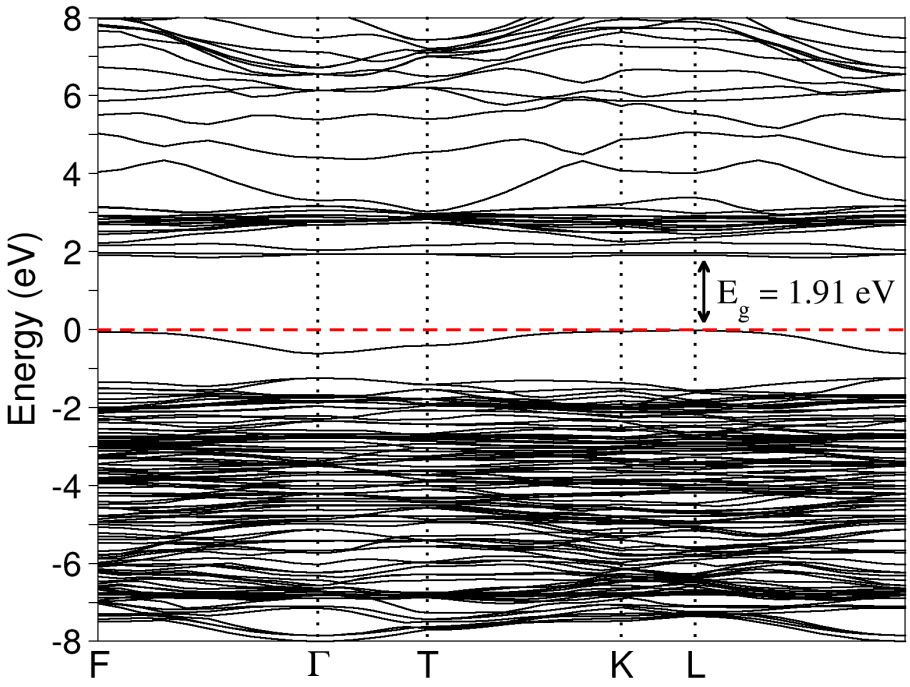

Figure 15: Calculated GGA + U Band Structure of $NiO_{0.9375}$. *Even with just one O vacancy in the unit cell (y = 0.9375), the band gap is reduced significantly to 1.91 eV. Dispersion in the new VBM is evident, yet the reduced band gap is direct at the L point.*

transitions with and without an O vacancy are presented in Figure 16. The PDOS elucidates the type of transition which occurs, and the band structures give an indication of the range of energies allowed for the first optical transitions. While DFT + U cannot provide precise quantitative conduction eigenvalues, qualitative spectral conclusions can be drawn. Figure 16 shows the real and imaginary parts of the complex dielectric function, without (a) and with (b) an O vacancy. The characteristic transition is apparent in both cases, while a lower energy transition can be seen in the case of the O vacancy at the reduced direct band gap energy. This lower energy peak is due to the transition from the occupied O vacancy-induced level to the conduction band. This result was shown for the first time in 2016 by Petersen, et al.[44] Some further analysis is necessary, however.

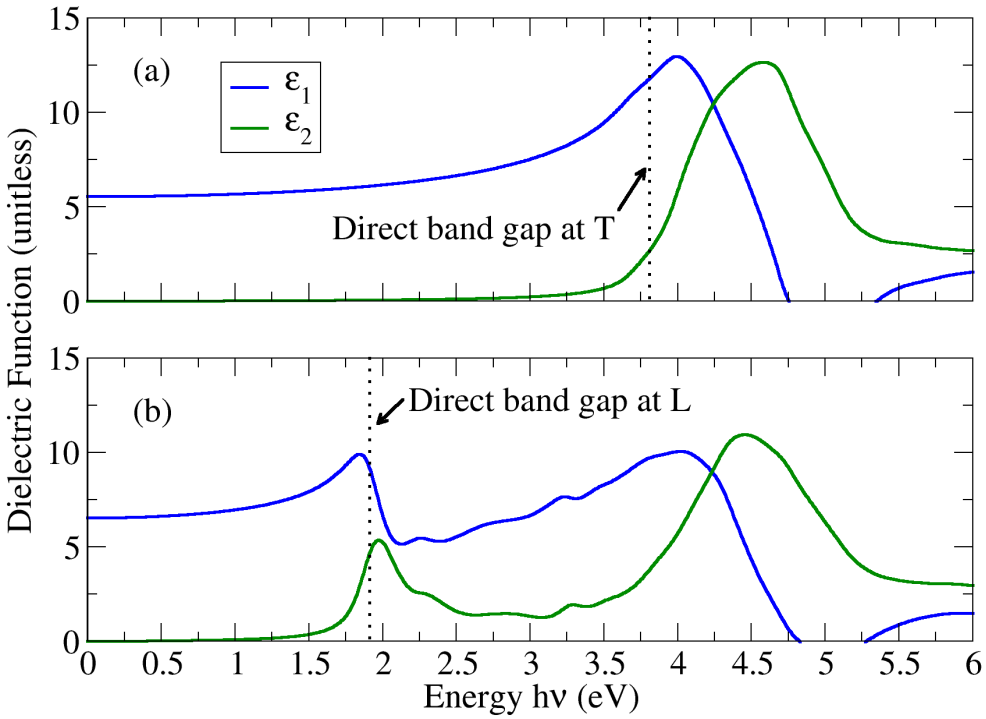

Figure 16. Complex Frequency-Dependent Dielectric Function of NiO and $NiO_{0.9375}$. *Real (ε_1) and imaginary (ε_2) components of the dielectric function were calculated for (a) intrinsic NiO and (b) $NiO_{0.9375}$ with one vacancy in the unit cell (6.25%). A lower energy optical transition is evident in the case with the vacancy.*

Without vacancies, due to the dispersion in the band structure in Figure 8, the direct band gap differs, depending upon which symmetry point is considered, ranging from 3.81 eV at the T point to 4.69 eV at the F point. This range leads to a broad peak in the first series of optical transitions in intrinsic NiO in Figure 16(a). The transitions are evident from the Imaginary component of the frequency-dependent dielectric function (ε_2). The minimum direct band gap at the T point is indicated by a dotted black line at the energy of the onset of the increase of ε_2, and the peak is broad until the direct band gap energy of the F point. From the PDOS in Figure 11, it can be seen that a multitude of transitions should be analyzed to determine which are allowed by electric-dipole

transition selection rules and equation 2.6.3. First, realizing that the perturbing Hamiltonian of the electric-dipole field in Equation 2.6.2 is of symmetry t_{1u} in an O_h crystal-field, a direct matrix product of valence states with t_{1u} yields possible final states of allowed transitions. Rather than treat the orbitals as atomic, due to the evident mixing of states in the valence in particular, here, they are treated as hybrid orbitals, as discussed in Section 3.1.1. Reducible representations were generated from the direct matrix product in Equation 2.6.1. From this result, the decomposition formula (Equation 2.6.3) yields the following two possible transitions:

$t_{1u}\ (\sigma) \leftrightarrow t_{2g}\ (\pi)$;

$e_g\ (\sigma) \leftrightarrow t_{1u}\ (\sigma)$;

It should be mentioned that both of these possibilities are available in the PDOS, as determined in the previous section. Also, the same logic determines that the transitions between even parity states in an electric-dipole perturbative field are not possible, at least at the Γ point.

These results can be compared directly with the cases with O vacancies. In Figure 16(b), the first optical transition is at lower energy, due to the O vacancy-induced reduced direct band gap. The peak in ε_2 shows that this transition is narrower in energy, resulting from the localization of the CBM and narrow range of energy in the dispersion of the VBM. The dotted line indicates the narrowest direct band gap at the L point. The VBM is clearly of e_g symmetry now; so, with this interpretation, there is only one possible transition – e_g to t_{1u}.

However, another interpretation of this transition is that of site-hopping. This is

the typical description of excitation in a transition-metal oxide, where, in this case, an e_g carrier hops from one Ni site to the nearest Ni of opposite spin alignment.[112] This possibility can be understood in terms of a Wannier-Mott exciton, where the radius of the photon-generated electron-hole pair is larger in size than the lattice spacing. Furthermore, the transfer integral can be described by

$$\langle \chi_i | \chi_j \rangle = \cos\left(\frac{\theta_{ij}}{2}\right), \tag{3.1.1}$$

where i and j are initial and final spin states χ, and θ is the angle between them. In the simple collinear approach in this work, clearly the angle can take only one of two values – 0 or π – thus, the transition is possible only for aligned spins where kinetic energy gain is maximized. From Figure 14(a), it is clear that the spin-up channel of e_g of Ni is occupied, while the spin-down channel of e_g is not. Since the nearest Ni will have opposite spin configuration, due to the magnetic ordering, this nearest Ni will have an empty e_g state of aligned spin with the occupied initial Ni e_g state. Similarly, the same argument holds for the case of an O vacancy, although the hopping distance is only from O vacancy site to nearest-neighbor Ni. Certainly, the theoretical methods used in this work could be more rigorous, and the hopping mechanism between e_g states should be confirmed with calculations of exciton radius and oscillator strength of the optical transition.

Frequency-dependent optical properties are analyzed further in Figure 17, where blue lines represent intrinsic NiO, and green lines represent the material with one O vacancy. These properties are calculated by the equations in Appendix A. Figures 17(a) and 17(b) compare the complex refractive index of the two cases, where Figure 17(a) is

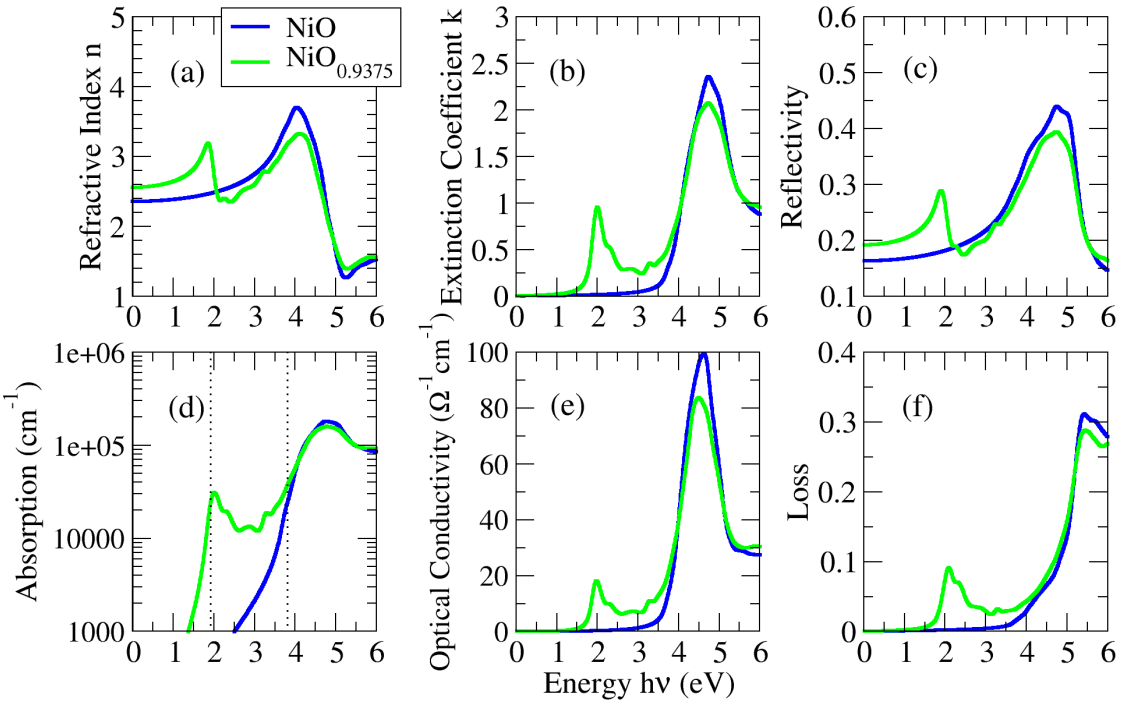

Figure 17. Optical Properties of NiO and $NiO_{0.9375}$. *Here, electronic components of (a) refractive index, (b) extinction coefficient, (c) reflectivity, (d) absorption, (e) optical conductivity, and (f) dielectric loss were calculated for intrinsic NiO (blue) and $NiO_{0.9375}$ with one O vacancy (green). Dotted lines in (d) represent the lowest energy direct band gaps in the respective systems.*

the real part, and Figure 17(b) is the imaginary part or extinction coefficient. Clearly, phase velocity of transmission depends on frequency, and attenuation is evident in the energy ranges of the respective transitions. Reflectivity (Figure 17(c)), which is frequently the optical property directly measured, has local maxima at the transition energies where the greatest reflection occurs. Refractive index, extinction coefficient, reflectivity, and absorption (Figure 17(d)) show excellent agreement with the experimental results of Powell and Spicer.[113] However, their absorption data has several local maxima in a narrow energy range near the lowest energy transition. The theoretical methods used in the present work are limited by numerical approximations which cannot

Table 2. Static Dielectric Constant of NiO_y. *LFE indicates whether local field effects were taken into account or not.*

	y = 1	y = 0.9375	y = 0.875
IPA without LFE	5.76	6.36	7.05
IPA with LFE	5.81	6.43	7.22
DFPT	7.59	7.95	8.16
Total ε(0)	13.4	14.38	15.38

necessarily distinguish between peaks in such a narrow energy range; however, the analysis presented above indicates that these transitions are characteristic of the several direct band gaps at high-symmetry points in the Brillouin zone. The real optical conductivity in Figure 17(e), related to the electric field strength corresponding to dielectric breakdown, shows peaks associated with the transition energies, as expected, indicating the energy at which electronic excitation occurs. The peaks in dielectric loss in Figure 17(f) display the energies at which electromagnetic energy is dissipated electronically. It is not surprising that this occurs at the energies corresponding to optical transitions.

While much information can be gleaned from frequency-dependent optical properties, device operation of RRAM is below infra-red frequency, so static values of the dielectric constant $\epsilon_{ij}^{\infty}=\epsilon_{ij}(0)$ are calculated for the case of zero, one, and two vacancies, i.e., y = 1, 0.9375, and 0.875. Electronic and ionic contributions are calculated separately, totaled, and compared in Table 2. A clear trend of increasing dielectric constant is evident as O vacancy concentration is increased. Local field effects play a small role in NiO, but the ionic and electronic contributions to the static dielectric

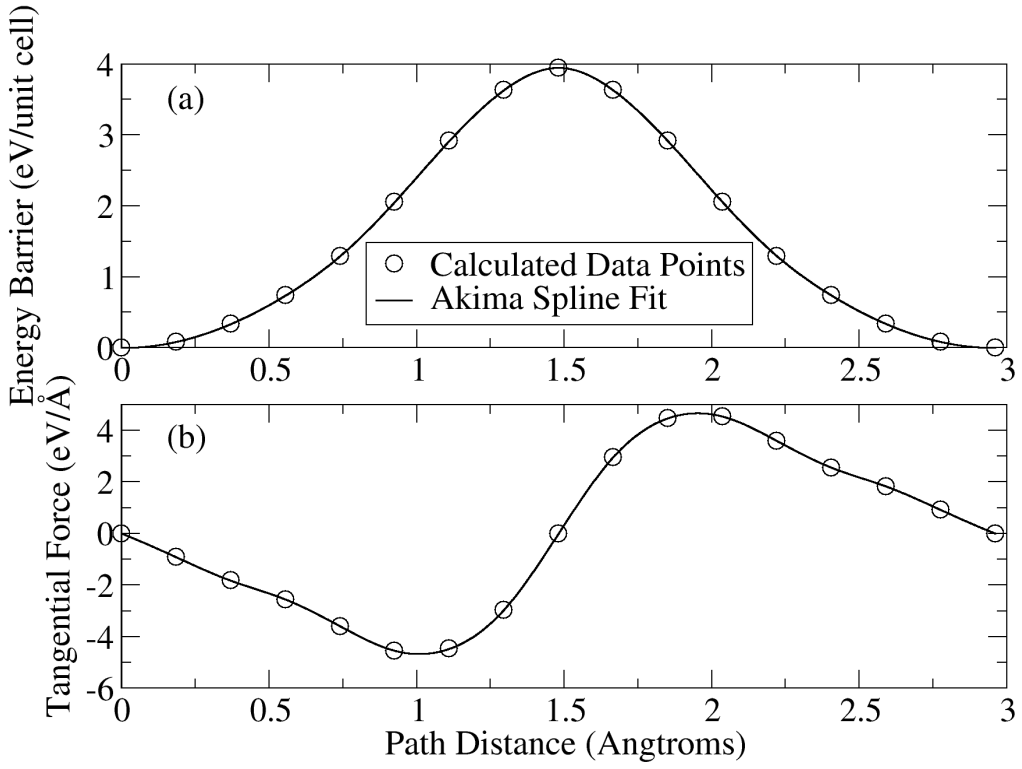

Figure 18. Nudged Elastic Band Calculations of O Diffusion in the [110] Direction of NiO. *Energy barrier (a) and tangential force (b) are fit to Akima splines, so extrema can be seen clearly.*

constants are quite different. The majority of the static electric field impeded by the material is due to vibronic interactions or polarization which is enhanced by O vacancies.

While comparing the static dielectric constants may give an indication of the ease of diffusion of O,[114] a more rigorous method is to calculate energy barriers and tangential forces of O diffusion. Both were calculated here within the Nudged Elastic Band Method,[47] in the case of y = 0.75 (1 vacancy in an 8 atom cell, leaving 7 atoms), and the results can be seen in Figure 18, where data points were fit with Akima splines. The peak energy barrier in the [110] direction – the energy required to move an O ion from one lattice site to the nearest-neighboring non-Ni site – was found to be approximately 4 eV

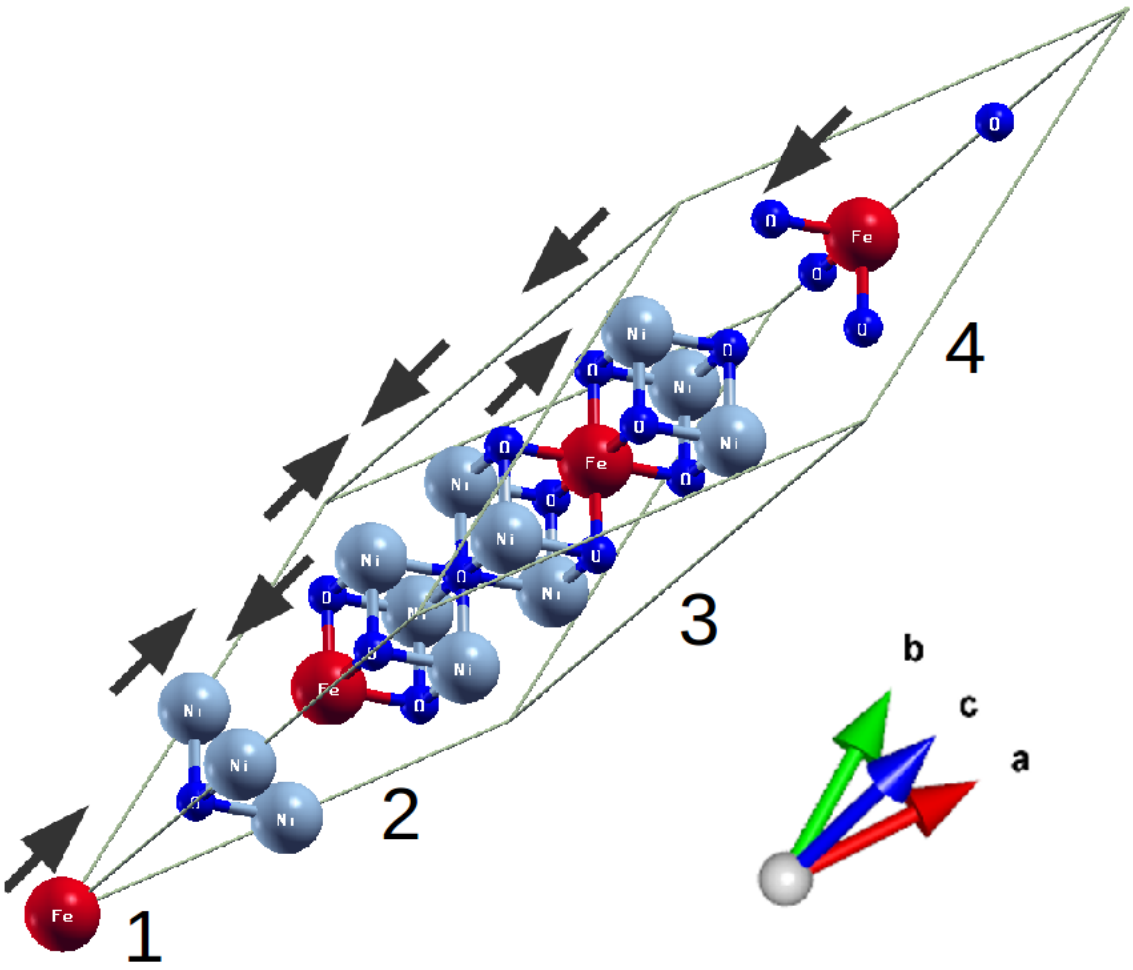

Figure 19. Supercell of 32 atom $Ni_{1-x}Fe_xO$. *Fe is red, Ni is gray, and O is blue. The cell is outlined in gray. Black arrows indicate local dipole moments of metal ions in the (111) planes, and colored arrows indicate the lattice vectors. Numbers indicate the order in which added Fe atoms orient in the supercell, according to enthalpy.*

per cubic unit cell in Figure 18(a). The force curve required to overcome such a barrier is shown in Figure 18(b) and was calculated from Equation 2.7.1. The peak force has a magnitude of approximately 4 eV/Å.

The energy barrier of diffusion of O (vacancies) of NiO_y, $Ni_{1-x}Fe_xO_y$, and $Ni_{1-x}Co_xO_y$ will be compared at the end of the following section. Electronic and optical properties will be analyzed for NiO_y and $Ni_{1-x}Fe_xO_y$ as well, with particular emphasis on

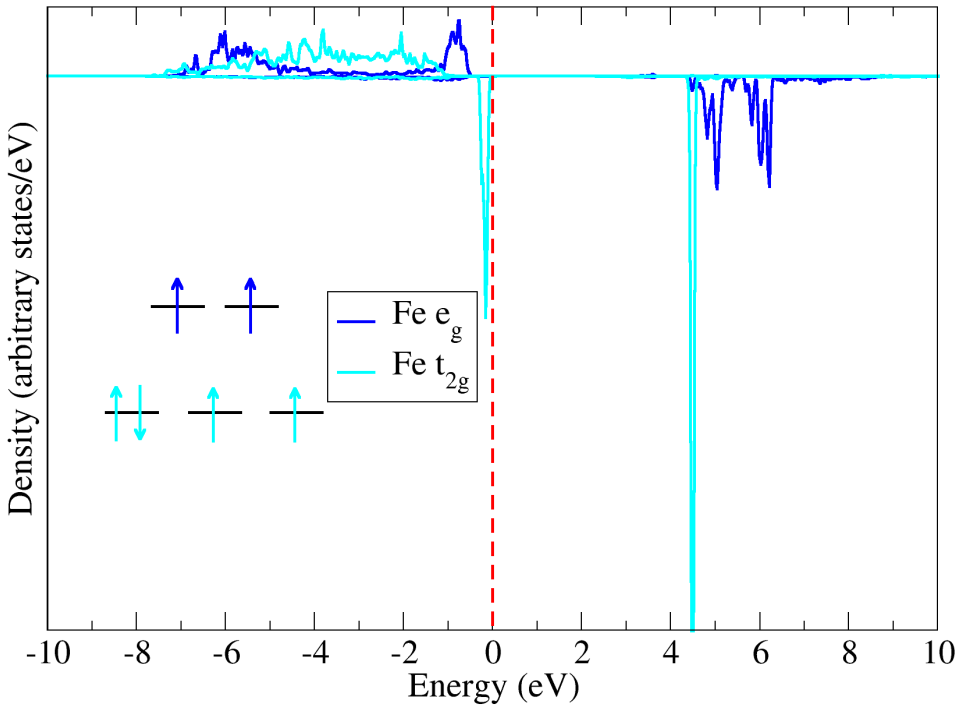

Figure 20. LDOS of d orbitals for Fe impurity in NiO. *Arrows indicate the spin of the filling of d orbitals in the octahedral field. The Fermi energy is taken to be zero and is indicated by the red dashed line.*

whether addition of Fe improves RRAM operation.

3.2 $Ni_{1-x}Fe_xO_y$ (Fe:NiO)

For purpose of comparison, the same 32 atom unit cell was used in the case of $Ni_{1-x}Fe_xO_y$ as with NiO_y. Thus, the BZ is the same, as well. Fe $4s^2 3d^6$ electrons were treated as valence in the PBE-generated PAWs, whereas inner orbitals were taken to be frozen in the core. Again, energy cutoff was chosen to be 320 eV, with a gamma-centered 4 × 4 × 4 k-point mesh. Since little experimental data is available for $Ni_{1-x}Fe_xO$, and almost no theoretical work, an effective U – J value cannot be determined empirically. For this

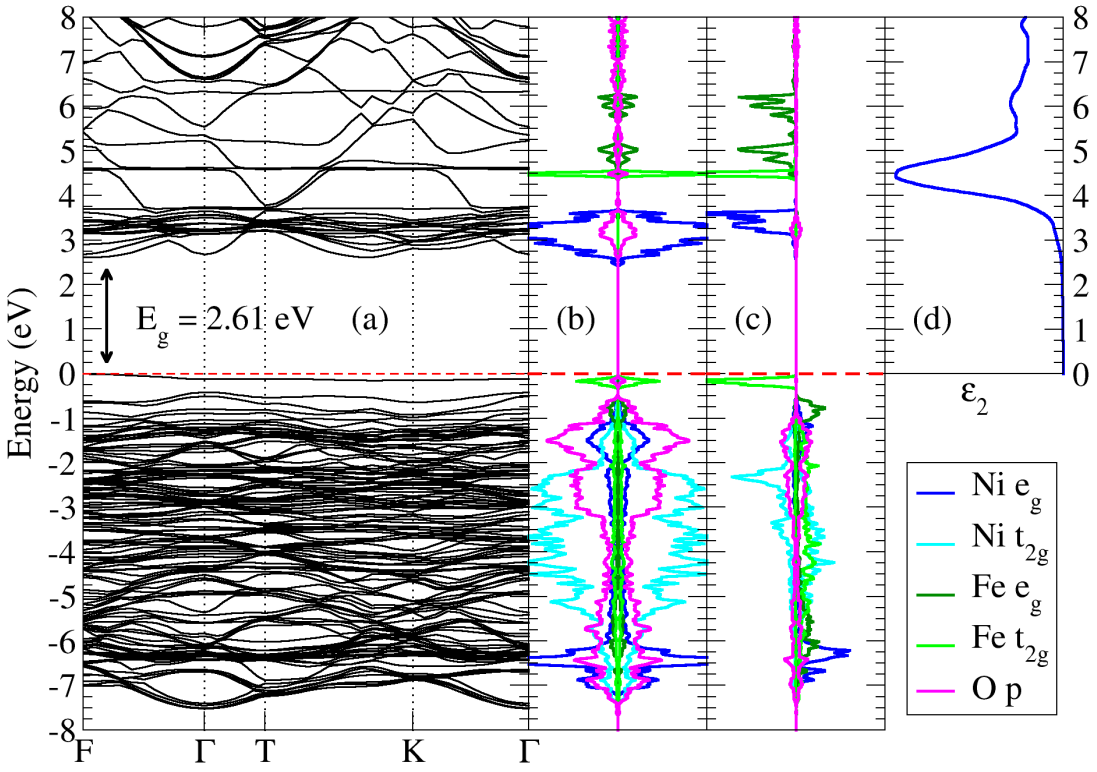

Figure 21. Electronic Structure and First Optical Transition of $Ni_{0.875}Fe_{0.125}O$. *Shown is the (a) band structure, (b) PDOS, (c) LDOS, and (d) the imaginary component of the dielectric function ε_2. The arrows indicate the direct energy band gap in the band structure at the F point. The Fermi energy is taken to be zero and is indicated by the red dashed line. The density of the LDOS in (c) is magnified 3 times the density of the PDOS in (b) for illustrative purposes.*

reason, the same value for Fe as Ni of 5.3 eV is used throughout this work. Due to the excellent description of physical properties of NiO_y with DFT + U, highly expensive HSE06 calculations – which significantly overestimate the band gap in NiO – are not performed on the present system doped with Fe.

Due to Fe having greater magnetic susceptibility than Ni, an even number of Fe must be present in the unit cell to ensure a net magnetic moment of zero in the AF system. Therefore, Fe concentrations of x = 0.125 and x = 0.25 are presented here,

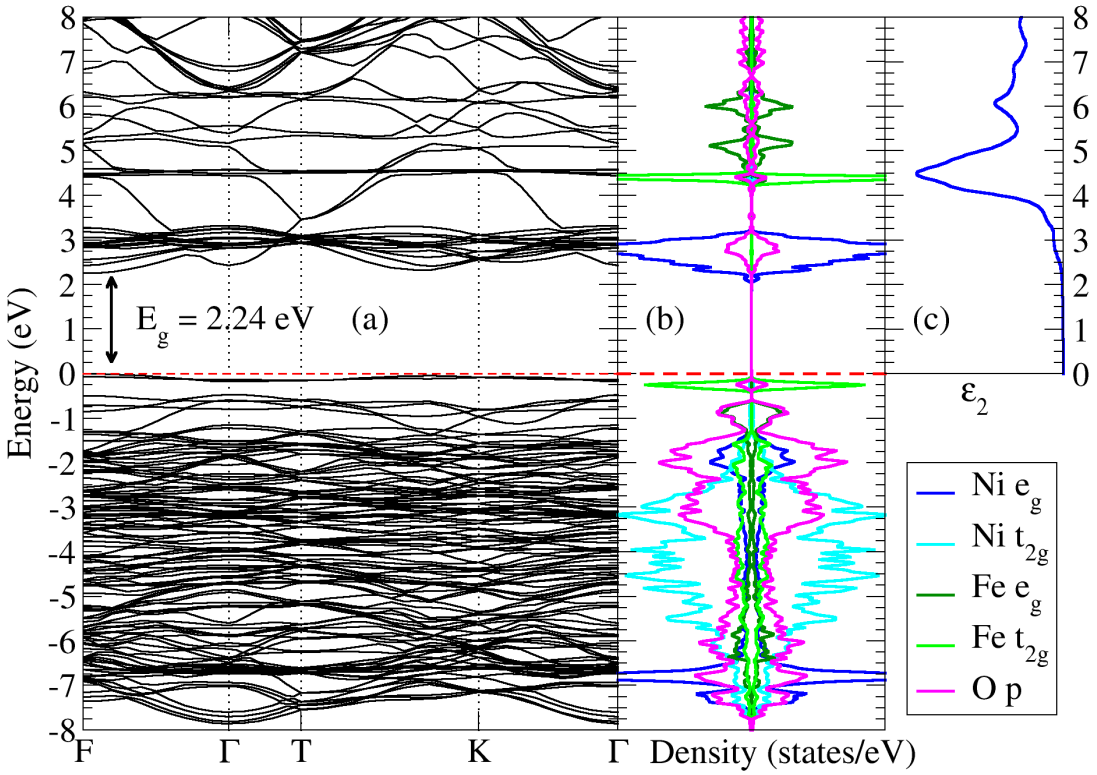

Figure 22. Electronic Structure and First Optical Transition of $Ni_{0.75}Fe_{0.25}O$. *Shown is the (a) band structure, (b) PDOS, and (c) the imaginary component of the dielectric function ε_2. The arrows indicate the direct energy band gap in the band structure at the F point. The Fermi energy is taken to be zero and is indicated by the red dashed line.*

corresponding to two and four Fe in the unit cell. Ground state energy was calculated, adding one Fe at a time to all possible lattice sites, in order to obtain the atomic positions of the most thermodynamically stable configuration. The resulting Fe positions are shown in the unit cell of Figure 19, where Fe replaced Ni directly, and the supercell underwent ionic relaxation to reduce forces on each ion to < 20 meV/Å. O ions move < 1% away from the Fe impurity sites. The 1 and 2 in Figure 19 correspond to the most stable configuration of two Fe in the x = 0.125 system, whereas 1-4 represent the four most stable Fe positions in the x = 0.25 composition.

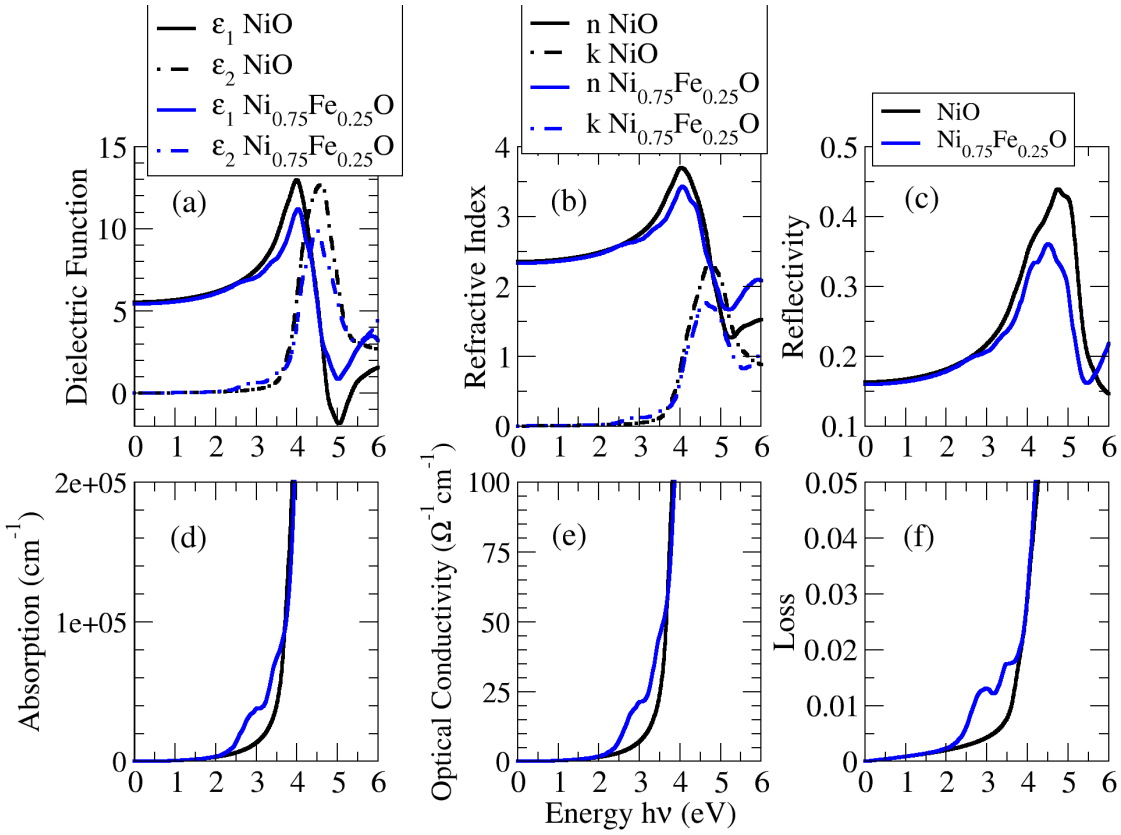

Figure 23. Optical properties of NiO vs $Ni_{0.75}Fe_{0.25}O$. *Shown is (a) the complex dielectric function, (b) complex refractive index, (c) reflectivity, (d) absorption, (e) optical conductivity, and (f) dielectric loss. Figure adapted from Petersen, et al.*[115]

3.2.1 $Ni_{1-x}Fe_xO$ Without Vacancies

For both x = 0.125 and 0.25, the magnitude of the magnetic dipole moments of Ni and Fe sites is found to be 1.70 and 3.75 Bohr magnetons, respectively, with the AF-aligned magnetic dipole moments summing to a net magnetization of zero in the ground state. As can be seen from the LDOS in Figure 20, the $3d^6$ electrons in Fe take on a vastly different role than the $3d^8$ electrons in Ni upon substitution in the lattice. The much larger magnetic dipole moment of Fe results from the high spin configuration. The arrows in the

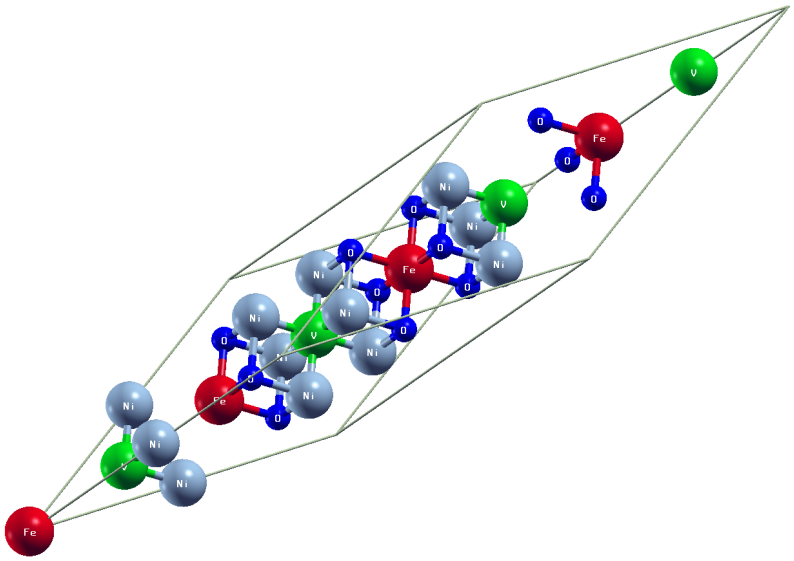

Figure 24. $Ni_{1-x}Fe_xO_y$ Supercell. *Ni are gray, Fe are red, O are blue, and O vacancy sites are green.*

figure indicate the filling, where the three spin-up electrons in the t_{2g} symmetry form a d^3 π bond, similar to what is seen in intrinsic NiO. However, the one spin-down t_{2g} electron is unpaired yet completely occupied. Two spin-up e_g electrons can be seen in the LDOS, as well. Clearly, without an even number of Fe impurities in the cell which are antiferromagnetically aligned, the experimentally observed net magnetization of zero would not be present.

With the ground state accurately described, the band structure was calculated, first for the case without O vacancies (Figure 21(a)), for $Ni_{0.875}Fe_{0.125}O$. With the substitution of Fe, the indirect band gap of NiO becomes direct at the F point. While the minimum direct energy band gap of intrinsic NiO was calculated to be 3.81 eV at the T point, $Ni_{0.875}Fe_{0.125}O$ has a direct band gap of 2.61 eV. A highly-localized band is introduced with the addition of Fe at the VBM. To characterize this band, along with the rest of the electronic structure, calculated PDOS and LDOS are shown in Figures 21(b) and 21(c),

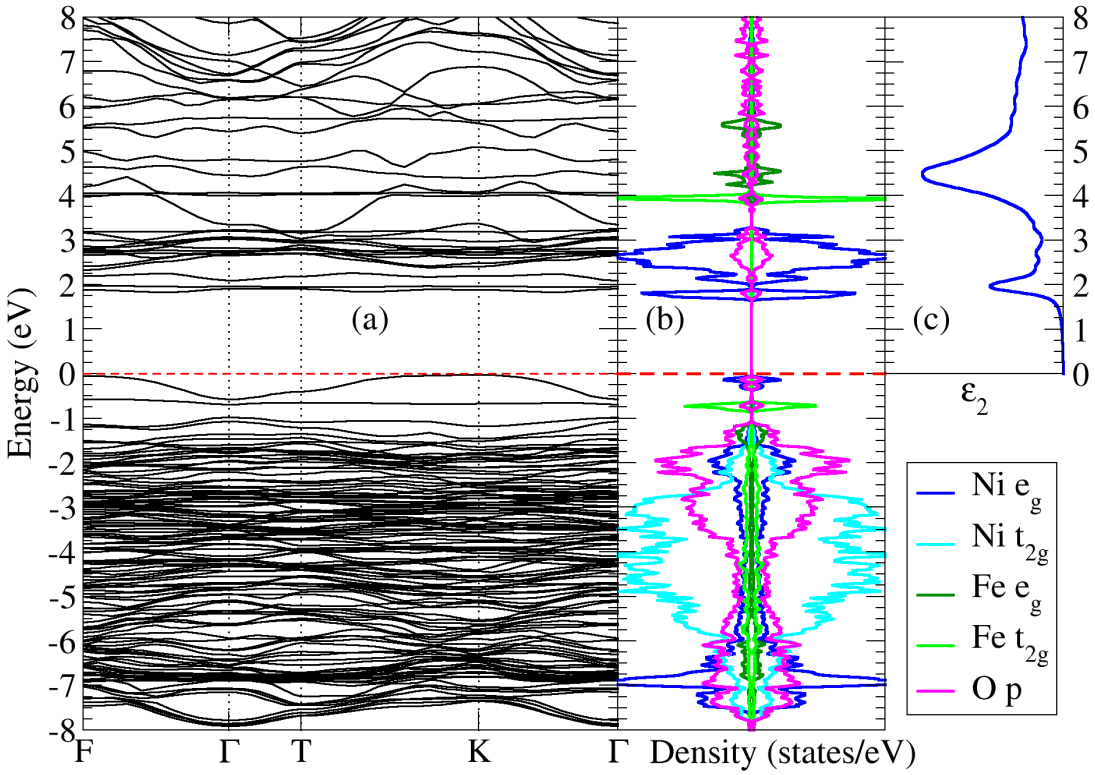

Figure 25. Electronic Structure and ε_2 in $Ni_{0.875}Fe_{0.125}O_{0.9375}$. *The (a) band structure, (b) PDOS, and (c) imaginary part of the dielectric function are shown.*

respectively. This reduction in the band gap from the t_{2g} level of Fe has little effect on the optical properties, as can be seen from the onset of ε_2 in Figure 21(d).

Figure 22 shows a similar figure for x = 0.25. In Figure 22(a), the direct band gap can be seen to be reduced by 0.37 eV from the x = 0.125 concentration. Figure 22(b) displays the calculated PDOS which differs only from the lesser concentration by having more density of Fe levels. In Figure 22(c), the first optical transition can be seen to occur at lower frequency, as expected with the reduced energy band gap. At first glance, this may be misleading, however. The lone spin-down t_{2g} electron of the VBM neither bonds with O nor participates in the first optical transition, nor does it create a Fermi surface. Octahedral symmetry forbids an electric-dipole transition from a state with t_{2g} symmetry

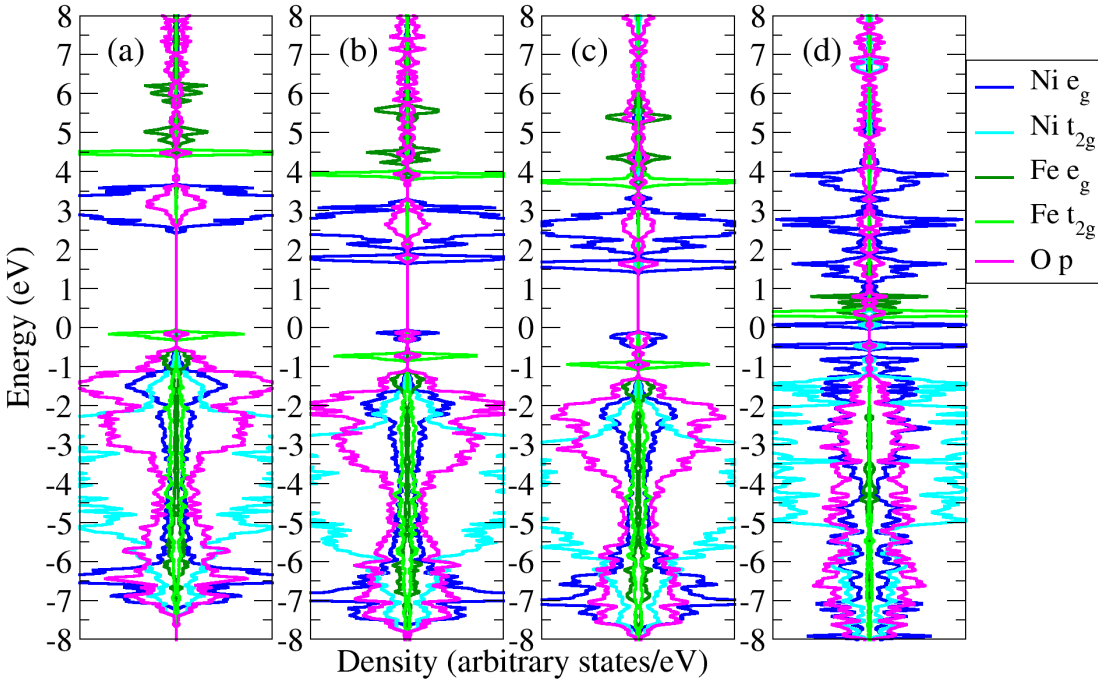

Figure 26. PDOS of $Ni_{0.875}Fe_{0.125}NiO_y$. *Here, (a) displays y = 1, (b) y = 0.0625, (c) y = 0.125, and (d) 0.25.*

to one of e_g, so the first optical transition is nearly identical to that of intrinsic NiO – again, the transition can be interpreted as being from t_{1u} to e_g. The transitions can be seen further in Figures 23(a) – (f), adapted from Petersen, et al.,[115] where peaks in optical properties, such as absorption, are at lower energy than NiO, merely due to the lowering of energy of the anti-bonding e_g state in the CBM, consisting of Ni e_g and O p. Again, however, the hopping transition in Equation 3.1.1 from e_g of one Ni to e_g of the next Ni along the bonding direction gives a more accurate description, assuming the created exciton is sufficiently large.

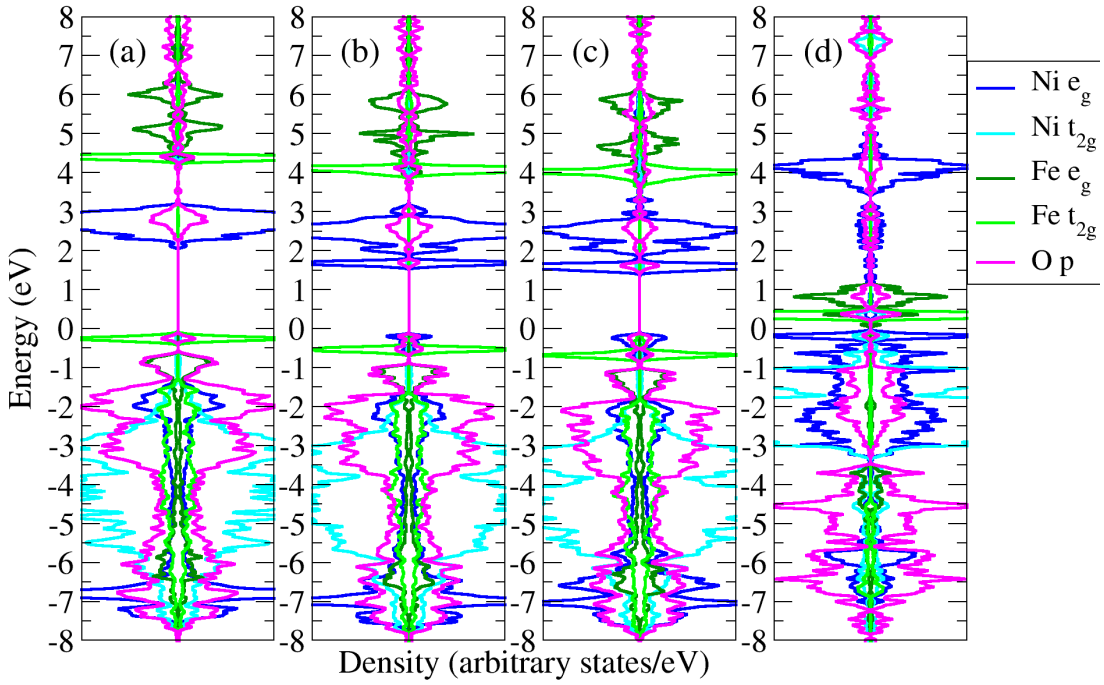

Figure 27. PDOS of $Ni_{0.75}Fe_{0.25}NiO_y$. *Here, (a) displays y = 1, (b) y = 0.0625, (c) y = 0.125, and (d) 0.25.*

3.2.1 $Ni_{1-x}Fe_xO_y$ With O Vacancies

As was done for the Fe impurities, O vacancy sites were tested for thermodynamic stability, where the most stable positions are indicated in green in Figure 24. It should be noted that the vacancy sites are most stable adjacent to Ni sites, rather than Fe sites. This is due to the propensity of Fe to have a higher oxidation state than Ni. Again, the Ni sites move closer to the 2^+ vacancy sites upon relaxation.

Contrary to NiO_y and $Ni_{1-x}Fe_xO$, the energy band gap of $Ni_{0.875}Fe_{0.125}O_{0.9375}$ in Figure 25(a) is indirect. The t_{2g} Fe d level (Figure 25(b)) is still highly localized in the valence, but it is no longer the VBM. As in NiO_y, the e_g Ni d and t_{1u} O p hybridize to an anti-bonding σ state of e_g symmetry, comprising the new VBM, which exhibits

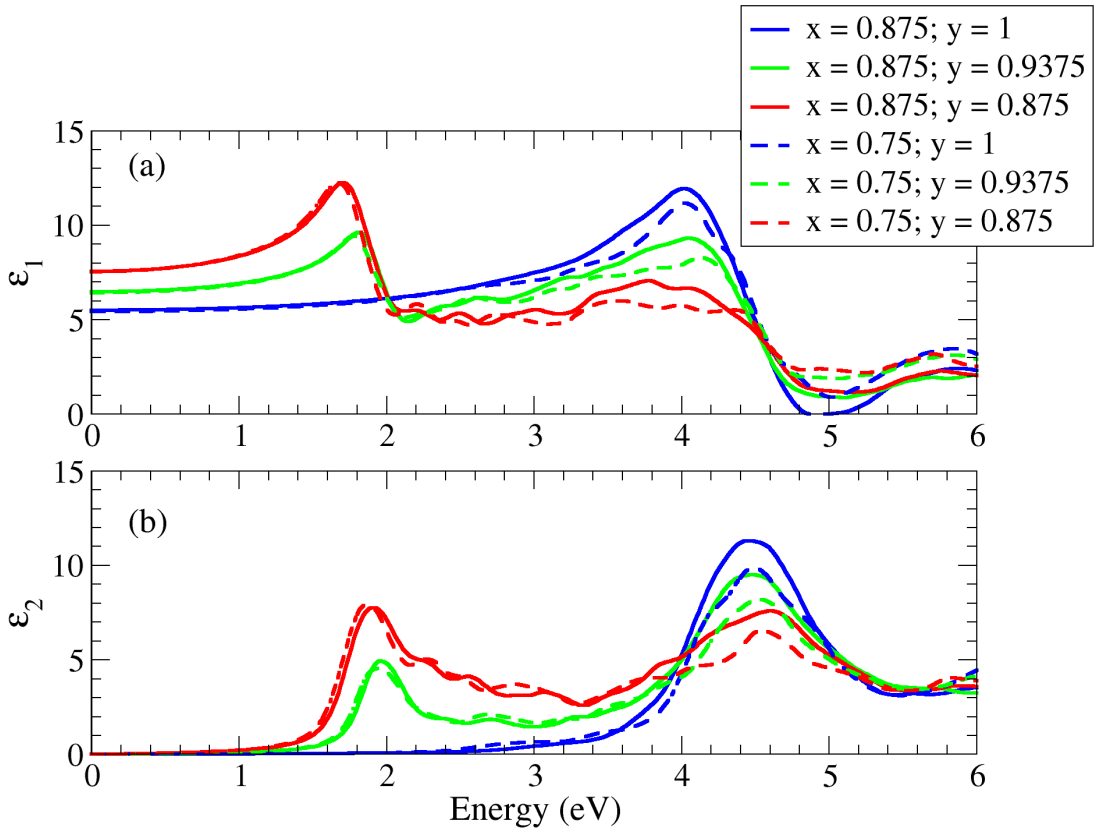

Figure 28. Frequency-Dependent Complex Dielectric Function of $Ni_{1-x}Fe_xNiO_y$. *The figures (a) show the calculated real component and (b) the imaginary component for various concentrations of Fe dopants and O vacancies.*

substantial dispersion in the band structure. Again, the only possible electric-dipole transition from this state is to the anti-bonding t_{1u} σ state in the CBM, comprised of the p orbitals of Ni and O. However, again, the site-hopping transition of Equation 3.1.1 is a strong possibility.

Depending on Ni site location in the supercell relative to O vacancies, e_g Ni d states take on various energy levels in the $Ni_{0.875}Fe_{0.125}NiO_y$ PDOS, as is evident in Figure 26. Figure 26(a) is the y = 1 case for reference, and Figures 26(b), 26(c), and 26(d) increase O vacancy concentration as y = 0.9375, y = 0.875, and y = 0.75, respectively.

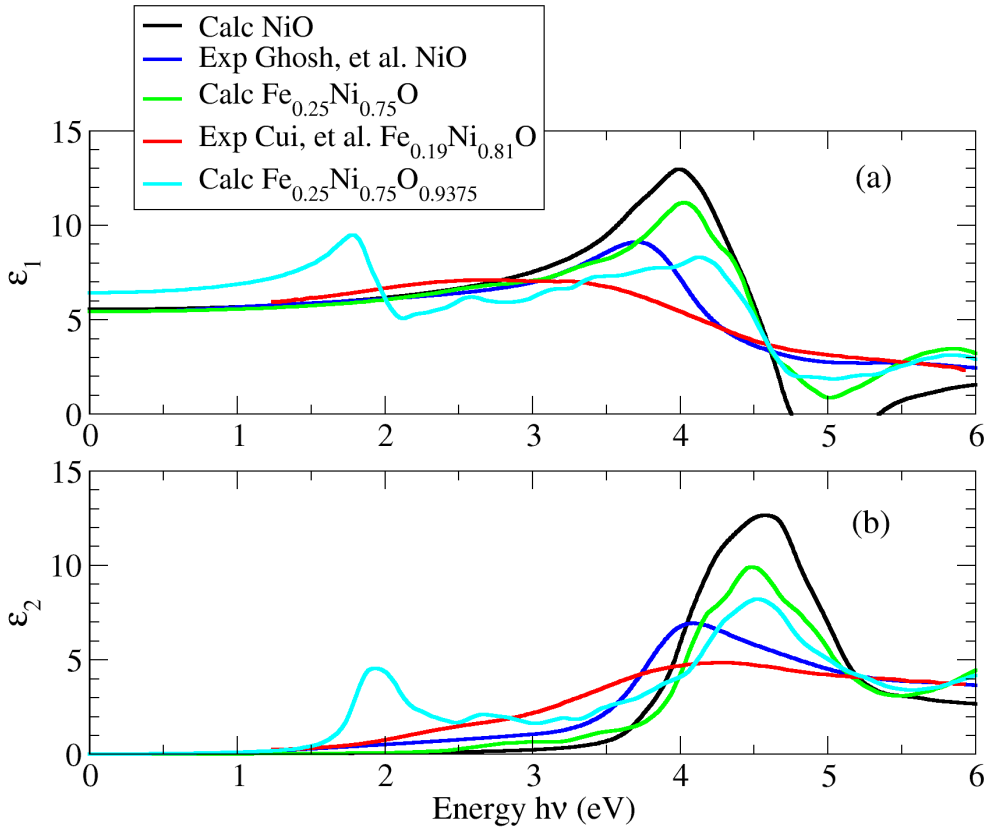

Figure 29: Calculated NiO and $Ni_{1-x}Fe_xO_y$ vs Experiment. *The figures (a) show the calculated real component and (b) the imaginary component for various concentrations of Fe dopants and O vacancies.*

Clearly, the energy band gap decreases with increasing O vacancy concentration. A combination of e_g Ni d and t_{1u} O p comprise the new VBM, with the t_{2g} Fe d state brought to a lower energy level, until y = 0.75, where a Fermi surface and a reorganization of states can be seen. Figures 27(a), (b), (c), and (d) show little difference in electronic structure upon doubling Fe concentration in NiO.

To further analyze the trend of various concentrations of Fe dopants and O vacancies, the complex dielectric function is shown in Figure 28 for various concentrations. The real portion of the static value (Figure 28(a)) clearly increases as O

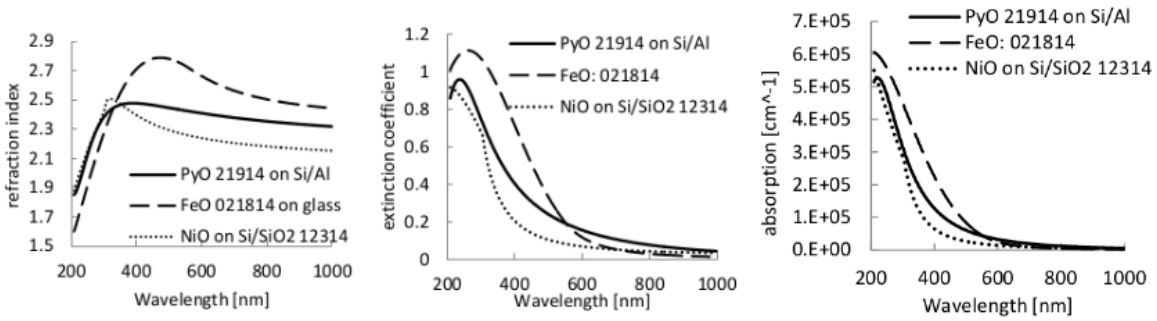

Figure 30. Experimental optical properties of $Ni_{1-x}Fe_xO$ (PyO). *Figure adapted from Reference [48].*

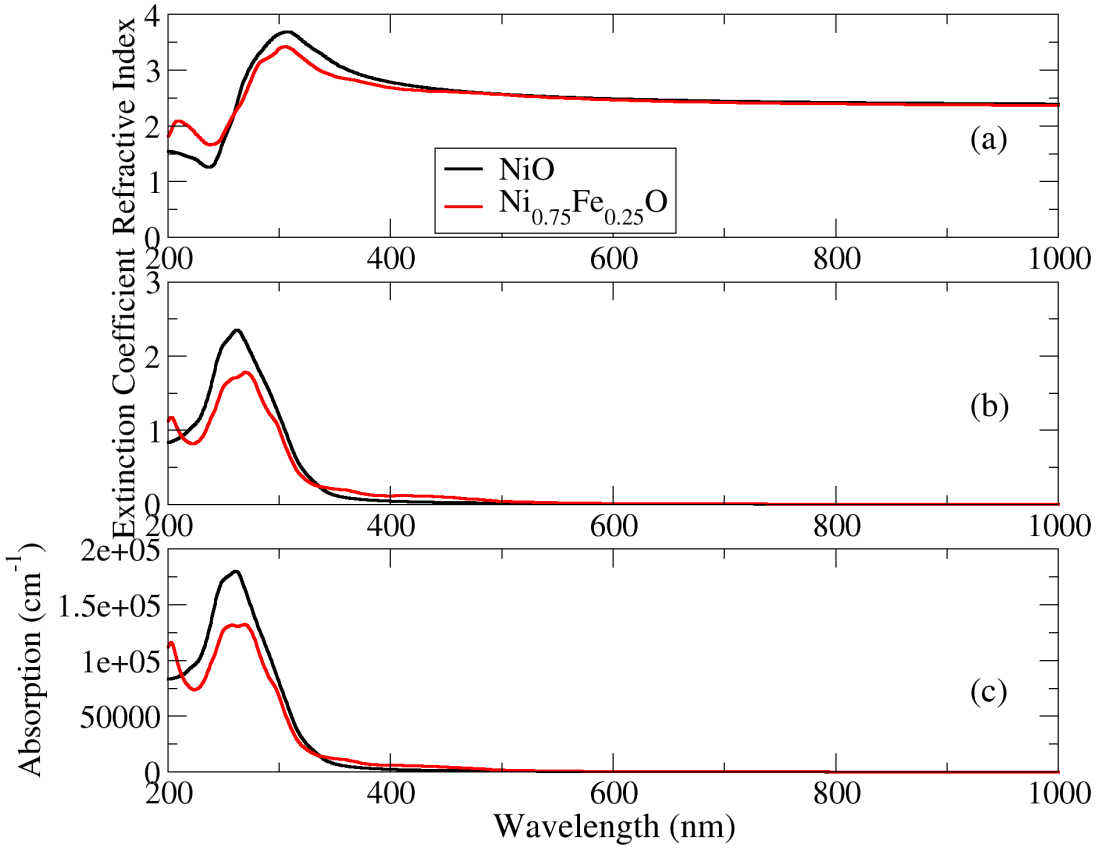

Figure 31. Calculated Optical Properties of NiO vs $Ni_{0.75}Fe_{0.25}O$. *Shown is (a) refractive index, (b) extinction coefficient, and (c) absorption.*

vacancy concentration increases. The greater concentration of O vacancies indicate greater intensity (Figure 28(b)) in the first transition and a decreased intensity in the second. In Figure 29, some experimental data is compared to the calculations of the

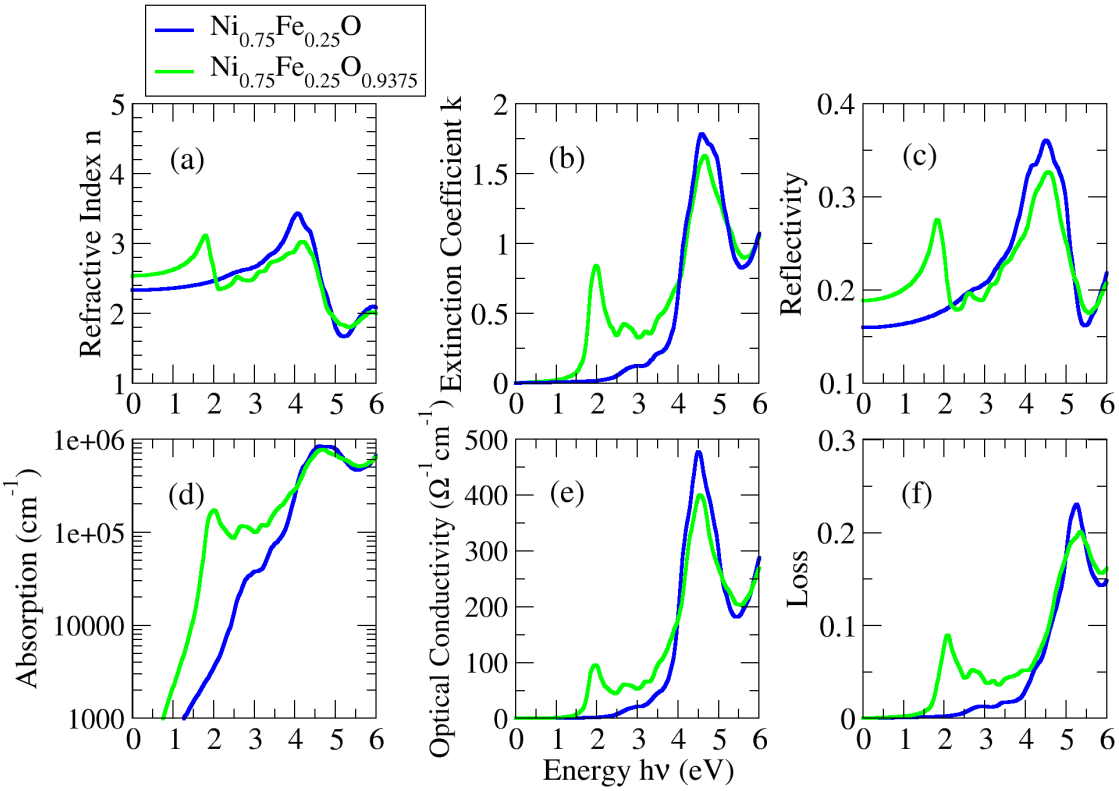

Figure 32. Optical properties of $Ni_{0.75}Fe_{0.25}O$ vs $Ni_{0.75}Fe_{0.25}O_{0.9375}$. *Shown is (a) refractive index, (b) extinction coefficient, (c) reflectivity, (d) absorption, (e) optical conductivity, and (f) dielectric loss.*

frequency-dependent complex dielectric function of this work. For intrinsic NiO, reasonable agreement can be seen with the measurements of Ghosh, et al.[105] However, the calculated peak in the real component in Figure 29(a) is substantially greater, broader, and at higher energy. The energetic difference could be explained by the chosen values for the effective Hubbard potential U-J of Ni and Fe, as the band gap is particularly sensitive to this value. A possibility for the greater peak could be the neglected local field effects (LFE Section 2.4), which can cause an underestimation of field screening.[92] Stoichiometries of the two experimental samples are unknown, so it is difficult to compare the case of O vacancies with experiment. Furthermore, the peak in

Table 3. Calculated Real Static Dielectric Constants for $Ni_{1-x}Fe_xO_y$. *The first column, which does not include local-field effects (LFE), is not included in the total.*

	$\varepsilon_{ij}(0)$ no LFE	$\varepsilon_{ij}(0)$ with LFE	ε_∞	total
NiO	5.76	5.81	7.60	13.41
$NiO_{0.9375}$	6.36	6.43	7.95	14.38
$NiO_{0.875}$	7.05	7.22	8.16	15.38
$Ni_{0.875}Fe_{0.125}O$	5.70	5.74	7.46	13.20
$Ni_{0.875}Fe_{0.125}O_{0.9375}$	6.30	6.37	8.06	14.43
$Ni_{0.875}Fe_{0.125}O_{0.875}$	7.01	7.18	8.14	15.32
$Ni_{0.75}Fe_{0.25}O$	5.63	5.67	7.60	13.27
$Ni_{0.75}Fe_{0.25}O_{0.9375}$	6.24	6.31	7.89	14.20
$Ni_{0.75}Fe_{0.25}O_{0.875}$	6.93	7.11	7.99	15.10

the measurement of $Ni_{0.81}Fe_{0.19}NiO$ of Cui et al.[116] is difficult to discern.

Therefore, the next comparison is with optical measurements of Compton, et al. on $Ni_{1-x}Fe_xO$.[48] Excellent agreement can be seen with measured values in Figure 30 and calculated values in Figure 31, where all peaks for $Ni_{1-x}Fe_xO$ are lower than those from NiO. However, again, stoichiometry of measured samples is unknown. Further calculated optical properties are shown in Figure 32. The first transition due to the oxygen vacancy is evident.

In addition to frequency dependent optical properties, the static dielectric constant was calculated within DFPT and tabulated in Table 3 for different concentrations of Fe impurities and O vacancies. Here, the electronic and vibronic quantities are totaled to give $\varepsilon_\infty(0)$. It is clear that the increase in dielectric constant with increase in O vacancy concentration is independent of Fe concentration in the compositions considered. As Fe concentration is increased, the dielectric constant slightly decreases, even though intrinsic FeO has about twice the dielectric constant as NiO.[117]

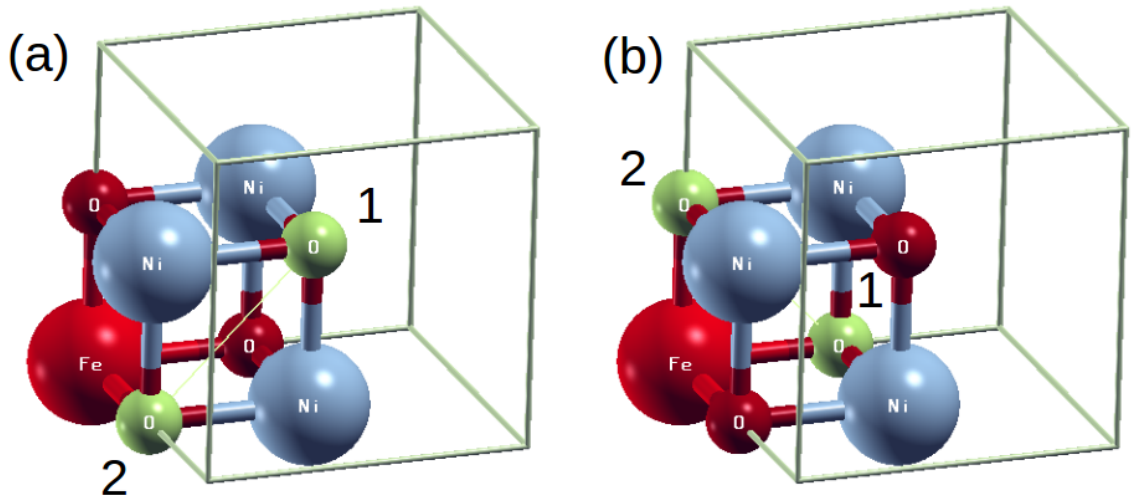

Figure 33. Two O diffusion paths in $Ni_{0.75}Fe_{0.25}O_{0.75}$. *Ni is gray, Fe or Co are red, and O is small and dark red. The highlighted green O represent the path which corresponds to the path of diffusion in the NEB calculations. Path (a) begins with a vacancy at site 1 and the diffusing O at site 2. Throughout the calculations, the O at site 2 moves in steps toward site 1. A similar argument follows for path (b).*

While dielectric and optical measurements can help characterize the material, the energy barrier of diffusion of O vacancies is directly related to the operation of RRAM. NEB calculations are performed for $Ni_{0.75}Fe_{0.25}O_{0.75}$ and $Ni_{0.75}Co_{0.25}O_{0.75}$ and compared to the results for intrinsic $NiO_{0.75}$ in Section 3.1. Two paths of O diffusion are evaluated in the NEB calculations, which are indicated in Figures 33(a) and 33(b). In 33(a), the vacancy begins in octahedrally coordinated Ni field and ends at a site nearest-neighbor to two Fe (Co) and four Ni. In Figure 33(b), the octahedral coordination is equivalent at the initial and final positions. Figure 34 contains energy barrier data and the force corresponding to Equation 2.7.1 along the [110] path. Even though the Fe-doped system in Figure 34(a) has the highest energy barrier, the difference in energy from the local minimum at the 3 Å position to the maximum is less than the energy barrier for the other two materials. Along the path in (b), clearly intrinsic NiO has the lesser energy barrier. In

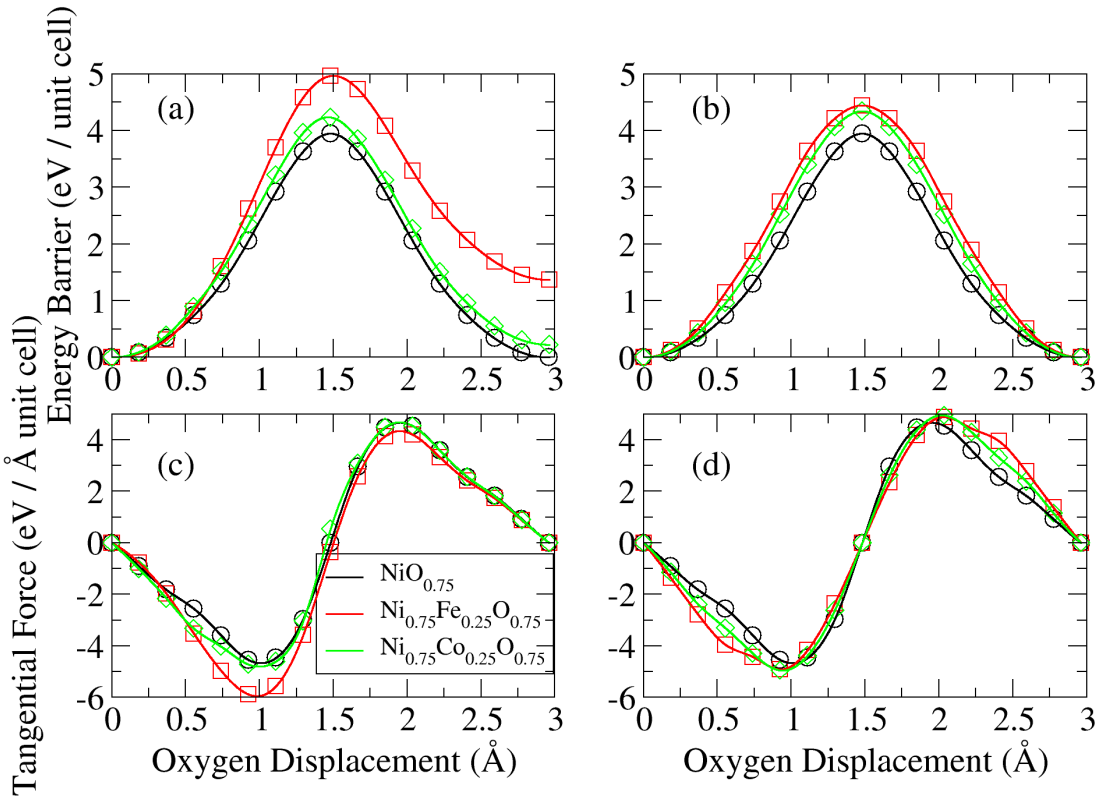

Figure 34. Nudged Elastic Band Calculations of O Diffusion in the [110] Direction of $Ni_{0.75}Fe_{0.25}O_{0.75}$. *Shown are two [110] direction paths, relative to dopant position. Data are shown by shapes, and lines are Akima spline fits. The path in (a) corresponds to the path in Figure 32(a), and the path in (b) corresponds to the path in Figure 32(b). Graphs (c) and (d) represent the forces necessary to cross the energy barriers in (a) and (b), respectively.*

(c), the average force required to cross the energy barrier is greatest in magnitude in the Fe-doped material. In (d), the forces are all comparable. It should be noted that since it is the potential energy which is proportional to the voltage, the energy barrier is perhaps the more important quantity in this figure when discussing RRAM. Both Co-doped and Fe-doped NiO should diffuse O nearly as well as intrinsic NiO; however, the undoped material requires less force to cross a lower energy barrier.

3.3 La_2NiO_4

La_2NiO_4 is an AF insulator of tetragonal space group I4/mmm, with crystal symmetry D_{4h}, where structurally equivalent unit cells are shown in Figure 35. Similar to a perovskite, the structure is known as a Ruddlesden-Popper phase, and the structural primitive cell is shown in Figure 35(a), with orthogonal lattice vectors c > a. To describe AF order, which sets in at a Néel temperature of 70 K,[118] the cell must be increased in size to include Ni sites of opposite magnetic dipole moments. Figure 35(b) displays a 2a × 2a × c AF version, where Ni nearest-neighbors are of opposite magnetic dipole moments. The magnetic primitive version of this cell is shown in Figure 35(c), where lattice vectors are √2a × √2a × c. The local spin density approximation (LSDA) within the Ceperly-Alder formulation[80] is used throughout the study of La_2NiO_4, as well as the three materials in the next three sections, including an effective Hubbard potential U-J (LSDA + U), within the Dudarev approximation.[87]

Contrary to NiO, there is not enough theoretical work using an effective Hubbard potential U-J in the literature for La_2NiO_4, so the values were found here empirically. Effective U – J values were varied from 0 – 8 eV, with steps of 0.5 eV, and Murnaghan fits were performed for each step. The Γ-centered k point mesh used in these calculations was 4 × 4 × 2. Again, cutoff energy is 320 eV. The optimized lattice constants were found at each step from Equation 3.1.2, using the cell shown in Figure 35(b), where tilt of NiO_6 octahedra was neglected. For each step, once lattice parameters were optimized, magnetic coupling constants (MCCs) were calculated with the following formula

$$\Delta E = J s^2 Z \qquad (3.3.1)$$

from Reference [119], where ΔE is the difference in total ground-state energy between ferromagnetic and AF phases, s is total spin of Ni, which is 1, Z is the nearest number of magnetic ions, which is 4, and the MCC is in units of energy. Essentially, the MCC is inter-atomic exchange. Figure 36 summarizes the results for various physical properties, as the effective Hubbard potential U – J is varied. As is typical for the LDA, lattice constants slightly underestimate the experimental value in Figure 36(a) of a = 3.86 Å and c = 12.68 Å,[120] even with the inclusion of U – J. The critical physical property in this work – the MCC (Figure 36(b)) – can be seen to cross the experimental value of 30 meV[121] for two values of U – J. Since the energy band gap (Figure 36(c)) is zero at the first crossing, the second crossing is determined to be the accurate value for U – J. Yamamoto, et al. chose their U – J value to be 6.6,[122] based on the work of Anisimov, et al.[86] While they apply U – J using a different approach than Dudarev, the analysis presented here indicates this value yields a highly accurate description of the physical properties of interest and will be used for La_2NiO_4 and the Sr doped case of LSNO. For this value of U – J, the magnitude of the magnetic dipole moment of Ni calculated here is found to be precisely the experimental value of 1.68 μ_B.[123]

Once the magnetic ground-state was described with a high level of accuracy, NiO_6 octahedral tilt was introduced by ionic relaxation. At this stage, electronic excitations were calculated. The high-symmetry path in the BZ in Figure 37 was used in the band structure calculation in Figure 38(a). In the Sr doped case, in the following section, it will become clear why the xy plane of the BZ is the region of interest. Here, the structure used in the calculations is that of Figure 35(c), which is not only more computationally

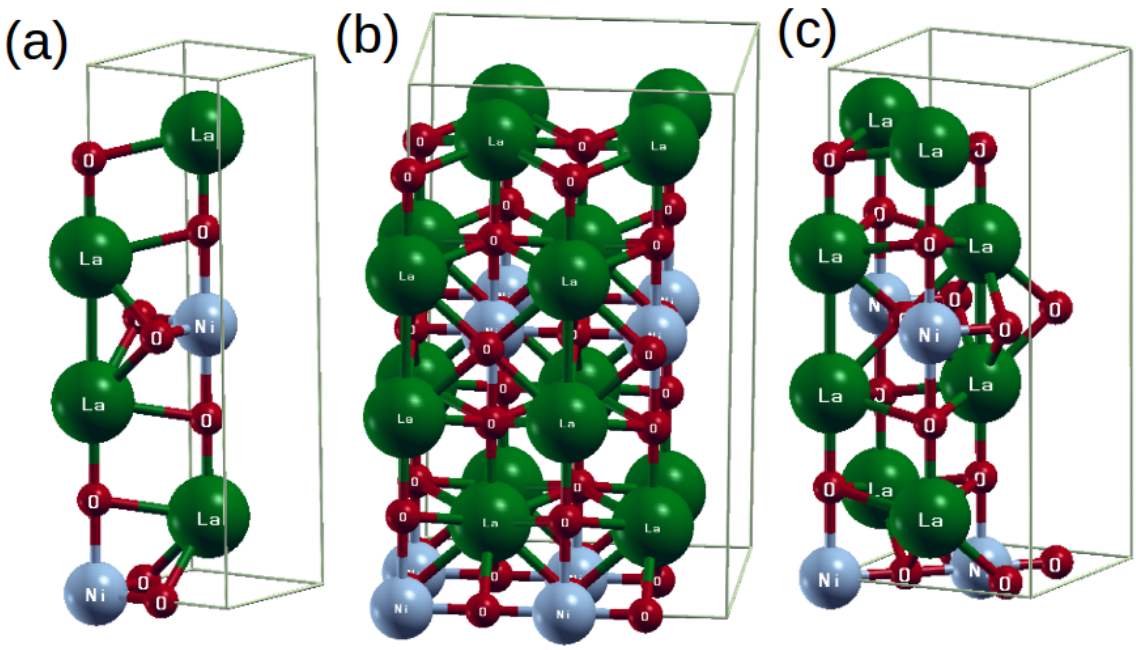

Figure 35. La_2NiO_4 Unit Cells in Three Structurally Equivalent Crystal Representations. *La is shown in green, Ni in gray, and O in red. Structure (a) is the primitive structural cell, (b) is a 2 × 2 × 1 AF version, and (c) is a √2 × √2 × 1 primitive AF cell.*

efficient than the one in Figure 35(b), but results can be more readily compared to the doped case in the following section.

The immediately apparent feature in the band structure is the extreme dispersion in the CBM along Γ-X and Γ-Y, which can be attributed to minor states of La f character in the PDOS of Figure 38(b), as is found in the calculations on La_2NiO_4 and La_2CuO_4 by Takegahara, et al.[124,125] These early LSDA calculations incorrectly described the electronic structure, however, due to valence bandwidth creating a Fermi surface which should not be present. A notable exception is the work of Guo and Temmerman,[126] who employ a Stoner parameter as the average exchange interaction. While they clearly show that La states comprise much of the CBM, they did not decompose the states to individual atomic orbital character. Though there is little to compare with, indeed the CBM is comprised of

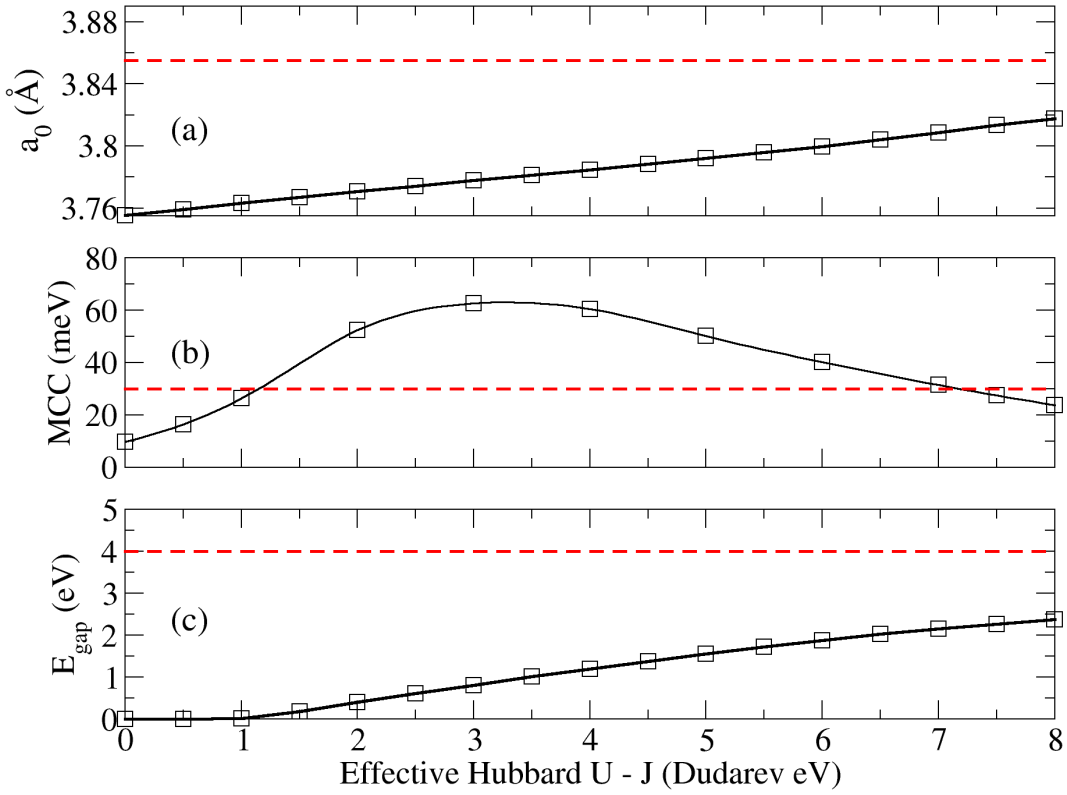

Figure 36. Effect of Variation of Effective Hubbard U - J on Physical Properties of La_2NiO_4. *Above, (a) displays the optimized lattice parameter after a Murnaghan fit, over the range of U – J, (b) displays the calculated MCCs, from Equation 3.3.1, and (c) displays the energy band gap. Experimental values (see text) are indicated by red dashed lines. Data points are connected by an Akima spline fit.*

La f. It should be noted that f levels exhibit crystal field splitting, as well, and in D_{4h} symmetry, f orbitals split to singlet a_{2u}, b_{1u}, b_{2u} and fourfold-degenerate e_u states.[107] The state corresponding to the CBM at Γ is the singlet f orbital of b_{1u} symmetry. Clearly, the dispersion of the CBM indicates a light fermion at Γ. Dispersion is evident in the VBM, as well, where the energy bands are comprised of Ni d and O p states. The elongated Ni-O bonds in the z direction create a tetragonal crystal field, which causes further splitting of d levels (Section 2.6) than in the octahedrally coordinated cases of $Ni_{1-x}Fe_xO_y$. Thus, e_g Ni d splits into nondegenerate a_{1g} and b_{1g} levels, which are frequently referred to by their

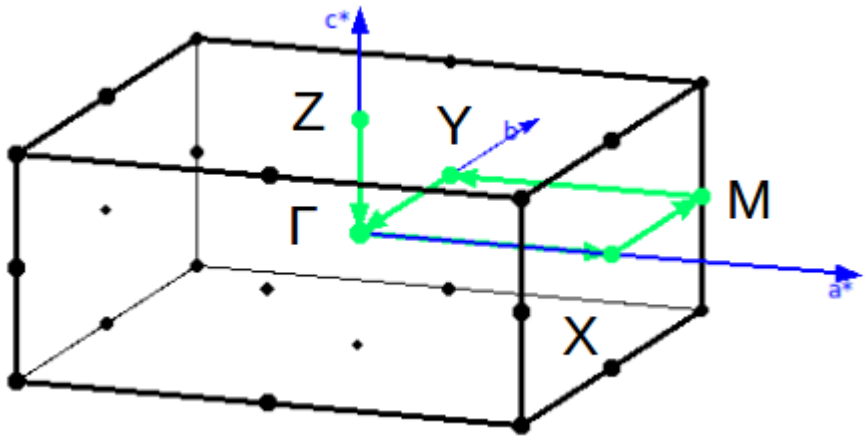

Figure 37. Brillouin Zone of La_2NiO_4. *The path used in the band structure calculation is highlighted in green, where arrows indicate the direction of the path. High symmetry points along the path are labeled in the order Z, Γ, X, M, Y, and Γ. Reciprocal lattice vectors are in blue.*

basis functions z^2 and $x^2 - y^2$, respectively.

Furthermore, the electric-dipole transition operator symmetry is split (in the same way O p is split) in the D_{4h} field to a_{2u} and e_u, where a_{2u} applies to light polarized in the z direction, and e_u applies to light polarized in the xy plane.[91] To determine the nature of the first optical transition, again, this problem is approached within ligand field theory and group theory. First, the nature of the hybridization between the b_{1g} Ni d level and that of e_u O p level needs to be determined. The hybridization is found to be of b_{1g} symmetry by Miessler and Tarr[127] by familiar group theory logic. Incidentally, an optical transition from light polarized along the c axis (z) from the a_{1g} state (Ni z^2 hybridized with O p_z) to neither b_{1u} nor e_u La f is possible from Equation 2.6.1. Such a transition is unfavorable from the small oscillator strength, as well. Due to this fact, along with the indirect band gap, the first major peaks in ε_2 are seen well above the CBM in Figure 38(c). A slight a_{2u} state of Ni p_z hybridized with O p_z is present at the VBM (not shown), such that a

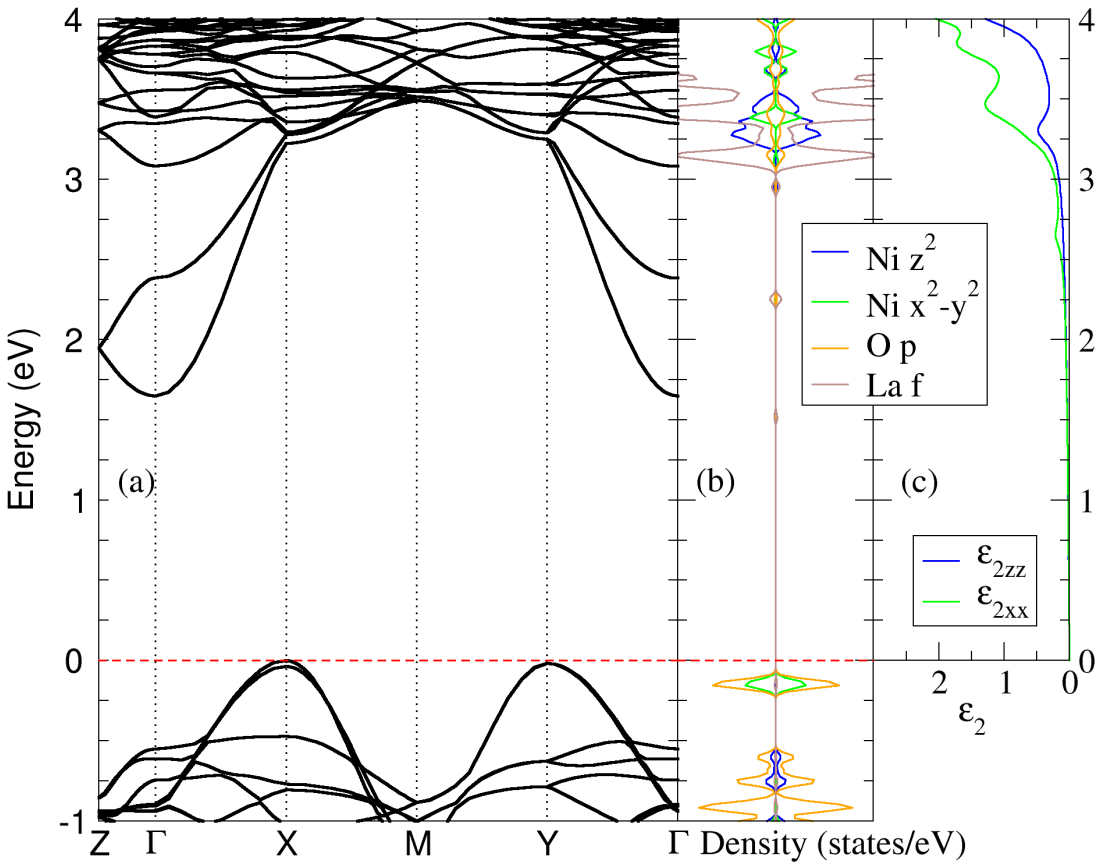

Figure 38. Electronic and Optical Properties of La_2NiO_4. *Electronic structure calculations are shown, where (a) is the band structure, (b) is the PDOS, and (c) is the imaginary component of the dielectric function.*

transition to the a_{1g} state at approximately 3.2 eV is certainly possible with light polarized in the z direction. This compares favorably with the experimentally found optical gap.[128] However, with light polarized in the xy plane, the VBM state of b_{1g} symmetry (Ni $x^2 - y^2$ hybridized with O p_x and O p_y) has no available state with which to transition optically. In this case – within the Ni-O plane of La_2NiO_4 – contrary to the case of NiO, the xy plane-polarized optical transitions in La_2NiO_4 can be explained only by site-hopping of carrier from one Ni site to another of opposite spin configuration.

3.4 $La_{5/3}Sr_{1/3}NiO_4$ (LSNO)

The tetragonal undoped primitive cell was translated to an orthorhombic supercell, with CDW and SDW commensurability in mind. A schematic which illustrates the commensurability in the Ni-O bonding plane is shown in Figure 39 (adapted from Figure 2). The unit cell was increased to a supercell of dimensions $3\sqrt{2}a \times \sqrt{2}a \times c$ for x = 1/3 LSNO, such that each of the two Ni-O planes has two stripe-centered Ni and four non-stripe-centered Ni, in agreement with Yamamoto, et al.[122] The $\sqrt{2}$ is introduced to describe CDW periodicity, since stripes in LSNO are oriented at 45 degrees to Ni-O bonds in the Ni-O planes. CDW periodicity is then $3\sqrt{2}a/2$, while it is $3\sqrt{2}a$ for SDW. It should be noted that this supercell should be considered an approximation. Zimmerman, et al. showed experimentally that stripes are rotated 90 degrees in adjacent planes in $La_{1.48}Nd_{0.4}Sr_{0.12}CuO_4$.[129] To consider the rotation here, a larger unit cell for LSNO should have dimensions $3\sqrt{2}a \times 3\sqrt{2}a \times sc$, where the integer $s > 1$ would allow simulation of staggering, or periodic shifting, of stripes every other layer in the z direction.[59] The unit cell approximation here is necessary, due to the sheer number of atoms in the calculation – 84, rather than $252 \times s$.

To maintain commensurability, the size of the cell depends critically on Sr concentration, since the sites at which La is substituted by Sr are found to affect CDW and SDW ordering drastically. This agrees with the results of Lloyd, et al., which indicate pinning of CDW to impurity location.[130] Thus, care was taken in choosing the initial magnetization on each Ni site and the position of the Sr atoms in each cell before minimizing the total energy in the ground state. Only certain configurations of Sr dopants

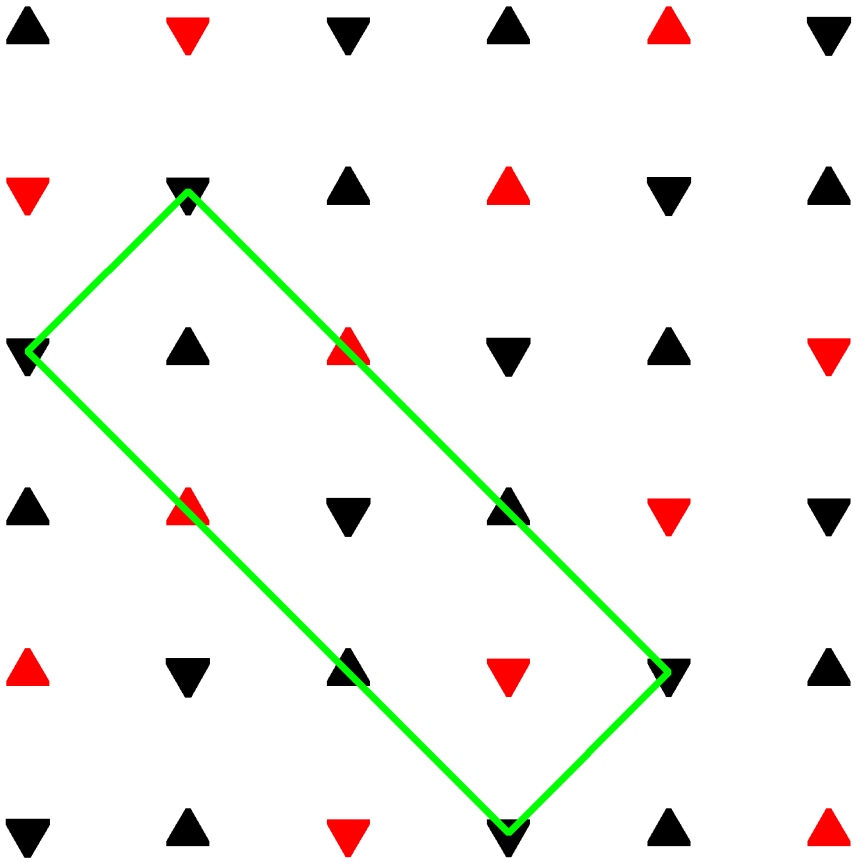

Figure 39. Commensurate LSNO Magnetic Unit Cell in 2D Ni-O plane. *Triangles indicate Ni lattice sites in the Ni-O plane, where triangles facing up indicate a positive magnetic dipole moment, and triangles pointing down indicate a negative magnetic dipole moment. Red triangles indicate partially magnetically frustrated sites where the CDW is densest. The green outline indicates the atomic sampling of the unit cell.*

were found to produce CDW and SDW in the Cu-O or Ni-O planes. The hole density congregates on the Cu or Ni nearest to the Sr, depending on spin, indicating that CDW and SDW are intimately related and dependent upon Sr position. The Sr positions are ordered with the same lattice periodicity as the CDW. The original lattice symmetry is spontaneously broken. There have been several cases of experimentally observed oxygen interstitial lattice ordering in $La_2NiO_{4.125}$.[131–134] Moreover, Lee, et al. observed interstitial oxygen order every fourth La_2O_2 layer in the HTSC $La_2CuO_{4.11}$.[135] Contrary to the case of

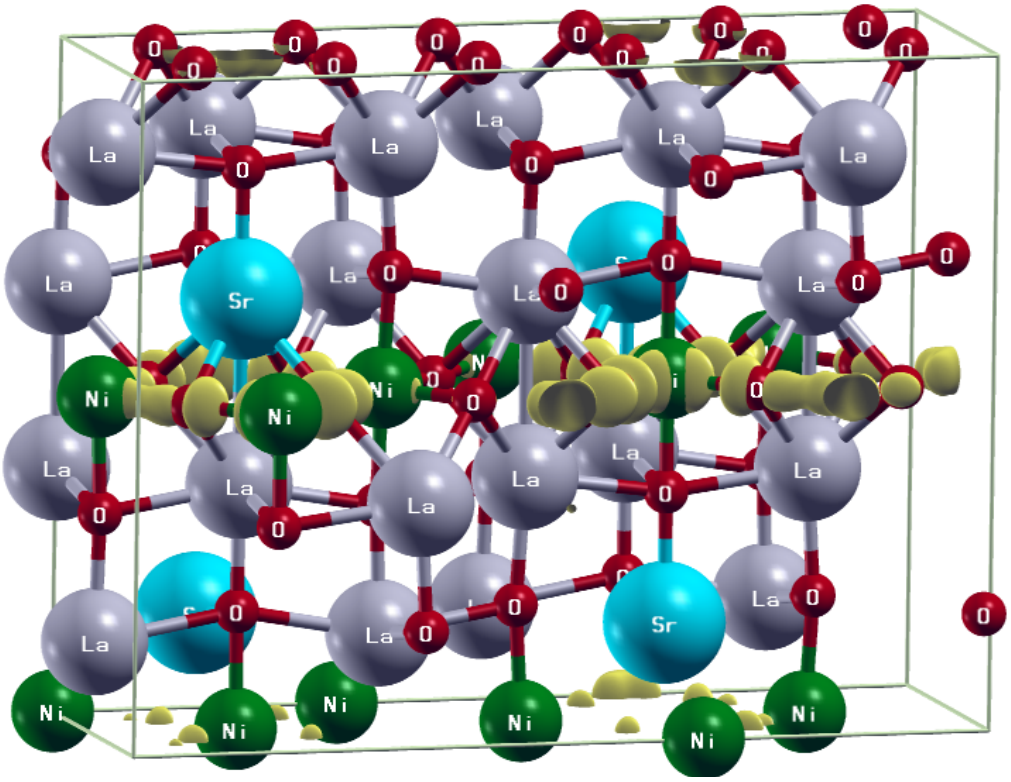

Figure 40. 3D CDW in LSNO. *La is gray, Sr is blue, Ni is green, and O is red. The CDW of the CBM is shown in yellow.*

oxygen interstitials, several experimental reports show Sr dopants are disordered in LSNO, which prevents long-range stripe order.[73,134,136,137] With CDW localization being dependent upon dopant position in the lattice, Sr disorder will result in a smectic phase at temperatures approaching 0 K, and may be nematic at finite temperatures, as found recently in experiment.[138] A smectic charge distribution refers to anisotropy within the 2D Ni-O plane, whereas a nematic system has anisotropic charge throughout the bulk. The magnetic unit cells, which are twice the lateral periodicity of the CDW, are commensurate with the SDW at this concentration of Sr. The Ni-O planes are separated by insulating LaO_2 layers, which are doped periodically with Sr. Each Sr provides one hole to one Ni in the nearest plane.

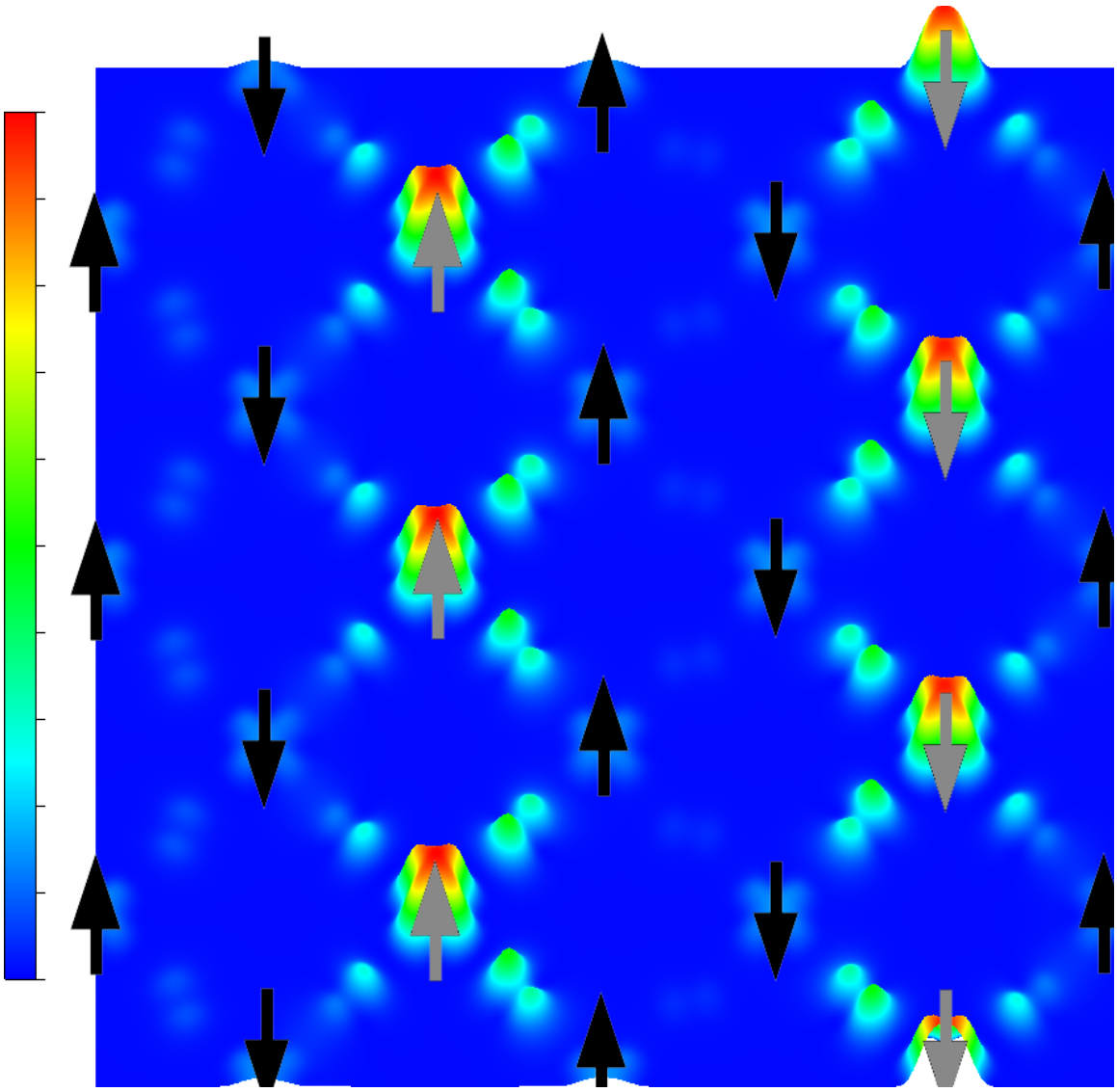

Figure 41. 2D CDW in LSNO. *The scale on the left indicates density, where red is densest. Arrows were added for schematic effect, where up arrows indicate positive magnetic dipole moment, and down arrows indicate negative magnetic dipole moment. Black arrows indicate Ni sites with no magnetic frustration, and gray arrows indicate partially magnetically frustrated Ni sites.*

Figure 40 displays the CDW clearly confined to the Ni-O plane, calculated from the square of the modulus of the wavefunction of the first excited state:

$$n_{CBM}(\boldsymbol{r})=|\varphi_{CBM}|^2. \qquad (3.4.1)$$

Taking a slice through the plane, the periodicity of the CDW can be seen more clearly in

Figure 41. The charge and spin distributions in Figure 41 are repeated along the vertical axis in a Bloch-like fashion (3x) to better illustrate the resulting density waves. Peaks correspond to holes donated by nearest-neighbor Sr which is out of the plane. Partially magnetically frustrated sites have a gray arrow, where the magnetically frustrated sites coincide with greatest charge density. Since the Ni atoms form square lattices bridged by O neighbors, with a distance of a = 3.81 Å, stripes of hole charge are aligned at 45 degrees to the Ni-O bonding direction in LSNO, giving rise to CDWs separated by two Ni of opposite spin. This finding is in complete agreement with neutron scattering data.[139]

At Ni sites nearest to Sr, where the CDW has the greatest density in LSNO, the magnetization is frustrated by ~0.7 μ_B. A complex spin pattern is visible far away from the linear antiferromagnetic ordering along the stripes. In each case, CDW nodes are found to be centered on one Ni ion with additional localization on neighboring O ions in the 2D plane (Figure 41), indicating coupling between Sr position, CDW, and SDW. In LSNO, Sr and CDW periodicities are both $3\sqrt{2}a / 2$, while SDW periodicity is $3\sqrt{2}a$. This result suggests that large primitive cell sizes should be considered when determining wave vectors in experimental characterization of similar materials exhibiting stripes. The SDW corresponds to magnetizations on Ni sites normal to Ni-O bonding plane of -1.62, 1.62, 0.92, -1.63, 1.63, -0.92 μ_B, where frustrated Ni sites with stripe localization have local magnetic moments of 0.92 μ_B. Commensurability is satisfied, and the total magnetic moment of the unit cell is zero.

Which La sites are substituted by Sr affects results significantly, especially the commensurability of CDW and SDW. The concentration x = 1/3 leads to high

commensurability between the density waves and the underlying atomic lattice, for periodic Sr. Alternative Sr concentrations and positions in the lattice modify charge density and spin orientation, resulting in incommensurate CDWs and SDWs in the chosen unit cells, along with a net magnetic moment which is to be avoided. It should be noted that the charge density of the first excited state in the (001) plane, at z = 1/2, slightly “bleeds” into the z = 0 layer in Figure 40. This indicates that some electronic correlation between layers is present, meaning the orthorhombic supercell approximation could be improved by the exact $3\sqrt{2}a \times 3\sqrt{2}a \times sc$ representation mentioned above. However, the CDW in the z = 0 layer is just as commensurate when plotted (not shown), so in the collinear spin limit, the orthorhombic cell is an excellent approximation which is used throughout the rest of the study; however, it should be noted that a calculation with noncollinear spins gave rise to more pronounced interlayer coupling, in an un-relaxed test calculation. Spin-dependent charge density of the spin-up and spin-down degenerate bands have similar magnitudes at each stripe location in the plane.

Electronic structure was calculated for the obtained CDW and SDW ground states of x = 1/3 LSNO. First, however, a comparison between the $x^2 – y^2$ orbital of Ni in various environments is warranted. In Figure 42(a), both spin channels of the orbital are shown for one Ni in NiO. It is clear that the spin-up channel (red) is fully occupied, and the spin-down channel (black) is fully unoccupied, as expected. In Figure 42(b), the spin-down channel (black) in La_2NiO_4 is fully occupied, and while the spin-up channel appears fully occupied, a state is present at approximately -1.3 eV. Having a state with the possibility of being both occupied and unoccupied is called resonance, and this

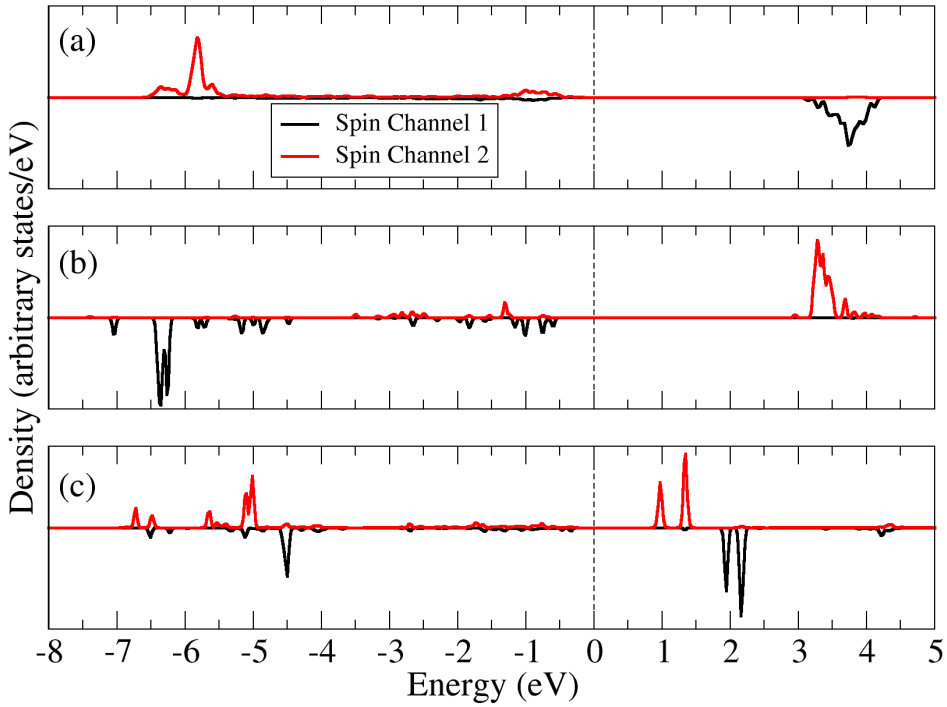

Figure 42. Comparison of DOS of the $x^2 - y^2$ Orbital of Ni in Different Environments. *Only one Ni is considered in each case. Spin-up is red, and spin-down is black. The top figure (a) displays the $x^2 - y^2$ orbital of Ni in NiO, (b) is in La_2NiO_4, and (c) is in LSNO. The black dashed line indicates the Fermi energy, taken to be zero.*

phenomenon is well-known in benzene. Anderson predicted resonance in La_2CuO_4 in 1987 within his Resonating Valence Bond (RVB) theory of cuprate superconductivity.[140] Isostructural La_2NiO_4 has remarkable similarities, even though the d orbital filling is quite different in Ni than Cu. Upon doping with Sr, the $x^2 - y^2$ orbital of a stripe-centered Ni in LSNO (Figure 42(c)) is quite clearly resonant in both spin channels.

With that in mind, the band structure in Figure 43(a) and PDOS (b-d) of LSNO clearly show an insulating ground state. A fundamental direct gap of 1 eV is found at the Y point of the Brillouin zone (BZ). In Figure 43(a), the degeneracy of hole bands is lifted, with respect to the plane in which the hole is localized, however degeneracy remains

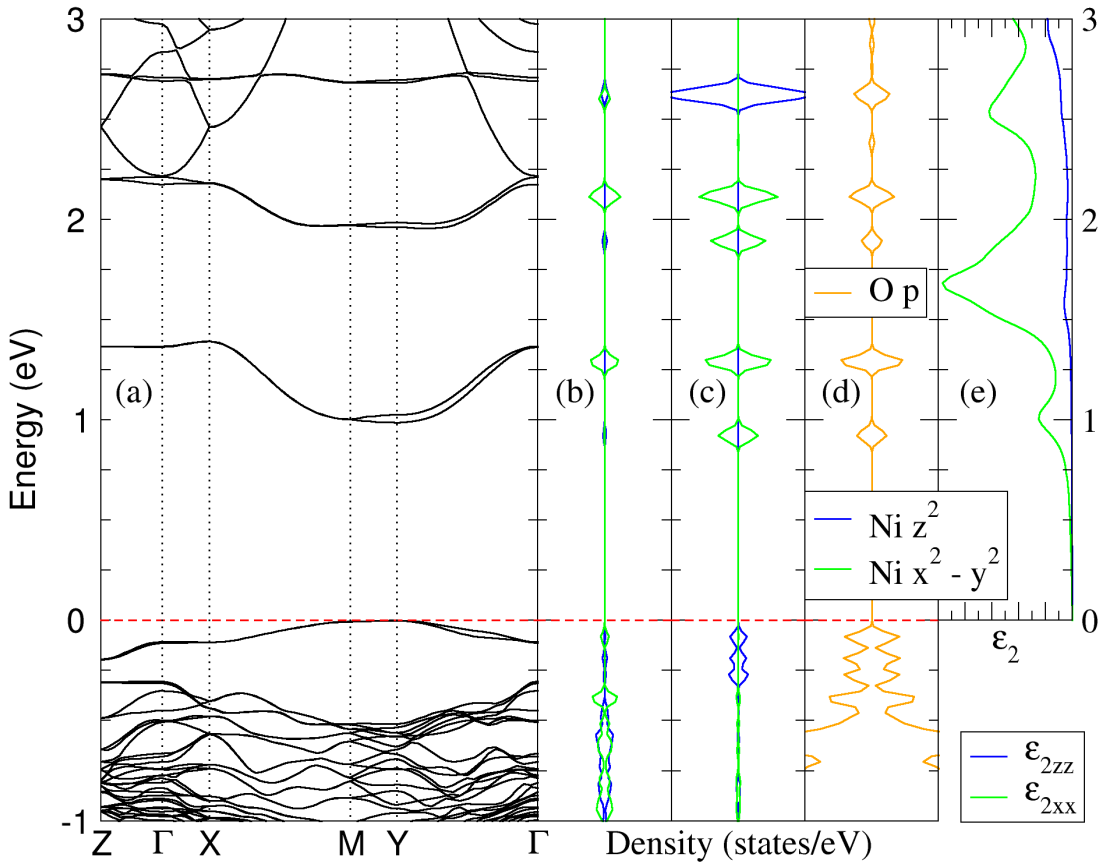

Figure 43. Electronic structure for both spin channels and optical transitions in LSNO. *(a) Band structure, (b) PDOS for non-stripe-centered Ni, (c) PDOS for stripe-centered Ni, (d) PDOS for O p (e) and imaginary parts of frequency-dependent dielectric function. Fermi energy taken as zero is shown by red dashed line.*

throughout most of the BZ. The four bands of the conduction band minimum (CBM) are degenerate throughout most of the BZ, but degeneracy is lifted along the high symmetry lines M to Y and Γ to Y. The four bands correspond to two different nodes of the CDW in each of the two Ni-O planes in the noncollinear calculation (not shown, because the spin degeneracy makes the band dispersion in the collinear calculation identical). It is the planar degeneracy that is lifted – not that of spin. To characterize the bands, figures 43(b), 43(c), and 43(d) correspond to PDOS calculations projected onto non-stripe-centered Ni, stripe-centered Ni, and O, respectively. The results widely agree with those of Yamamoto,

et al.;[122] however, here, a much larger band gap along with more states above the Fermi energy are observed. Technically speaking, more states are observed due to the points used to calculate the PDOS, along with a small broadening parameter used for Gaussian smearing. In the electronic structure, a CBM state exists for each change in energy related to high symmetry points in the BZ. These states are mostly localized to the stripe-centered Ni sites, along with some contributions from neighboring O (Figures 43(b) and (c)). Each of these two states gives rise to an optical transition for in-plane light polarization, resulting in a peak in Figure 43(e). Although the LSDA + U approach cannot provide accurate conduction band eigenvalues relative to the VBM, the character and symmetry of the bands are well described, so one can make qualitative spectral rather than quantitative energetic conclusions. The imaginary parts of the frequency-dependent dielectric function characterize the optical absorption parallel to the Ni-O plane (ε_{xx}) and parallel to the c-axis (ε_{zz}). Two transitions, one at Y, for light polarized parallel to stripe direction in the Ni-O plane, from O p_y to Ni $x^2 - y^2$, and a higher transition at X, perpendicular to stripe direction yet in the Ni-O plane, from O p_x to Ni $x^2 - y^2$. Both fulfill the angular momentum selection rule. Transitions are forbidden for polarization along the c-axis at low energy. Only those at the zone boundary are visible. Since Ni p is present in both the VBM and CBM, the same group theory argument as the intrinsic case can be made, where an a_{2u} to a_{1g} optical transition is possible with incident light polarized along the c (z) axis. For xy plane-polarized light, $x^2 - y^2$ hopping from Ni 2+ sites to Ni 3+ sites is likely.

While no pseudogap (PG) character is found in LSNO, it should be noted that the

electronic structure calculations of Figure 43 were performed within the Born-Oppenheimer approximation. Coslovich, et al. measured a PG at finite temperatures in x = ¼ LSNO, with a decrease in optical conductivity with temperature at low energy.[68] As they suggest, the PG may be attributed to contributions of the vibrating lattice in the stripe-ordered geometry. The results of Homes, et al. confirm that low energy mid-gap states are not present at low temperature.[131] Lloyd-Hughes et al. found negligible optical conductivity at low temperature for x = 1/3 yet a substantial increase for incommensurate x = 0.275.[130] Our calculations suggest that the optical conductivity (imaginary part of the dielectric function multiplied by the frequency) of the PG reduces to zero at zero temperature for commensurate samples, yet transitions are apparent at approximately 1 eV in the present calculation. For this reason, reflectivity measurements, such as those of Ido, et al.[128] at room temperature will differ from the present calculation significantly.

The real parts of the calculated dielectric functions (not shown) describe light refraction and propagation. Their $\omega \to 0$ limits determine the electronic contribution to the dielectric properties of LSNO. The dielectric results are summarized in Table 4. We find static electronic dielectric constants $\epsilon_{ij}^{\infty} = \epsilon_{ij}(0)$ of the order of magnitude known for semiconductors with similar fundamental gaps. Thereby, the components parallel to the layers are somewhat larger than the component in the c direction. Local field effects increase (decrease) the dielectric constants perpendicular (parallel) to the c axis slightly. Adding the static polarizabilities α_{ij} of the vibrating lattice, the tensor of the static dielectric constants $\epsilon_{ij}^{0} = \epsilon_{ij}^{\infty} + \alpha_{ij}$ appear. The anisotropic phonon contributions to the dielectric properties of x = 1/3 LSNO with stripe ordering are investigated in the DFPT

Table 4. Components of Static Dielectric Tensors of LSNO. *The pure electronic contributions are listed with and without local-field effects. For comparison, experimental results of Filippi, et al.[70] are also given.*

	Local Field Effects	XX	YY	ZZ
IPA Electronic Contribution	none	7.09	7.09	5.91
IPA Electronic Contribution	in DFT	6.90	6.90	5.71
DFPT ionic contribution	N/A	42.39	42.39	17.87
Total		49.29	49.29	23.58
Experiment @ T = 5 K		100		

framework.[90] The lattice polarizabilities in Table 4, the phonon contributions, are much larger than the static electronic polarization contributions. Moreover, they show a large effect due to the stripe anisotropy. In particular, large in-plane values of the order of 42 appear. CDCs of about 50 are predicted by the present ab initio calculations. The dielectric tensor is diagonal in agreement with the structural finding of the primitive orthorhombic character of the LSNO system. Our results compare qualitatively well with the low temperature measurements of Filippi, et al.[70] They attribute the value of about 100 to charge ordering in the Ni-O plane, whereas the results presented here indicate that it is the phonon interaction with the CDW in the Ni-O plane that is the dominant mechanism behind the CDC in LSNO.

3.5 La_2CuO_4

Since the MCC in the intrinsic material is fundamental to the description of the SDW in the following section including Sr dopants, here, it is calculated over a range of U – J values, similar to the calculations in Section 3.3. The results can be seen in Figure 44, where the MCC plateaus at a U – J value which is approximately 5 eV. The peak MCC value of 117 meV is found at a U – J value of 5 eV, and the experimental value has

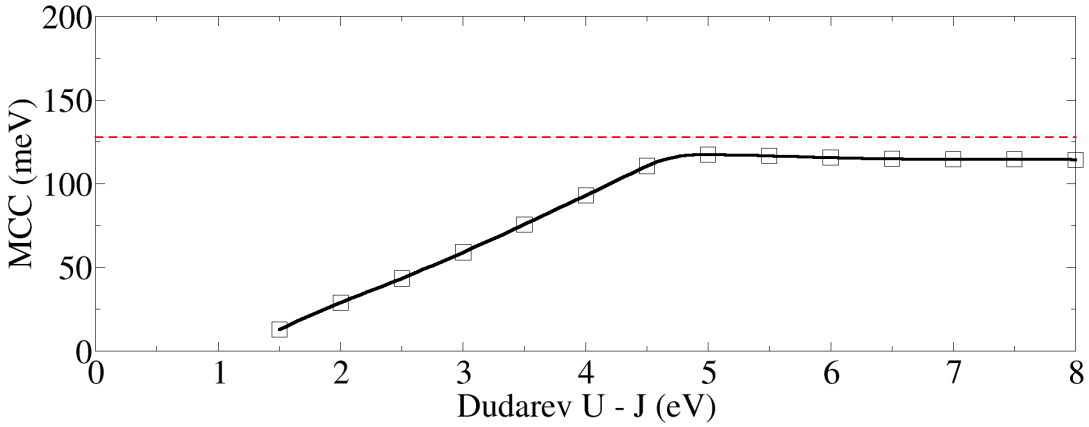

Figure 44: Magnetic Coupling Constant vs Effective Hubbard U – J in La_2CuO_4. *Calculated data points are displayed as squares, and the Akima spline fit is shown as the connecting solid black line. The Experimental value, represented by a red dashed line, is averaged between the experimental values in References [141,142].*

been shown to range within the particularly high values of 128-135 meV.[141,142] Thus, 5 eV is chosen as the effective Hubbard U – J value for all calculations in this section and the next. The corresponding magnetic-dipole moment of Cu is calculated here to be 0.53 μ_B, whereas the experimental value has been measured to be 0.4 μ_B by Vaknin, et al.[143] The U – J value which corresponds to the experimental magnetic-dipole moment is 2 eV, in which case the band gap is closed and the MCC is only 29 meV. The MCC should be as close to experiment as possible, and the energy band gap should be open, in order to describe SDW in the doped case effectively, since the SDW depends directly on Cu nearest to each other in the Cu-O plane.

La_2CuO_4 is isostructural to La_2NiO_4, described by the tetragonal I4/mmm unit cell. The lattice constants (for U – J = 5 eV) from a Murnaghan fit (Equation 3.1.1) are a = b = 3.75 Å and c = 12.95 Å. Upon full ionic relaxation resulting in forces < 10 meV/Å, tilt of the CuO_6 octahedra is evident and taken into account in all subsequent calculations. It should be noted that the path through the BZ in La_2CuO_4 differs from the case of

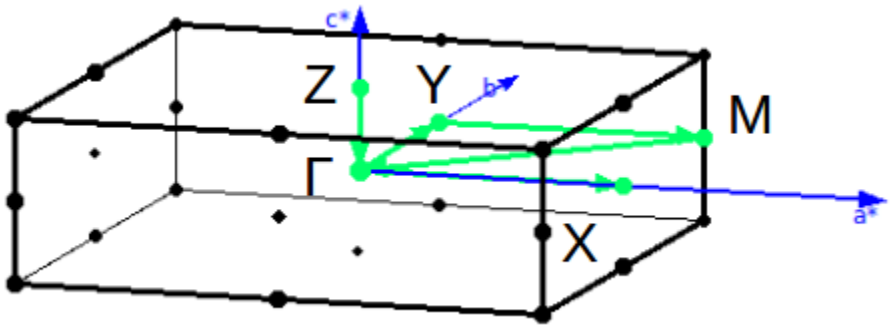

Figure 45: Brillouin Zone of La_2CuO_4. *The path used in the band structure calculation is highlighted in green, where arrows indicate the direction of the path. High symmetry points along the path are labeled in the order Z, Γ, Y, M, Γ, and X. Reciprocal lattice vectors are in blue.*

La_2NiO_4 and can be seen in Figure 45. In Section 3.3, the unit cell used for the band structure calculation is that of Figure 35(c). In the present case, the band structure is calculated from the unit cell in Figure 35(b). The reason for this will become apparent in the Sr-doped material in Section 3.6 – stripes in LSCO are aligned differently from LSNO. For a direct comparison with LSCO, here, the unit cell of Figure 35(b) and BZ of Figure 45 are the geometries of interest.

This BZ is used in the calculation of the band structure in Figure 46(a). Here, an indirect gap can be seen between the M and Γ points. Both the VBM and CBM, at the M and Γ points, respectively, are comprised of a mixture of O p and Cu $x^2 – y^2$ levels, as indicated in Figure 44(b). Contrary to La_2NiO_4, La f states are neither present near the Fermi energy nor the first optical transition, which can be seen in Figure 44(c). This contrasts with the results of Takegahara, et al., as well.[125] However, the present calculations should be considered an improvement, due to the inclusion of the effective Hubbard potential U. Here, light polarized parallel to the Cu-O plane gives rise to an optical transition from O p to Cu $x^2 – y^2$, as can be seen from the imaginary component of

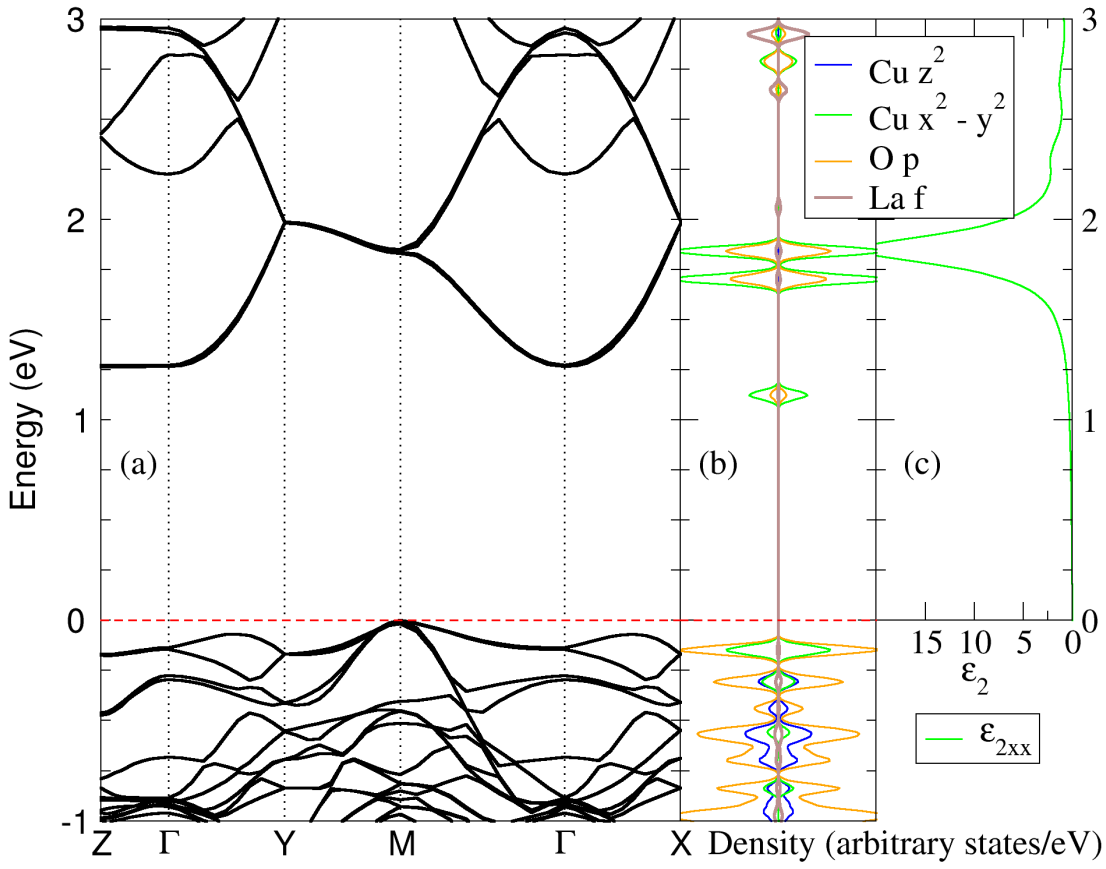

Figure 46. Electronic Structure and Optical Properties in La_2CuO_4. *Band structure is shown in (a), (b) displays PDOS, and (c) displays the imaginary part of the dielectric function. The Fermi energy is taken to be zero and is indicated by the red dashed line.*

the frequency-dependent dielectric function. This transition is allowed from both the angular momentum selection rule and Equation 2.6.1. Alternatively, the more likely scenario is hopping of the resonant $x^2 - y^2$ orbital. Incidentally, the experimental optical gap is approximately 2 eV.[128]

3.6 $La_{7/4}Sr_{1/4}CuO_4$ (LSCO)

A direct comparison between the electronic properties of x = 1/3 LSNO and x = 1/3 LSCO is not very helpful, since x = 1/3 LSCO is overdoped and slightly metallic (not

superconducting). The system considered here is x = ¼ LSCO, which is between the optimal doping concentration of x = 0.17 and the SC limit of x = 0.3.[72] While charge stripes are aligned at 45 degree angles to the Ni-O bonding direction in LSNO, they are aligned parallel to the Cu-O bonds in LSCO.[59] Therefore, the unit cell used in this case is an orthorhombic supercell version of the unit cell in Figure 35(b). Similarly to the case of LSNO, the supercell is grown in only one direction, under the assumption that interplanar correlation is minimal. However, instead of the 45 degree angle growth direction in the case of LSNO, due to the parallel bonds in LSCO, the cell is multiplied along the bonding direction, resulting in an 8a × 2a × c supercell of 224 atoms, with commensurability of CDW and SDW in mind. The resulting structure with the CDW of the first excited $x^2 - y^2$ state (PG state) can be seen in Figure 47. Care was taken in choosing the initial magnetization on each Cu site and the position of the Sr atoms in each cell before minimizing the total energy in the ground state. Only certain configurations of Sr dopants were found to produce CDW and SDW in the Cu-O planes. The hole density congregates on the Cu or Ni nearest to the Sr, depending on spin, indicating that CDW and SDW are intimately related and dependent upon Sr position. The Sr positions are ordered with the same lattice periodicity as the CDW, and the original lattice symmetry is spontaneously broken.

In order to illustrate both density wave formations in Figure 47, the formation of stripes in the Cu-O plane is shown in Figure 48 at z = 0.5c, perpendicular to the c axis. The magnetic unit cell, which is twice the lateral periodicity of the CDW, is commensurate with the SDW. The Cu-O planes are separated by insulating LaO_2 layers,

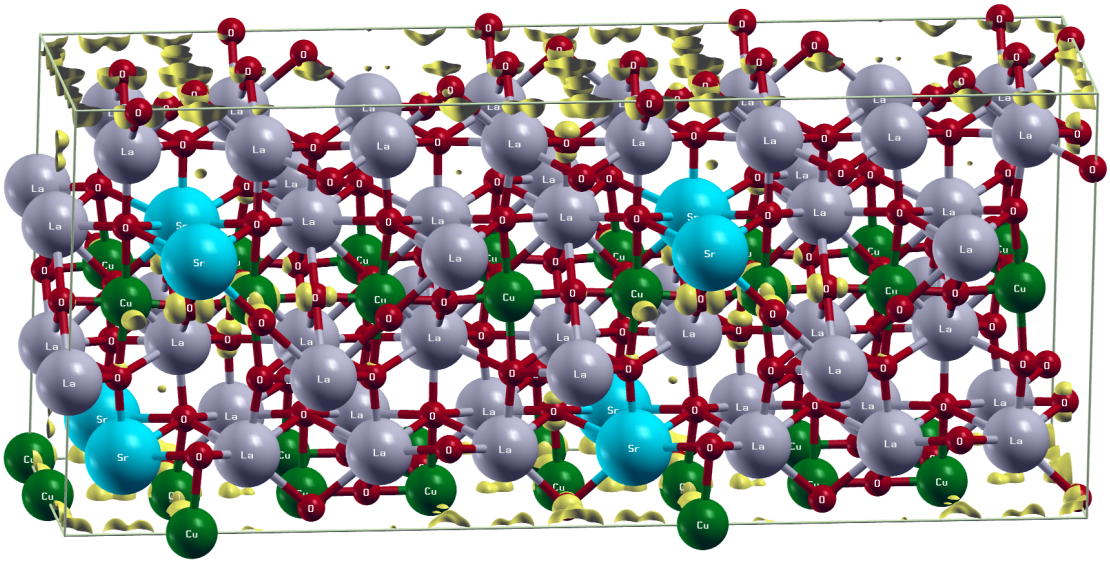

Figure 47. 3D CDW of LSCO. *La is gray, Sr is light blue, Cu is green, and O is red. The CDW is shown in yellow.*

which are doped periodically with Sr. As with LSNO, here, in LSCO, each Sr provides one hole to one Cu in the nearest plane. The charge and spin distributions in Figure 48 is repeated along the vertical axis in a Bloch-like fashion (4x) to better illustrate the resulting density waves. Peaks correspond to holes donated by nearest-neighbor Sr which is out of the plane. Magnetically frustrated sites have a gray circle, and the magnetically frustrated sites coincide with greatest charge density in the excited state considered, forming zig-zag chains. Both CDW and SDW are coupled to Sr position. Magnetic dipole-moments on Cu sites normal to the Cu-O plane are found to be 0.08, 0.41, -0.46, 0.47, -0.08, -0.41, 0.46, -0.47 μ_B, where frustrated Cu sites with stripe localization have local magnetic moments approaching zero μ_B. Commensurability is satisfied, and the total magnetic moment of the unit cell is zero. Both the Cu z^2 / O p_z hybridization and local magnetizations are described effectively in the doped system with the chosen U – J parameter.

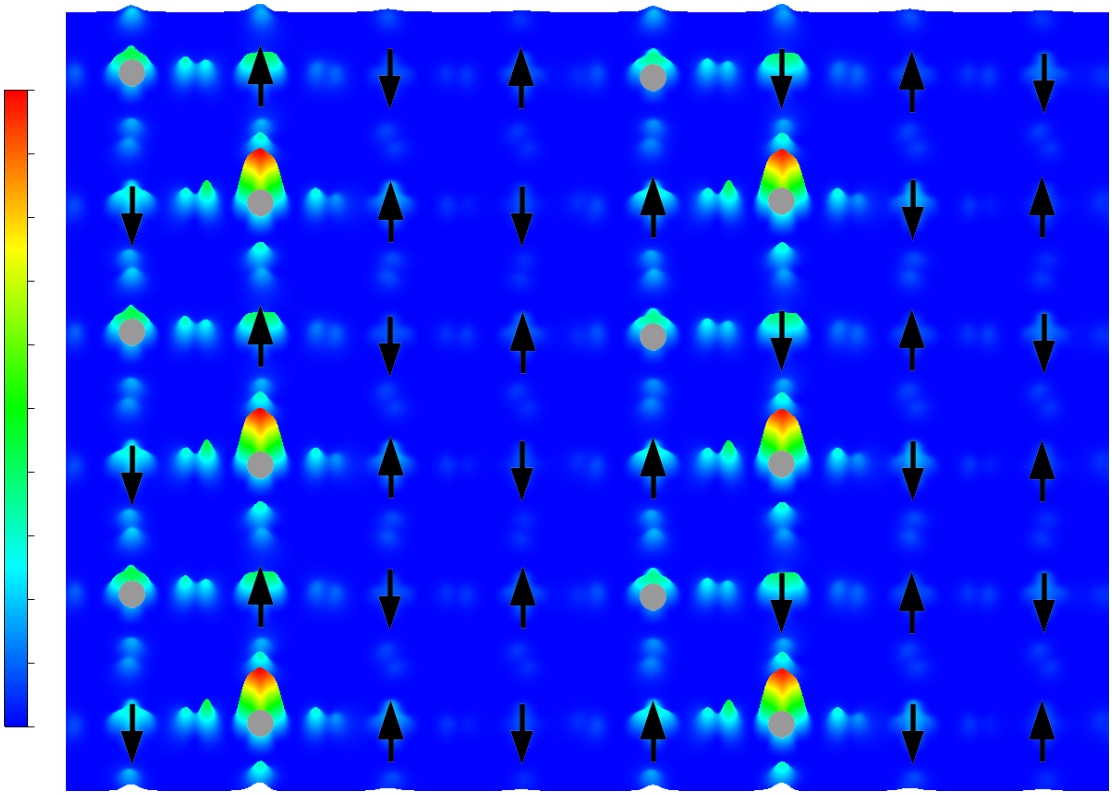

Figure 48. 2D CDW in LSCO. *The scale on the left indicates density, where red is densest. Arrows were added for schematic effect, where up arrows indicate positive magnetic dipole moment, and down arrows indicate negative magnetic dipole moment. Black arrows indicate Cu sites with no magnetic frustration, and gray circles indicate completely magnetically frustrated Cu sites.*

The other d orbital of interest – the $x^2 - y^2$ orbital – is shown in various environments in Figure 49. In Figure 49(a), this orbital is shown for one Cu (2+) in La_2CuO_4, where resonance can be seen, even in the intrinsic case, as predicted by Anderson in 1987.[140] Figure 49(b) displays the $x^2 - y^2$ orbital for a non-stripe-centered Cu (2+) in LSCO, which is remarkably similar to the intrinsic case. The key difference is due simply to the method used to calculate the DOS in each case. Since the intrinsic material is insulating, a Gaussian smearing technique is applied, with a smearing parameter of 0.03 eV, whereas in the doped case, since a Fermi surface is present, the Methfessel-Paxton technique is applied, with a smearing parameter of 0.1 eV. Figure 49(c) shows the

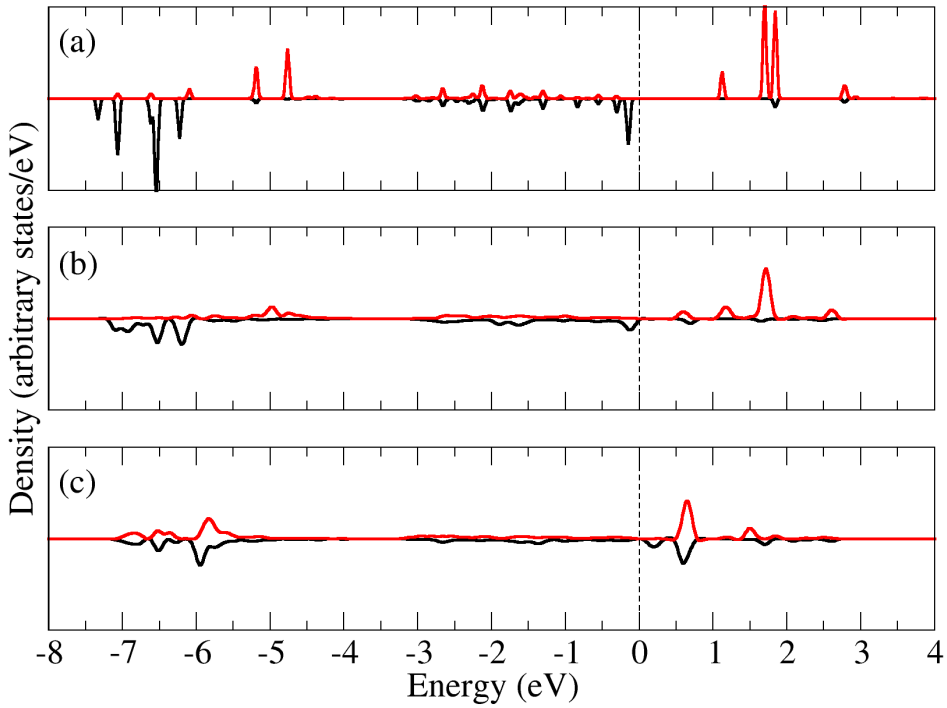

Figure 49. Comparison of DOS of the x2 – y2 Orbital of Cu in Different Environments. *Only one Cu is considered in each case. Spin-up is red, and spin-down is black. The top figure (a) displays the $x^2 - y^2$ orbital of Cu in La_2CuO_4, (b) is Cu 2+ in LSCO, and (c) is Cu 3+ in LSCO. The black dashed line indicates the Fermi energy, taken to be zero.*

same orbital but for stripe-centered Cu (3+). The local extrema at the VBM in Figures 49(a) and 49(b) is shifted to the CBM upon hole-doping, effectively emptying this state. However, due to resonance, the situation may not be so simple.

For clarity, Figure 50 displays the full relevant electronic structure of the material. The semi-metallic character can be seen clearly from the Fermi surface in the band structure (Figure 50(a)) along Γ – M, i.e., the nodal direction, from (0,0) to (π,π). The Fermi energy crosses the uppermost two valence bands, leading to hole pockets near the zone boundaries. Two series of conduction bands not present in the undoped case appear

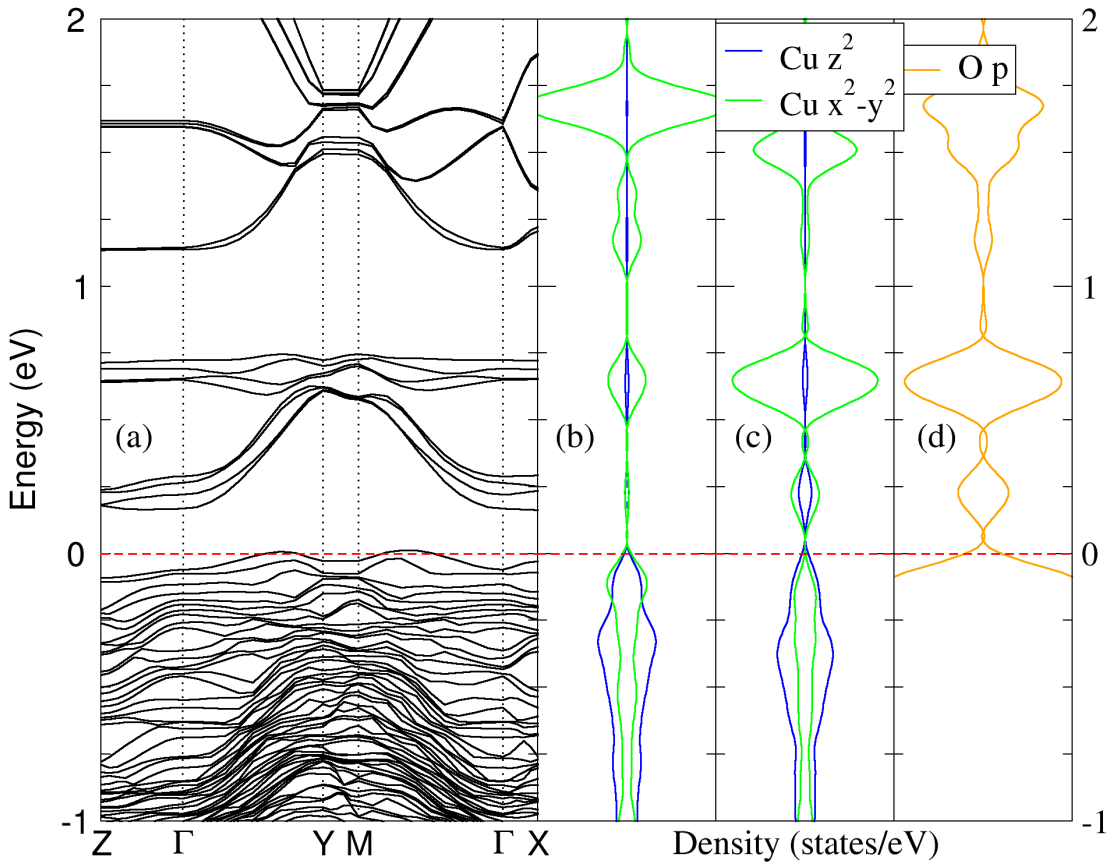

Figure 50. Electronic Structure of LSCO. *Band structure is shown in (a), DOS of non-stripe-centered (2+) Cu d orbitals are shown in (b), DOS of stripe-centered (3+) Cu d orbitals are shown in (c), and DOS of O p is shown in (d). The Fermi energy is taken to be zero and is indicated by the red dashed line.*

in the band structure between 0.2 and 0.7 eV. The lower one is related to the SC gap, whereas the one above that is the PG. The conduction states above the two gaps of the doped system form the normal gap, correspondent to the intrinsic x = 0 gap. The PDOS in Figure 50(d) shows that along with the SC gap, PG, and normal gap all have a strong O 2p character. The Cu $x^2 - y^2$ and O p bond leads to hopping optical transitions to the SC gap and the PG along Γ – X with the same character, as found in the case of LSNO. The Cu z^2 / O p_z hybridization can be seen at the Fermi surface. The $x^2 - y^2$ state ascribed to non-stripe-centered Cu forms the normal gap (Figure 50(b)), while the SC gap and PG of

$x^2 - y^2$ character are directly related to the stripe-centered Cu sites (Figure 50(c)). Our results clearly prove the proposal of Tranquada, et al., that only states aligned with the stripes are gapped.[61] This fact confirms again that the PG is directly caused by CDW, i.e., the symmetry break.

The nature of the SC gap is more complex, however, due to potentially boson-like Cooper-pair formation as a result of phonon-like interaction with the carrier pair, as is typical in BCS superconducting materials. However, Anderson's interpretation of superconductivity in the HTSC cuprates[140] has gained considerable attention over the years. His claim that the origin of SC in the HTSC cuprates is mostly electronic and magnetic, and that phonon interactions merely favor the state, is likely the correct interpretation. From Figure 50(c), it can be seen that up and down-spin states have their antisymmetric counterparts within the stripe-centered totals. It could be argued that the relaxation of the lattice around the Sr impurity and stripe formation is sufficient to overcome the repulsion between carriers of opposite spin at k and -k, thus coupling the pair within the coherence length. This coupling is indicated by degenerate states of opposite spin within the valence, of $x^2 - y^2$ character, which have resonant states above the Fermi energy corresponding to the SC gap and PG.

4. REVIEW AND FUTURE WORK

Transition metal oxides, such as NiO, La_2NiO_4, La_2CuO_4, and their doped counterparts, have a wide variety of interesting physical properties, including, but certainly not limited to resistive switching, a colossal dielectric constant, and high-temperature superconducting behavior. After an overview of theoretical techniques employed here, including DFT + U, the IPA, DFPT, and the NEB, original calculations of electronic and optical properties were interpreted in two ways. First, electronic excitation in terms of orbital hybridization was evaluated in terms of group theory. Second, the common view that $x^2 - y^2$ orbital site hopping is the dominant excitation mechanism was presented as an alternative interpretation. Since disentanglement of atomic states from hybridization within a crystal is not straightforward, calculation of the oscillator strength of electric-dipole transitions was not employed as an analysis technique. While such a numerical method can give conclusive evidence of an optical transition, the wavefunctions involved in such a calculation are linear combinations which do not necessarily give an intuitive explanation for the origin and destination of an optical transition. Thus, the interpretations presented here were chosen as a matter of preference for clarity and conceptual physical understanding. Certainly, calculations of oscillator strength of each material, on a case-by-case basis, would be an interesting comparison to the results presented here. Ground states calculated within the highly expensive quasiparticle GW approach, along with solving the Bethe-Salpeter equation to determine optical properties would certainly be ideal, but with current computational technology,

such analysis is out of reach, since it would be prohibitively expensive when dealing with unit cells of the size considered in this work. Future calculations could explore these avenues to bring further clarity.

That being said, significant conclusions were made throughout this work, using more computationally efficient methods, appropriate for the large and resource-demanding systems studied. In $Ni_{1-x}Fe_xO_y$, the first optical transition was found by group theoretical techniques to involve the p orbitals of Ni, where they hybridize with p orbitals of O in an anti-bonding σ* orbital. Within this interpretation, the first optical transition to this orbital should originate from Ni e_g hybridized with O p, which is a bonding σ orbital at the VBM. The alternative explanation is site hopping from the e_g orbital of one Ni to the e_g orbital of the next nearest Ni. This explanation is likely, due to excitons in transition metal oxides being Wannier-Mott-like with a large radius. Furthermore, it fits with the observed electronic structure when including oxygen vacancies. Future excitonic calculations can confirm.

In electronic devices, it is often the static dielectric constant which is of interest, and since iron dopants and oxygen vacancies in NiO were a large focus of this work, due to the grant support, comparisons were made for various concentrations of both. While clearly oxygen vacancies increase the dielectric constant, addition of iron surprisingly decreases it, even though the static value for FeO is about twice that of NiO. The screening from addition of iron certainly affects the diffusion of oxygen, as well, which is critical in RRAM. The NEB calculations presented here indicate that oxygen diffusion in intrinsic NiO may have a lower energy barrier than iron-doped NiO. However, further

confirmation could be obtained by calculating the diffusion coefficient and activation energy of oxygen in each case.

Dopants (Sr) were added to La_2NiO_4 and La_2CuO_4, as well, and the doped materials were directly compared theoretically via *ab initio* methods, for the first time. Two main conclusions are to be drawn from these sections. First, the colossal dielectric constant in LSNO is a direct result of the coupling of lattice vibrations with the CDW. Second, the PG state in LSCO is attributed to the CDW, from hopping within the resonant $x^2 – y^2$ orbital. Resonance of the $x^2 – y^2$ orbital, which is the first excited state, was observed in both materials.

The PG being directly related to the resonant $x^2 – y^2$ conduction band is the most important discovery made in this work, which indicates validity of Anderson's RVB theory. While the author certainly does not presume to fully explain HTSC in the cuprates, it should be noted that with the characterization of the PG presented here, it would not take a great leap in logic to extend this understanding to the similar SC gap and develop a theoretical framework for the mechanism behind HTSC in the cuprates. With a better understanding of the mechanism, materials exhibiting HTSC could be engineered with improved physical properties.

The second major contribution here is that of the CDC in LSNO being a direct result of vibronic coupling of the lattice with the CDW in the Ni-O plane. With further understanding, CDC devices become closer to commercial application. In addition to this, the densest portion of the CDW is located in the metal-oxygen plane nearest to the Sr impurity in both LSCO and LSNO, at low temperature.

APPENDIX A: OPTICAL PROPERTIES

Equations of optical properties which can be directly calculated from the frequency-dependent complex dielectric function are presented here. For more information, see Ashcroft and Mermin.[89] The refractive index can be calculated by

$$n_{ii}(\omega)=\sqrt{\frac{|\epsilon_{ii}(\omega)|+\Re\,\epsilon_{ii}(\omega)}{2}}.$$

The extinction coefficient follows as:

$$k_{ii}(\omega)=\sqrt{\frac{|\epsilon_{ii}(\omega)|-\Re\,\epsilon_{ii}(\omega)}{2}},$$

where the $\Re$ indicates the real portion, and ij represents the ij tensor component. Optical conductivity can be found from

$$\Re\,\sigma_{ii}(\omega)=\frac{\omega}{4\pi}\Im\,\epsilon_{ii}(\omega),$$

where $\Im$ represents the imaginary portion. Reflectivity can be calculated from

$$R_{ii}(\omega)=\frac{(n_{ii}-1)^2+k_{ii}^2}{(n_{ii}+1)^2+k_{ii}^2}.$$

Absorption coefficient is calculated by

$$A_{ii}(\omega)=\frac{2\,\omega\,k_{ii}(\omega)}{c},$$

where c is the speed of light. Loss function is found from

$$L_{ii}(\omega)=-\Im\left(\frac{1}{\epsilon_{ii}(\omega)}\right).$$

Finally, optical conductivity can be calculated by

$$\Re\,\sigma_{ii}(\omega)=\frac{\omega}{4\pi}\,\Im\,\epsilon_{ii}(\omega).$$

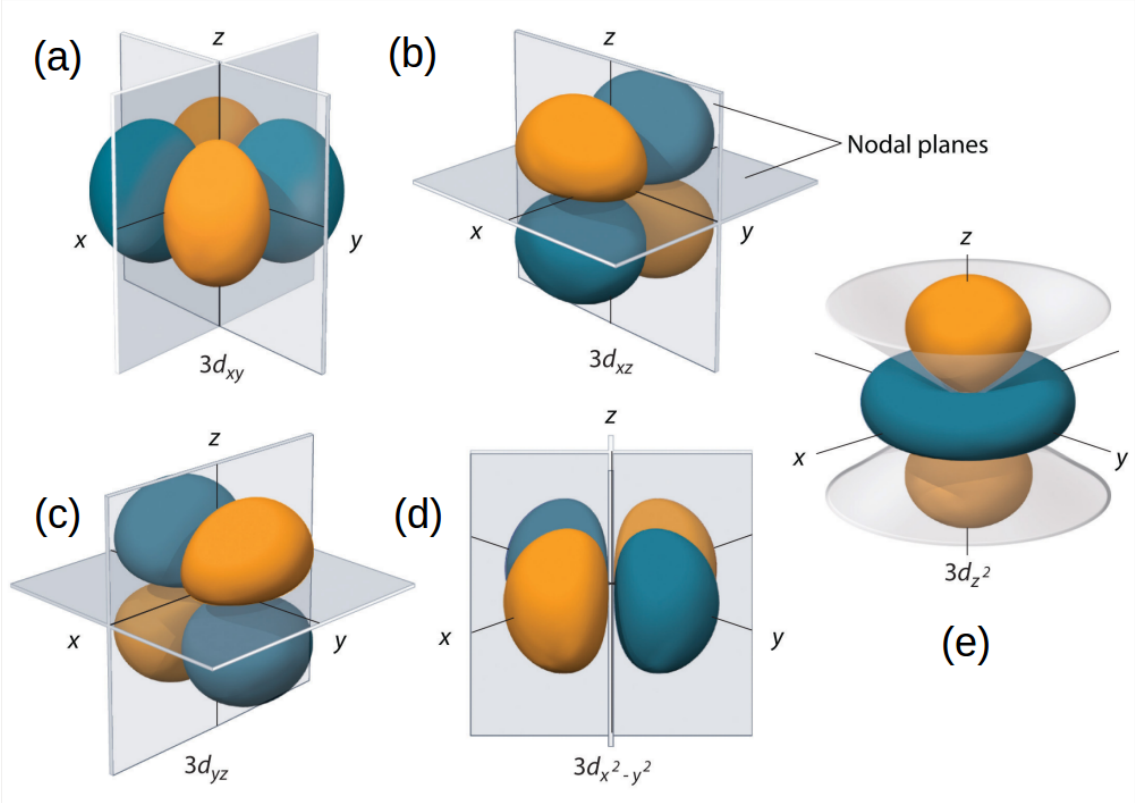

Figure 51. Schematic Images of the d Orbitals. *Schematics (a), (b), and (c) represent the t_{2g} orbitals, and (d) and (e) represent the e_g orbitals. Blue and orange orbitals represent opposite parity. Open source figure adapted from chem.libretexts.org.*

APPENDIX B: BASIS FUNCTIONS AND D ORBITALS

From the familiar images in Figure 51, the t_{2g} orbitals in O_h (octahedral) symmetry shown by (a), (b), and (c) can be taken into each other by inversion, which is a type of symmetry operation. The theorems of group theory will not be derived here. Rather, only practical application of group theory will be presented here and explained pedagogically, as is relevant to the analysis of the solid state physics in this work. In the systems considered here, with octahedral (cubic) or dihedral (tetragonal) symmetry, the t_{2g} orbitals are not along the bonding direction, so not only do they not contribute to bonding, they

exhibit limited further crystal field splitting in a dihedral field. On the contrary, the e_g orbitals in (d) and (e) are along the bonding direction. Thus, they are directly involved in bonding. They are degenerate in energy in octahedral symmetry, yet another splitting occurs in a dihedral crystal field. The orbitals in (d) are also related geometrically by π/2 rotations; however, in (e), the case is not as simple. While crystal field splitting can be observed in both t_{2g} and e_g orbitals, here, the present work is primarily concerned with the e_g orbitals in (d) and (e). Upon splitting in a dihedral field, the degeneracy is lifted, and the now non-degenerate e_g orbitals can be expressed in real finite form. As such, a symmetry operation R, which can be represented by the matrix **D**(R), operates on the basis functions corresponding to the orbitals in question.

Basis functions in what is known as carrier space are analogous to unit vectors in Cartesian space. Being an abstract concept, an example is helpful for clarity, and since it is the e_g orbitals which are the orbitals of importance in the present work, the symmetry operations on these orbitals in O_h and D_{4h} symmetries will be presented explicitly. For the e_g orbitals (d) and (e) in the group O_h, the basis functions are $\sqrt{3}(x^2 - y^2)$ and $3z^2 - r^2$, where the $\sqrt{3}$ is commonly omitted in the former, and the latter can be equally expressed as $2z^2 - x^2 - y^2$ by the Pythagorean Theorem in three dimensions. Thus, the basis functions in an octahedral crystal field can be represented as follows:

$$\boldsymbol{X}_1 = 2z^2 - x^2 - y^2;$$
$$\boldsymbol{X}_2 = \sqrt{3}(x^2 - y^2).$$

The symmetry operations which bring these basis functions into new linear combinations of each other are

$$\boldsymbol{D}\left(C_4^z\right)=\begin{pmatrix}1 & 0\\ 0 & -1\end{pmatrix},$$

and

$$\boldsymbol{D}\left(C_3^{xyz}\right)=\begin{pmatrix}-\frac{1}{2} & -\frac{\sqrt{3}}{2}\\ \frac{\sqrt{3}}{2} & -\frac{1}{2}\end{pmatrix}.$$

The former operates as a 2π/4 rotation about the z axis, and the latter operates as a 2π/3 rotation about the [111] axis. The matrices can be constructed using tables from any crystallography text, noting that

$O_h = O \otimes i$,

where i is the inversion operator

$$i=\begin{pmatrix}-1 & 0\\ 0 & -1\end{pmatrix},$$

and ⊗ represents a direct matrix product. Symmetry operations on basis functions can be described by

$$\boldsymbol{D}(R)\begin{pmatrix}\boldsymbol{X_1}\\ \boldsymbol{X_2}\end{pmatrix}=\begin{pmatrix}\boldsymbol{X'}_1\\ \boldsymbol{X'}_2\end{pmatrix}.$$

Explicitly, in O_h symmetry,

$$\begin{pmatrix}1 & 0\\ 0 & -1\end{pmatrix}\begin{pmatrix}2z^2-x^2-y^2\\ \sqrt{3}(x^2-y^2)\end{pmatrix}=\begin{pmatrix}2z^2-x^2-y^2\\ \sqrt{3}(y^2-x^2)\end{pmatrix},$$

and

$$\begin{pmatrix}-\frac{1}{2} & -\frac{\sqrt{3}}{2}\\ \frac{\sqrt{3}}{2} & -\frac{1}{2}\end{pmatrix}\begin{pmatrix}2z^2-x^2-y^2\\ \sqrt{3}(x^2-y^2)\end{pmatrix}=\begin{pmatrix}2y^2-x^2-z^2\\ \sqrt{3}(z^2-x^2)\end{pmatrix}.$$

Thus, a π/2 rotation about the z axis leaves $\mathbf{X}_1$, the orbital in Figure (e), invariant, whereas $\mathbf{X}_2$ has changed sign, effectively going from blue to orange in Figure (d). The 2π/3 rotation about the [111] axis effectively permutes (x, y, z) to (z, x, y). The Cartesian axes are still right-handed, but the orbitals in Figures (d) and (e) have rotated with the crystal, along with the gray cone in Figure (e). For more information, see Reference [93].

APPENDIX C: AUTHOR'S PUBLICATIONS AND PRESENTATIONS

Publications

S. Sohal, M. Edirisooriya, O. S. Ogedengbe, J. E. Petersen, C. H. Swartz, E. G. LeBlanc, T. H. Myers, J. V. Li, M. Holtz: *Carrier Lifetimes of Iodine-Doped CdMgTe/CdSeTe Double Heterostructures Grown by Molecular Beam Epitaxy*. Journal of Electronic Materials 06/2017;, DOI:10.1007/s11664-017-5646-y

O.S. Ogedengbe, C.H. Swartz, P.A.R.D. Jayathilaka, J.E. Petersen, S. Sohal, E.G. LeBlanc, M. Edirisooriya, K.N. Zaunbrecher, A. Wang, T.M. Barnes, T.H. Myers: *Iodine Doping of CdTe and CdMgTe for Photovoltaic Applications*. Journal of Electronic Materials 06/2017;, DOI:10.1007/s11664-017-5588-4

John E. Petersen, Fidele Twagirayezu, Luisa M. Scolfaro, Pablo D. Borges, Wilhelmus J. Geerts: *Electronic and optical properties of antiferromagnetic iron doped NiO – A first principles study*. AIP Advances 05/2017; 7(5):055711., DOI:10.1063/1.4975493

Sandeep Sohal, M Edirisooriya, O S Ogedengbe, J E Petersen, C H Swartz, E G LeBlanc, T H Myers, J V Li, M Holtz: *Effect of free-carrier concentration and optical injection on carrier lifetimes in undoped and iodine doped CdMgTe/ CdSeTe double heterostructures grown by molecular beam epitaxy*. Journal of Physics D Applied Physics 11/2016; 49(50):505104., DOI:10.1088/0022-3727/49/50/505104

C. H. Swartz, K. N. Zaunbrecher, S. Sohal, E. G. LeBlanc, M. Edirisooriya, O. S. Ogedengbe, J. E. Petersen, P. A. R. D. Jayathilaka, T. H. Myers, M. W. Holtz, T. M. Barnes: *Factors influencing photoluminescence and photocarrier lifetime in CdSeTe/CdMgTe double heterostructures*. Journal of Applied Physics 10/2016; 120(16):165305., DOI:10.1063/1.4966574

John Petersen, Fidele Twagirayezu, Pablo D. Borges, Luisa Scolfaro, Wilhelmus Geerts: *Ab initio study of oxygen vacancy effects on electronic and optical properties of NiO*. MRS Advances 05/2016; -1:1-6., DOI:10.1557/adv.2016.405

C. H. Swartz, J. E. Petersen, E. W. Welch, T. H. Myers: *The Effect of Anisotropic Valleys on Phonon Scattering and the Magnetotransport Properties of n-Type PbTe*. Journal of Electronic Materials 11/2015; 45(1)., DOI:10.1007/s11664-015-4184-8

P. D. Borges, J. E. Petersen, L. M. R. Scolfaro, H. W. Leite Alves, T. H. Myers: *Thermoelectric properties of IV–VI-based heterostructures and superlattices*. Journal of Solid State Chemistry 07/2015; 227:123., DOI:10.1016/j.jssc.2015.03.027

John E. Petersen, Luisa M. Scolfaro, Thomas H. Myers: *Elastic and mechanical properties of intrinsic and doped PbSe and PbTe studied by first-principles*. Materials Chemistry and Physics 08/2014; 146(3):472–477., DOI:10.1016/j.matchemphys.2014.03.055

Presentations

J. Petersen, F. Bechstedt, J. Furthmüller, L. Scolfaro, *Ab Initio study on structural, electronic, magnetic and dielectric properties of LSNO within Density Functional Perturbation Theory.* APS March Meeting, New Orleans, LA (2017).

J. Petersen, F. Twagirayezu, P. Borges, L. Scolfaro, W. Geerts, *Role of Oxygen Vacancies in Fe-Doped NiO from ab Initio Calculations.* Annual Conference on Magnetism and Magnetic Materials (MMM), New Orleans, LA (2016).

L. Scolfaro, A. Neto, H. Alves, J. Petersen, T. Myers, P. Borges, *Ab initio calculations of the vibrational and dielectric properties of PbSnTe alloys*, APS March Meeting, Baltimore, MD (2016).

J. Petersen, F. Twagirayezu, P. Borges, L. Scolfaro, W. Geerts, *First principles study of oxygen vacancies and iron impurities on electrical and optical properties of NiO,* APS March Meeting, Baltimore, MD (2016).

O. Ogedengbe, P. Jayathilaka, J. Petersen, S. Sohal, E. LeBlanc, M. Edirisooriya, C. Swartz, T. Myers, K. Zaunbrecher, T. Barnes, *Iodine doping studies of CdTe grown using molecular beam epitaxy,* MRS Spring Meeting and Exhibit, Phoenix, Arizona (2016).

P. Borges, J. Petersen, L. Scolfaro, H. Alves, T. Myers, *First principles study of thermoelectric properties of IV-VI semiconductor superlattices*, APS March Meeting, San Antonio, TX (2015).

REFERENCES

[1] C. A. Mack, IEEE Trans. Semicond. Manuf. **24**, 202 (2011).

[2] A.A. Chien and V. Karamcheti, Computer. **46**, 48 (2013).

[3] J. Meena, S. Sze, U. Chand, and T. Tseng, Nanoscale Res. Lett. **9**, 526 (2014).

[4] H.S.P. Wong, H.Y. Lee, S. Yu, Y.S. Chen, Y. Wu, P.S. Chen, B. Lee, F.T. Chen, and M.J. Tsai, Proc. IEEE **100**, 1951 (2012).

[5] A. Sawa, Mater. Today **11**, 28 (2008).

[6] Y. Taur, D.A. Buchanan, W. Chen, D.J. Frank, K.E. Ismail, L.O. Shih-Hsien, G.A. Sai-Halasz, R.G. Viswanathan, H.J.C. Wann, S.J. Wind, and H.S. Wong, Proc. IEEE **85**, 486 (1997).

[7] D. Kwon, K.M. Kim, J.H. Jang, J.M. Jeon, M.H. Lee, G.H. Kim, X. Li, G. Park, B. Lee, S. Han, M. Kim, and C.S. Hwang, Nat. Nanotechnol. **5**, 148 (2010).

[8] C. Cagli, F. Nardi, and D. Ielmini, IEEE Trans. Electron Devices **56**, 1712 (2009).

[9] T.G. Seong, M.R. Joung, J.W. Sun, M.K. Yang, J.K. Lee, J.W. Moon, J. Roh, and S. Nahm, Jpn. J. Appl. Phys. **51**, (2012).

[10] J.Y. Son and Y.H. Shin, Appl. Phys. Lett. **92**, 1 (2008).

[11] H. Wang, C. Zou, L. Zhou, C. Tian, and D. Fu, Microelectron. Eng. **91**, 144 (2012).

[12] J.G. Bednorz and K.A. Müller, Zeitschrift Für Phys. Rev. B **64**, 189 (1986).

[13] P.A. Lee, N. Nagaosa, and X.G. Wen, Rev. Mod. Phys. **78**, (2006).

[14] T.W. Hickmott, J. Appl. Phys. **33**, 2669 (1962).

[15] J.F. Gibbons and W.E. Beadle, Solid. State. Electron. **7**, 785 (1964).

[16] F. Argall, Solid. State. Electron. **11**, 535 (1968).

[17] A. Sawa, Mater. Today **11**, 28 (2008).

[18] D. Ielmini, F. Nardi, and C. Cagli, IEEE Trans. Electron Devices **58**, 3246 (2011).

[19] D. Lee, D.J. Seong, I. Jo, F. Xiang, R. Dong, S. Oh, and H. Hwang, Appl. Phys. Lett. **90**, 4 (2007).

[20] B.J. Choi, D.S. Jeong, S.K. Kim, C. Rohde, S. Choi, J.H. Oh, H.J. Kim, C.S. Hwang, K. Szot, R. Waser, B. Reichenberg, and S. Tiedke, J. Appl. Phys. **98**, (2005).

[21] K. Szot, W. Speier, G. Bihlmayer, and R. Waser, Nat. Mater. **5**, 312 (2006).

[22] G. Bersuker, D.C. Gilmer, D. Veksler, P. Kirsch, L. Vandelli, A. Padovani, L. Larcher, K. McKenna, A. Shluger, V. Iglesias, M. Porti, and M. Nafría, J. Appl. Phys. **110**, 456 (2011).

[23] S. Tsui, A. Baikalov, J. Cmaidalka, Y.Y. Sun, Y.Q. Wang, Y.Y. Xue, C.W. Chu, L. Chen, and A.J. Jacobson, Appl. Phys. Lett. **85**, 317 (2004).

[24] A. Baikalov, Y.Q. Wang, B. Shen, B. Lorenz, S. Tsui, Y.Y. Sun, Y.Y. Xue, and C.W. Chu, Appl. Phys. Lett. **83**, 957 (2003).

[25] X. Chen, N.J. Wu, J. Strozier, and A. Ignatiev, Appl. Phys. Lett. **87**, 1 (2005).

[26] Y.B. Nian, J. Strozier, N.J. Wu, X. Chen, and A. Ignatiev, Phys. Rev. Lett. **98**, 3 (2007).

[27] S.H. Jeon, B.H. Park, J. Lee, B. Lee, and S. Han, Appl. Phys. Lett. **89**, 1 (2006).

[28] A. Sawa, T. Fujii, M. Kawasaki, and Y. Tokura, Appl. Phys. Lett. **85**, 4073 (2004).

[29] T. Fujii, M. Kawasaki, A. Sawa, H. Akoh, Y. Kawazoe, and Y. Tokura, Appl. Phys. Lett. **86**, 0 (2005).

[30] I.H. Inoue, M.J. Rozenberg, S. Yasuda, M.J. Sánchezll, M. Yamazaki, T. Manageo, H. Akinaga, H. Takagi, H. Akoh, and Y. Tokura, 2005 Non-Volatile Mem. Technol. Symp. NVMTS05 **33510**, 131 (2005).

[31] F. Nardi, S. Larentis, S. Balatti, D.C. Gilmer, and D. Ielmini, Electron Devices, IEEE Trans. **59**, 2461 (2012).

[32] G. Ma, X. Tang, H. Zhang, Z. Zhong, J. Li, and H. Su, Microelectron. Eng. **139**, 43 (2015).

[33] K.-W. Nam and K.-B. Kim, J. Electrochem. Soc. **149**, A346 (2002).

[34] X. Xia, J. Tu, Y. Mai, R. Chen, X. Wang, C. Gu, and X. Zhao, Chem. - A Eur. J. **17**, 10898 (2011).

[35] R. Vardimon, M. Klionsky, and O. Tal, Nano Lett. **15**, 3894 (2015).

[36] R.C. Korošec and P. Bukovec, Acta Chim. Slov. **53**, 136 (2006).

[37] I. Hotovy, J. Huran, P. Siciliano, S. Capone, L. Spiess, and V. Rehacek, Sensors Actuators, B Chem. **78**, 126 (2001).

[38] J.A. Dawson, Y. Guo, and J. Robertson, Appl. Phys. Lett. **107**, 2 (2015).

[39] G.S. Park, X.S. Li, D.C. Kim, R.J. Jung, M.J. Lee, and S. Seo, Appl. Phys. Lett. **91**, 9 (2007).

[40] H.Y. Peng, Y.F. Li, W.N. Lin, Y.Z. Wang, X.Y. Gao, and T. Wu, Sci. Rep. **2**, 442 (2012).

[41] S. Park, H.S. Ahn, C.K. Lee, H. Kim, H. Jin, H.S. Lee, S. Seo, J. Yu, and S. Han, Phys. Rev. B **77**, 1 (2008).

[42] B. Magyari-Köpe, S.G. Park, H.D. Lee, and Y. Nishi, J. Mater. Sci. **47**, 7498 (2012).

[43] M. Gajdoš, K. Hummer, G. Kresse, J. Furthmüller, and F. Bechstedt, Phys. Rev. B **73**, 45112 (2006).

[44] J. Petersen, F. Twagirayezu, P.D. Borges, L. Scolfaro, and W. Geerts, MRS Adv. **1**, 2617 (2016).

[45] S. Baroni and R. Resta, Phys. Rev. B **33**, 5969 (1986).

[46] D.C. Kim, S. Seo, S.E. Ahn, D.S. Suh, M.J. Lee, B.H. Park, I.K. Yoo, I.G. Baek, H.J. Kim, E.K. Yim, J.E. Lee, S.O. Park, H.S. Kim, U.I. Chung, J.T. Moon, and B.I. Ryu, Appl. Phys. Lett. **88**, 2004 (2006).

[47] G. Henkelman, B.P. Uberuaga, H. Jónsson, and G. Henkelman, J. Chem. Phys. **113**, 9901 (2000).

[48] M.S. Compton, N.A. Simpson, E.G. LeBlanc, M.A. Robinson, and W.J. Geerts, MRS Proc. **1708**, mrss14 (2014).

[49] Y.F. Li and A. Selloni, ACS Catal. **4**, 1148 (2014).

[50] J. Wang, J. Cai, Y.H. Lin, and C.W. Nan, Appl. Phys. Lett. **87**, 1 (2005).

[51] A.P. Douvalis, L. Jankovic, and T. Bakas, J. Phys. Condens. Matter **19**, 436203 (2007).

[52] K. Noipa, S. Labuayai, E. Swatsitang, and S. Maensiri, Electron. Mater. Lett. **10**, 147 (2014).

[53] P. Mallick, C. Rath, R. Biswal, and N.C. Mishra, Indian J. Phys. **83**, 517 (2009).

[54] S. Thota, J.H. Shim, and M.S. Seehra, J. Appl. Phys. **114**, 1 (2013).

[55] V. Raghavan, J. Phase Equilibria Diffus. **31**, 369 (2010).

[56] M.A.A. Talukder, Y. Cui, M. Compton, W. Geerts, L. Scolfaro, and S. Zollner, MRS Adv. **1**, 3361 (2016).

[57] A.K. Bandyopadhyay, S.E. Rios, A. Tijerina, and C.J. Gutierrez, J. Alloys Compd. **369**, 217 (2004).

[58] Y. Wensheng, W. Weng, G. Zhang, Z. Sun, Q. Liu, Z. Pan, Y. Guo, P. Xu, S. Wei, Y. Zhang, and S. Yan, Appl. Phys. Lett. **92**, 52508 (2008).

[59] M. Hücker, M. V. Zimmermann, G.D. Gu, Z.J. Xu, J.S. Wen, G. Xu, H.J. Kang, A. Zheludev, and J.M. Tranquada, Phys. Rev. B **83**, 41 (2011).

[60] Q. Li, M. Hücker, G.D. Gu, A.M. Tsvelik, and J.M. Tranquada, Phys. Rev. Lett. **99**, 4 (2007).

[61] J.M. Tranquada, G.D. Gu, M. Hücker, Q. Jie, H.J. Kang, R. Klingeler, Q. Li, N. Tristan, J.S. Wen, G.Y. Xu, Z.J. Xu, J. Zhou, and M. V. Zimmermann, Phys. Rev. B **78**, 1 (2008).

[62] H.E. Mohottala, B.O. Wells, J.I. Budnick, W. a Hines, C. Niedermayer, L. Udby, C. Bernhard, A.R. Moodenbaugh, and F.-C. Chou, Nat. Mater. **5**, 377 (2006).

[63] E. Fradkin, S.A. Kivelson, and J.M. Tranquada, Rev. Mod. Phys. **87**, 457 (2015).

[64] S. Krohns, P. Lunkenheimer, C. Kant, A. V. Pronin, H.B. Brom, A.A. Nugroho, M. Diantoro, and A. Loidl, Appl. Phys. Lett. **94**, 1 (2009).

[65] A. Podpirka, A. Tselev, and S. Ramanathan, J. Phys. D. Appl. Phys. **45**, 305302 (2012).

[66] C. Hess, B. Buchner, M. Hucker, R. Gross, and S.W. Cheong, Phys. Rev. B **59**, 10397 (1999).

[67] C.-H. Du, M.E. Ghazi, Y. Su, I. Pape, P.D. Hatton, S.D. Brown, W.G. Stirling, M.J. Cooper, and S.-W. Cheong, Phys. Rev. Lett. **84**, 3911 (2000).

[68] G. Coslovich, B. Huber, W.-S. Lee, Y.-D. Chuang, Y. Zhu, T. Sasagawa, Z. Hussain, H. A. Bechtel, M.C. Martin, Z.-X. Shen, R.W. Schoenlein, and R. a Kaindl, Nat. Commun. **4**, 2643 (2013).

[69] S. Huefner, M.A. Hossain, A. Damascelli, and G.A. Sawatzky, Reports Prog. Phys. **71**, 62501 (2008).

[70] M. Filippi, B. Kundys, S. Agrestini, W. Prellier, H. Oyanagi, and N.L. Saini, J. Appl. Phys. **106**, 104116 (2009).

[71] H. Yoshizawa, T. Kakeshita, R. Kajimoto, T. Tanabe, T. Katsufuji, and Y. Tokura, Phys. Rev. B **61**, 4 (2000).

[72] R. Cooper, Y. Wang, B. Vignolle, O. Lipscombe, S. Hayden, Y. Tanabe, T. Adachi, Y. Koike, M. Nohara, H. Takagi, C. Proust, and N. Hussey, Science **323**, 603 (2009).

[73] C. Chen, S. Cheong, and A. Cooper, Phys. Rev. Lett. **71**, 2461 (1993).

[74] R.R. Tummala, IEEE Spectr. **43**, 44 (2006).

[75] A.E. Ostfeld, I. Deckman, A.M. Gaikwad, C.M. Lochner, and A.C. Arias, Sci. Rep. **5**, 15959 (2015).

[76] B. Van Tassell, S. Yang, C. Le, L. Huang, S. Liu, P. Chando, X. Liu, A. Byro, D.L. Gerber, E.S. Leland, S.R. Sanders, P.R. Kinget, I. Kymissis, D. Steingart, and S. O'Brien, IEEE Trans. Power Electron. **31**, 2695 (2016).

[77] P. Lunkenheimer, V. Bobnar, V. Bobnar, A. V. Pronin, A.I. Ritus, A.A. Volkov, and A. Loidl, Phys. Rev. B **66**, 521051 (2002).

[78] S. Krohns, P. Lunkenheimer, C. Kant, a. V. Pronin, H.B. Brom, a. a. Nugroho, M. Diantoro, and a. Loidl, Appl. Phys. Lett. **94**, 122903 (2009).

[79] J.E. Petersen, First Principles Study of Structural, Electronic, and Mechanical Properties of Lead Selenide and Lead Telluride, Master's Thesis, Texas State University, 2013.

[80] B. Alder and D. Ceperly, Phys. Rev. Lett. **45**, 56 (1980).

[81] J. Perdew, K. Burke, and M. Ernzerhof, Phys. Rev. Lett. **77**, 3865 (1996).

[82] J. Heyd, G.E. Scuseria, and M. Ernzerhof, J. Chem. Phys. **118**, 8207 (2003).

[83] P. Blöchl, Phys. Rev. B **50**, 17953 (1994).

[84] G. Kresse and J. Furthmiiller, Comput. Mat. Sci. **6**, 15 (1996).

[85] G. Kresse and J. Furthmüller, Phys. Rev. B. **54**, 11169 (1996).

[86] V.I. Anisimov, J. Zaanen, and O.K. Andersen, Phys. Rev. B **44**, 943 (1991).

[87] S.L. Dudarev, S.Y. Savrasov, C.J. Humphreys, and a. P. Sutton, Phys. Rev. B **57**, 1505 (1998).

[88] M. Krause and F. Bechstedt, J. Supercond. Nov. Magn. **26**, 1963 (2013).

[89] Ashcroft and Mermin, *Solid State Physics* (Brooks/Cole, 1976).

[90] S. Baroni, S. de Gironcoli, A. D. Corso, and P. Giannozzi, Rev. Mod. Phys. **73**, 52 (2000).

[91] M.S. Dresselhaus, G. Dresselhaus, and A. (Ado) Jorio, *Group Theory : Application to the Physics of Condensed Matter* (2008).

[92] C. Rödl and F. Bechstedt, Phys. Rev. B **86**, 1 (2012).

[93] R. McWeeny, *Symmetry: An Introduction To Group Theory And Its Applications (Dover Books On Physics)* (Dover Publications, Inc., Mineola, New York, 2002).

[94] Michael Tinkham, *Group Theory and Quantum Mechanics* (Dover Publications, Inc., Mineola, New York, 2003).

[95] G. Mills and H. Jonsson, Surf. Sci. **324**, 42 (1994).

[96] F. Birch, Phys. Rev. **71**, 809 (1947).

[97] A. Rohrbach, J. Hafner, and G. Kresse, Phys. Rev. B **69**, 75413 (2004).

[98] C. Rödl, F. Fuchs, J. Furthmüller, and F. Bechstedt, Phys. Rev. B **79**, 1 (2009).

[99] J. Zaanen, G.A. Sawatzky, and J.W. Allen, Phys. Rev. Lett. **55**, 418 (1985).

[100] D. Adler and J. Feinleib, Phys. Rev. B **2**, 3112 (1970).

[101] A. Fujimori, F. Minami, and S. Sugano, Phys. Rev. B **29**, 5225 (1984).

[102] A. Fujimori and F. Minami, Phys. Rev. B **30**, 957 (1984).

[103] G.A. Sawatzky and J.W. Allen, Phys. Rev. Lett. **53**, 2339 (1984).

[104] J. Zaanen and G.A. Sawatzky, J. Solid State Chem. **88**, 8 (1990).

[105] A. Ghosh, C.M. Nelson, L.S. Abdallah, and S. Zollner, J. Vac. Sci. Technol. A **33**, 061203/1 (2015).

[106] R. Gillen and J. Robertson, J. Phys. Condens. Matter **25**, 165502 (2013).

[107] F.A. Cotton, *Chemical Applications of Group Theory* (John Wiley and Sons Inc., New York, 1990).

[108] R. Zimmermann, R. Claessen, F. Reinert, T. Pillo, R. Zimmermann, P. Steiner, and N. Mannella, J. Phys. Condens. Matter **11**, 1657 (1999).

[109] S. Lany, J. Osorio-Guillén, and A. Zunger, Phys. Rev. B **75**, 1 (2007).

[110] J. Yu, K.M. Rosso, and S.M. Bruemmer, J. Phys. Chem. C **116**, 1948 (2012).

[111] H.D. Lee, B. Magyari-Köpe, and Y. Nishi, Phys. Rev. B **81**, 1 (2010).

[112] Y. Tokura and N. Nagaosa, Science **288**, 462 (2000).

[113] R.J. Powell and W.E. Spicer, Phys. Rev. B **2**, 2182 (1970).

[114] A.K. Jonscher, J. Phys. D. Appl. Phys. **32**, R57 (1999).

[115] J.E. Petersen, F. Twagirayezu, L.M. Scolfaro, P.D. Borges, and W.J. Geerts, AIP Adv. **7**, (2017).

[116] Y. Cui, Master's Thesis, Texas State University, 2016.

[117] H. Landolt and R. Börnstein, *Group III Condensed Matter*, 41D ed. (2005).

[118] G. Aeppli and D. Buttrey, Phys. Rev. Lett. **61**, 203 (1988).

[119] X. Feng and N.M. Harrison, Phys. Rev. B **70**, 2 (2004).

[120] R.J. Cava, B. Batlogg, T.T. Palstra, J.J. Krajewski, W.F. Peck, a P. Ramirez, and L.W. Rupp, Phys. Rev. B **43**, 1229 (1991).

[121] S. Itoh, K. Yamada, M. Arai, Y. Endoh, Y. Hidaka, and S. Hisoya, J. Phys. Soc. Japan **63**, 4542 (1994).

[122] S. Yamamoto, T. Fujiwara, and Y. Hatsugai, Phys. Rev. B **76**, 165114 (2007).

[123] J. Rodriguez-Carvajal, M.T. Fernandez-Diaz, and J.L. Martinez, J. Phys. Condens. Matter **3**, 3215 (1991).

[124] K. Takegahara and T. Kasuya, Solid State Commun. **70**, 641 (1989).

[125] K. Takegahara, H. Harima, and A. Yanase, Jpn. J. Appl. Phys. **26**, (1987).

[126] G.Y. Guo and W.M. Temmerman, Phys. Rev. B **40**, 285 (1989).

[127] G. Miessler and D. Tarr, *Inorganic Chemistry*, 2nd ed. (Prentice-Hall, Inc., New Jersey, 1998).

[128] T. Ido, K. Magoshi, H. Eisaki, and S. Uchida, Phys. Rev. B **44**, 12094 (1991).

[129] M. V. Zimmermann and E. Al., Europhys. Lett. **41**, 629 (1998).

[130] J. Lloyd-Hughes, D. Prabhakaran, A.T. Boothroyd, and M.B. Johnston, Phys. Rev. **77**, 2 (2008).

[131] C.C. Homes, J.M. Tranquada, Q. Li, A.R. Moodenbaugh, and D.J. Buttrey, Phys. Rev. B **67**, 184516 (2003).

[132] J.M. Tranquada, D.J. Buttrey, V. Sachan, and J.E. Lorenzo, Phys. Rev. Lett. **73**, 1003 (1994).

[133] P. Wochner, J.M. Tranquada, D.J. Buttrey, and V. Sachan, Phys. Rev. B **57**, 1066 (1998).

[134] J. Tranquada, D. Buttrey, and V. Sachan, Phys. Rev. B **54**, 318 (1996).

[135] Y.S. Lee, R.J. Birgeneau, M.A. Kastner, Y. Endoh, S. Wakimoto, K. Yamada, R.W. Erwin, S.-H. Lee, and G. Shirane, Phys. Rev. B **60**, 3643 (1999).

[136] V. Sachan, D.J. Buttrey, J.M. Tranquada, J.E. Lorenzo, and G. Shirane, Phys. Rev. B **51**, 12742 (1995).

[137] S.-H. Lee and S.-W. Cheong, Phys. Rev. Lett. **79**, 2514 (1997).

[138] R. Zhong, B.L. Winn, G. Gu, D. Reznik, and J.M. Tranquada, Phys. Rev. Lett. **118**, 177601 (2017).

[139] S. Anissimova, D. Parshall, G.D. Gu, K. Marty, M.D. Lumsden, S. Chi, J.A. Fernandez-Baca, D.L. Abernathy, D. Lamago, J.M. Tranquada, and D. Reznik, Nat. Commun. **5**, 3467 (2014).

[140] P.W. Anderson, Science **235**, 1196 (1987).

[141] P.E. Sulewski, P.A. Fleury, K.B. Lyons, S.W. Cheong, and Z. Fisk, Phys. Rev. B **41**, 225 (1990).

[142] B. Keimer, N. Belk, R.J. Birgeneau, A. Cassanho, C.Y. Chen, M. Greven, M.A. Kastner, A. Aharony, Y. Endoh, R.W. Erwin, and G. Shirane, Phys. Rev. B **46**, 14034 (1992).

[143] D. Vaknin, S.K. Sinha, D.E. Moncton, D.C. Johnston, J.M. Newsam, C.R. Safinya, and H.E. King, Phys. Rev. Lett. **58**, 2802 (1987).